

Progress of Surface Science Studies on ABX₃ Based Metal Halide Perovskite Solar Cells

*Longbin Qiu†, Sisi He†, Luis K. Ono†, Yabing Qi**

Dr. L. Qiu, Dr. S. He, Dr. L. K. Ono, Prof. Y. B. Qi

Energy Materials and Surface Sciences Unit (EMSSU), Okinawa Institute of Science and Technology Graduate University (OIST), 1919-1 Tancha, Onna-son, Kunigami-gun, Okinawa 904-0495, Japan.

*Corresponding author: Yabing Qi, E-Mail: Yabing.Qi@OIST.jp

†These authors contributed equally to this work.

Keywords: microstructure, energy level alignment, defect state, passivation, operando

ABX₃ type metal halide perovskite solar cells (PSCs) have shown performance over 25%, which is rocketing towards its limit. To gain the full potential of PSCs relies on the understanding of device working mechanisms and recombination, the material quality and the match of energy levels in the device stacks. In this progress report, we presented the importance of designing of PSCs from the viewpoint of surface/interface science studies. For this purpose, we first present recent case studies to demonstrate how probing of local heterogeneities (e.g., grains, grain boundaries, atomic structure, etc.) in perovskites by surface science techniques can help correlate the PSC parameters. At the solar cell device level that has active areas larger than the millimeter scale, the ensemble average measurement techniques can characterize the overall averaged properties of perovskite films as well as their adjacent layers and provides clues to understand better the solar cell parameters. How the generation/healing of electronic defects in perovskite will limit the device efficiency, reproducibility and stability and also induce the time-dependent behavior of J-V curves are also the focus of this report. On the basis of these studies, we propose the strategies to further improve efficiency and stability, meanwhile reduce hysteresis.

30 **1. Introduction**

31

32 Metal halide perovskites with the ABX_3 (here $A = MA^+ (CH_3NH_3^+)$, $FA^+ (CH(NH_2)_2^+)$, Cs^+ or
33 mixed A-cations; $B = Pb^{2+}$ or Sn^{2+} or mixed B-cations; $X = I^-$, Br^- or Cl^- or mixed X-anions)

34 structure have been developed and show a great potential for future solar energy applications.

35 It has been reported that theoretically, perovskite solar cells (PSCs) could attain efficiency of

36 30% with a single junction structure,^[1] which is higher than silicon solar cells (29.1%).^[2] PSCs

37 have reached efficiency up to 25.2%, which is already higher than polycrystalline silicon solar

38 cells (22.3%) and other thin film solar cells like CdTe solar cells (22.1%) and approaching the

39 record of silicon solar cells of 26.6%.^[3] Perovskite-based large area solar modules are also

40 growing in performance. Currently, the champion solar module with an area over 200 cm²

41 shows a certified performance of 11.98%.^[3] MAPbI₃ perovskite single crystals have also been

42 applied for solar cells and demonstrated an efficiency over 21% aided by the low density of

43 defect states.^[4] All-inorganic perovskite materials such as CsPbI₃ with a band gap of 1.7 eV,

44 the performance has been reported to be over 18%, which is promising for tandem structured

45 devices with over 30% efficiency.^[5] Tremendous efforts are being made into this field to further

46 improve the device performance towards its thermodynamic limit. The factors that determine

47 the device performance include the band gap, light absorbance, and charge generation and

48 extraction. No matter whether it is a single junction or multi junction perovskite based solar

49 cell, the surfaces/interfaces determine charge extraction and transfer, which dictates the overall

50 performance. How to improve charge separation and reduce the non-radiative recombination is

51 the main direction for the future performance improvements, which requires a perovskite

52 photoactive layer and neighboring interfaces with superior opto-electronic properties and

53 perfect energy level alignment match.

54

55 On the other hand, although the performance of PSCs is approaching silicon solar cells, several
56 issues still need to be overcome. Surfaces/interfaces play a vital role on device performance in
57 addition to hysteresis and stability. For example, the prevention of moisture infiltration with a
58 several-nanometer-thick lead oxysalt coating layer on the MAPbI₃ perovskite single crystal was
59 demonstrated by submersing the crystal under water for a long time.^[6] Ion migration is
60 considered as the origin for hysteresis phenomena in PSC current-voltage profiles.
61 Understanding of complex physico-chemical dynamics at interfaces will help design interfaces
62 that can further improve the efficiency and stability, while reduce hysteresis at the same time.

63
64 Regarding research efforts on technological aspects of device performance, improvements in
65 perovskite film quality, interface structure, and defect passivation play a crucial role for
66 overcoming device performance limits and increasing device stability. In this progress report,
67 we present recent case studies to demonstrate how probing of local heterogeneities (e.g., grains,
68 grain boundaries, atomic structure, etc.) in perovskites by surface science techniques can help
69 correlate the PSC parameters (**Section 2**). Understanding local properties at the micro,
70 nanometer, or even at the atomic scale is key to settling the several existing controversial issues
71 in perovskite materials and solar cells. On the other hand, at the solar cell device level that has
72 active areas larger than the millimeter scale, the ensemble average measurement techniques
73 play also a pivotal role (**Section 3**). Characterization of the overall averaged properties of
74 perovskite films as well as their adjacent layers (selective contacts and electrodes) provides
75 clues to understand better the solar cell parameters, such as open-circuit voltage (*V*_{oc}), short-
76 circuit current density (*J*_{sc}), fill factor (*FF*), and power conversion efficiency (*PCE*). The
77 functional layers within the solar cells under realistic operation conditions do not stay *static*,
78 i.e., a variety of perturbations (light, built-in potential, temperature, environmental gases, and
79 so on) lead to rich dynamical phenomena manifested in the final current density-voltage (*J-V*)
80 curves such as hysteresis and transient behaviors in *PCEs* (enhancement and/or deterioration as

81 a function of time). One of the fundamental origins for all of these time-dependent responses
82 lies in the generation/healing^[7] of electronic defects within the semiconductor band gap
83 influencing efficiency, lifetime, as well as reproducibility (Section 4).^[7a] How the local
84 heterogeneities in perovskites evolve as a function of time and how *in operando* surface science
85 techniques allow probing of properties changes in functional layers under PSC operation
86 conditions are also the central focus of this progress report.

87

88 **2. Local properties influencing solar cell parameters**

89

90 The behavior of a solar cell J-V curve and corresponding parameters of V_{oc} , J_{sc} , FF, and PCE
91 are governed by the balance of charge carrier generation, recombination processes, transport
92 across the bulk, and extraction at the interfaces. The device structure of a PSC is complex
93 comprised of multiple stacked layers. For instance, the cell architecture that has led to the
94 majority of the best certified efficiencies in the National Renewable Energy Laboratory (NREL)
95 chart is composed of a transparent conductive oxide (photoanode), electron transport layer
96 (ETL) including a mesoporous scaffold layer, a perovskite layer, hole transport layer (HTL),
97 and a high work function (WF) electrode (photocathode). Among these stacked layers, the
98 polycrystalline perovskite layer is often inherently nano/micro-structured with the presence of
99 grain boundaries^[8] and has varying chemical compositions and crystal structures/orientations
100 (Figure 1a). Therefore, the film local structure is expected to influence the overall device
101 macroscopic properties. Furthermore, under a certain stimulus (e.g., light, temperature,
102 environment) the perovskite layer will respond dynamically (i.e., a time-dependent response
103 behavior) impacting the overall device performance as a function of time. For example, a
104 measurement condition may exist under which a parameter under the study (e.g., photocurrent,
105 photovoltage, and so on) shows a transient behavior for a certain period of time and then reaches
106 an equilibrium, i.e., a static condition. The time-scale of the responses will vary according to

107 the physico-chemical processes (**Figure 1b,c**), for example, after free carriers are generated
108 upon incident photons, hot carrier cooling processes take place within picoseconds, while the
109 subsequent carrier transport and recombination processes occur within microseconds.^[9] Trap
110 states related processes (trapping, de-trapping, recombination) have the characteristic time-
111 scale in milliseconds. Ion migration has a longer time-scale in seconds.^[9] Description on (i)
112 how the solar cell parameters (V_{oc} , J_{sc} , FF, and PCE) can be correlated directly with the local
113 heterogeneity effects employing spatially-resolved techniques as well as (ii) how these local
114 heterogeneities evolve as a function of time are the central topics of this section. We discuss a
115 selected number of scanning probe microscopy (SPM) with multi-modality imaging capabilities,
116 electron microscopy, and spatially resolved optical microscopy techniques that showed
117 feasibility in describing the spatially- and temporally-resolved phenomena (**Figure 1 and Table**
118 **1**) in PSCs.

119

120 **2.1. Photocurrent mapping**

121

122 A few SPM techniques can provide insights into the photovoltaic characteristics of PSCs at the
123 nanoscale. Conductive AFM (c-AFM) is able to map the electrical properties such as local
124 charge distribution and charge transport (current distribution with sensitivity as high as a few
125 pA). A variant of c-AFM, photoconductive AFM (pc-AFM), employs additionally a light beam
126 that shines onto the sample. The local photocurrent characteristics as a response to the light-
127 stimulus, can be mapped and correlated simultaneously with the microstructural (topography)
128 features. The pc-AFM technique has been employed to understand the influences of grain
129 boundaries on the photovoltaic performance.^[10] While some studies found that the
130 photoconductivity at the grain boundaries was higher compared to that of grain interiors,^[10b, 10c]
131 a few other studies reported the opposite, i.e., the photoconductivity within a grain was higher
132 than that at the grain boundaries.^[10a, 10f] These results have already shown the complexity of

133 such studies, and the origin of this discrepancy can be due to the different sample preparation
134 conditions, influence of the underneath functional layers and substrate, the environmental
135 measurement conditions, the lack of consideration of the dynamics within the PSC such as ion
136 migration, and so on.^[11] Huang and co-workers^[10g] conducted a systematic study employing
137 spatially resolved local spectroscopy measurement in the dark by positioning the probe tip at
138 the location of a grain boundary or on top of a grain interior. The hysteresis phenomenon was
139 observed to occur majorly at the grain boundaries. In contrast, the measured dark current at the
140 grain interiors have shown negligible hysteresis. Upon light-stimulus, a gradual increase in
141 current (short-circuit conditions) was probed only when the pc-AFM probing tip was placed at
142 a grain boundary. As comparison, the short-circuit current probed on the top but inside a grain
143 remained almost unchanged. The similar conclusion was also corroborated by other works.^{[10a,}
144 ^{10g, 11-12]} These microscopic studies show that the transient behavior in photocurrent in
145 polycrystalline films are dominated by the faster ion migration within grain boundaries induced
146 by a built-in potential. As a consequence of this movement of electrically charged species and
147 accumulation at grain boundaries, it has been proposed that grain boundaries can be effective
148 in separating and collecting charges, hence enhance photocurrent.^[10b, 13] An alternative scenario
149 exists, i.e., the presence of nonstoichiometric crystals and/or neutral or charged impurities at
150 grain boundaries may also lead to the formation of localized electronic trap states within the
151 band gap, which can act as recombination sites deteriorating the overall PSC performance.^[14]
152
153 Large variations in photoconductivity are also observed when comparing the different grain
154 interiors within the same scanning area.^[10a, 15] Variations even inside a grain interior can be
155 seen indicating heterogeneity (**Figure 1a**). These heterogeneities can be of various origins and
156 were previously attributed to (i) facet-dependent density of trap states studied by c-AFM,^[10e]
157 (ii) PbI₂ passivation probed by light-modulated scanning tunneling microscopy (STM) and
158 scanning tunneling spectroscopy (STS),^[15] (iii) effects of additives (e.g., chlorine) leading to

159 enhanced photoconductivity measured by c-AFM,^[16] (iv) recombination losses at the interfaces
160 studied by pc-AFM,^[17] (vi) doping strategy in perovskite probed by pc-AFM,^[18] passivation
161 strategies such as pyridine^[19] and thiophene^[19b] leading to variations in PL mapping.

162
163 The abovementioned studies demonstrate that electronic charges upon light excitation are
164 significantly affected by the structural and chemical heterogeneity of grain boundaries and grain
165 interiors impacting the overall solar cell photocurrent. Further spatially-resolved mapping
166 combined with probing of time-resolved dynamics in perovskite materials will likely obtain
167 clearer pictures of the fundamental processes in photocurrent behaviors. Local photocurrent
168 magnitude, which is associated with the strength and profiles in photovoltage across the stacked
169 layers in PSCs is discussed next.

170

171 **2.2. Photovoltage mapping**

172

173 The photovoltage effect can be probed by Kelvin probe force microscope (KPFM) by
174 comparing the differences in CPD values of photovoltaic films in dark and under illumination
175 (ΔV). The value of ΔV cannot be directly converted to the value of V_{oc} , but it provides
176 qualitative information about the strength of the photovoltage effect. Furthermore, the ΔV
177 magnitude is related to the density of charge carriers, while the polarity of ΔV is associated
178 with the type of charge carriers (electrons or holes) on the surface.^[10f, 13b, 20] The concepts above
179 were also studied on MAPbI₃ perovskite samples when deposited on different layers of ETL
180 (FTO/c-TiO₂/MAPbI₃,) and HTL (FTO/PEDOT:PSS/MAPbI₃, where FTO = fluorine-doped
181 tin oxide, c-TiO₂ = compact layered TiO₂, and PEDOT:PSS = poly(3,4-
182 ethylenedioxythiophene) polystyrene sulfonate).^[10f, 13b] Considering the case of FTO/c-
183 TiO₂/MAPbI₃ (half-cell in n-i-p configuration), the surface photovoltage value (SPV)

184 difference when comparing under illumination and in dark revealed a positive shift ($\Delta V > 0$).
185 This was rationalized on the grounds that (i) the photoexcited charge carriers in the perovskite
186 layer are separated by the built-in field located at the $\text{TiO}_2/\text{MAPbI}_3$ interface, (ii) subsequently
187 electrons are effectively transferred to the c- TiO_2 ETL back contact layer and to the ground of
188 the KPFM system. (iii) Meanwhile, holes will be left in the perovskite and accumulate at the
189 surface of the perovskite layer. The built-in field at the $\text{TiO}_2/\text{MAPbI}_3$ interface has little
190 influence on ΔV and the electric field generated by the excess holes leads to the increase in
191 SPVs (i.e., $\Delta V > 0$). To highlight the critical role played by the selective contact layers, charge
192 separation and transfer were studied on $\text{FTO}/\text{PEDOT:PSS}/\text{MAPbI}_3$ (half-cell in p-i-n
193 configuration). It is found that SPVs taken under illumination show lower values than those
194 measured in dark.^[13b] This opposite result from the $\text{TiO}_2/\text{MAPbI}_3$ sample is explained due to
195 the preferential extraction of holes to the back contact of PEDOT:PSS. Hence, excess electrons
196 are accumulated on the surface of the perovskite layer leading to a global reduction of potential
197 variation ($\Delta V < 0$). The phenomenon of unbalanced charge extraction can be inferred when
198 comparing the average differences of ΔV in ETL/perovskite and HTL/perovskite. In the
199 experiment by Zhu and co-workers^[13b], $\text{FTO}/\text{TiO}_2/\text{MAPbI}_3$ and $\text{FTO}/\text{PEDOT:PSS}/\text{MAPbI}_3$
200 samples showed ΔV of approximately +39 mV and -10 mV, respectively. On the basis of these
201 ΔV values, it has been proposed that the ability of electron transfer at the TiO_2 /perovskite
202 interface is better than that of hole transfer at the PEDOT:PSS/perovskite interface.

203

204 KPFM is also widely employed to study the potential distribution across the stacks of all
205 functional layers constituting the complete solar cell device (**Figure 1b**). The measurement of
206 cross-section profiles in a full device can provide ample useful information but requires a clean
207 and flat sample surface. The sample fabrication for cross-section measurements has to be
208 handled carefully for the surface-sensitive techniques. The clean cross section can be prepared

209 by cleaving,^[21] or focused ion beam milling^[12c], such that the full structure and functionality of
210 each layer can be preserved. For PSCs typically the device side area outside the device boundary
211 was notched and fractured by tension rather than by compression to expose the cross-section.^{[21-}
212 ^{22]} After cleaving the sample surface can be polished either mechanically^[23] or by focus-ion
213 beam milling.^[12c] Scanning of CPD profiles on a cross-sectional surface provides key
214 information of “buried interfaces” such as energy level alignments with adjacent layers, band
215 bending, electronic trap states, and ionic accumulation at interfaces.^[12c, 21-22, 24] The electrical
216 potential distribution of highly performing device architecture that led to certified efficiencies
217 in the NREL chart has been widely studied by KPFM.^[25] These regular structured devices are
218 typically composed of FTO/c-TiO₂/mp-TiO₂/perovskite/ 2,2',7,7'-tetrakis(N,N-di-p-
219 methoxyphenyl-amine)9,9'-spirobifluorene (spiro-MeOTAD)/Au (or Ag).^[21, 24b] Systematic
220 studies by sequentially switching the light on and off revealed the dynamics of charge carriers
221 of perovskites when in contact with the ETL and HTL interfaces. Under illumination, holes
222 were observed to accumulate in the proximity to the HTL as a consequence of unbalanced
223 charge transport in the device, i.e., a high rate of electron extraction at the TiO₂/perovskite
224 interface was probed by cross-sectional KPFM. As a consequence, the accumulation of excess
225 holes creates an electrical potential barrier reducing the overall J_{sc}.^[22-23, 24b] These experiments
226 show the importance of a careful choice of ETL and HTL for controlling the potential
227 distribution within the PSC device. Not only the selective contacts, but also the chemical
228 composition of MAPbI₃ perovskite (PbI₂-rich or MAI-rich) was also observed to affect the
229 position of the potential drop where charge separation occurs (meaning the position of the diode
230 junction).^[22, 24e, 24f] The magnitude of the potential drop at the junction area is proportional to
231 the local electric field. Therefore, a larger potential drop indicates a stronger electric field and
232 efficient charge separation at the particular interface.^[24d] CPD profiles by KPFM obtained for
233 planar PSCs showed a significant potential drop at the c-TiO₂/MAPbI₃ interface. On the other
234 hand, the PbI₂-rich device exhibited a significant potential drop at the MAPbI₃/spiro-MeOTAD.

235 In sharp contrast, regardless of the variations in perovskite stoichiometry, when the mesoporous
236 layer of TiO₂ (mp-TiO₂) is employed, no localized potential drop was probed and all the
237 potential drop was observed to occur within the MAPbI₃ and mp-TiO₂ layer. These results
238 suggest that in the planar PSC, unlike the mesoporous PSC, a slight change in the precursor
239 stoichiometry strongly influences the potential distribution and the position of the diode
240 junction.^[22] More recently, Li and co-workers^[24f] demonstrated realization of a FTO/c-TiO₂/n-
241 type perovskite/p-type perovskite/spiro-MeOTAD/Au device by controlling the stoichiometry
242 of perovskite precursors. The homojunction interface of p-type perovskite/n-type perovskite
243 leads to a built-in electric field promoting oriented transport of photoexcited carriers with
244 minimum carrier recombination losses. As a proof of concept, fabricated PSCs with p-type/n-
245 type MAPbI₃ perovskite homojunction structure generated a certified PCE of 20.5%.^[24f]

246
247 From the studies above, KPFM has been demonstrated to provide vital information of the
248 electronic processes taking place at the “buried interfaces” formed between perovskite and
249 selective contacts. The time evolution of microscopic pictures of physico-chemical dynamics
250 at the interface will have help design new device structures and strategies that can further
251 enhance Voc in PSCs. Next, we discuss how the studies at the atomic-level in perovskite
252 materials can help elucidate dynamical processes discussed at the device level such as
253 ferroelectricity^[26] and halide segregation.^[27]

254

255 **2.3. Dynamical processes at the atomic level**

256

257 Perovskites are considered to possess a “soft” (or “plastic”) crystalline structure^[28] formed by
258 ions exhibiting rich dynamical processes such as organic cation rotations (**Figure 1c**)^[26, 29],
259 which leads to temporal-dependent deformation in the inorganic lattice.^[29a, 29b, 30] For instance,
260 the deformation and dynamics of a metal-halide lattice is associated with several local and

261 eventually averaged global effects such as (i) dynamic direct-to-indirect transitions in bandgap
262 suppressing charge recombination; (ii) spatially separated localization of valence and
263 conduction bands; and (iii) nanoscale ferroelectric domains (due to the MA⁺ cation dipole
264 moment) can assist separation of electrons and holes reducing their recombination. Chiu and
265 co-workers^[26] mapped the dynamics of the MA⁺ dipole orientation pattern in MAPbBr₃ single
266 crystals with atomic resolution upon light illumination employing photoexcited cross-sectional
267 STM and STS. The initial surface structure of a dimmer pattern (or checkerboard-like pattern)
268 in dark (**Figure 2a**) transitions to a much more complex structure with a characteristic one-
269 dimensional valley and hill pattern along the [1-10] direction under light illumination (laser
270 diode, 532 nm, 140 mW/cm²) (**Figure 2b**). This drastic modification of the potential energy
271 landscape affects significantly charge carrier transport. In dark, the non-uniform pattern of the
272 potential energy fluctuations and the lack of orientational confinement create many crossing
273 points of hole and electron pathways. Hence, the probability of recombination increases (**Figure**
274 **2a**). However, under illumination the reordering of the MA⁺ dipoles creates deep one-
275 dimensional potential energy wells with an average depth of ~150 meV. These aligned potential
276 well “highways”^[31] help charge transport and extraction toward the electrodes (**Figure 2b**).^[32]
277 Because these organic cations exhibit polarization phenomena, the topics / questions are
278 relevant:^[33] (i) whether ferroelectric domains walls (i.e., ferroelectricity) indeed exists in halide
279 perovskites and if so, (ii) how do they influence the overall performance in PSCs? Ferroelectric
280 domains were proposed to provide local internal electric fields that assist charge carrier
281 separation and hence reduce recombination on the positive side but contribute to I-V hysteresis
282 on the negative side. Piezo force microscopy (PFM) has been widely employed to image
283 polarization domains and local dipole moment switching in perovskites. Currently there are still
284 debates regarding ferroelectric properties of MAPbI₃^[11, 34] as shown by the conflicting
285 proposals: some groups reported the existence of ferroelectricity^[33, 35] while others reported the
286 absence of ferroelectricity.^[36] As pointed out previously,^[11, 33, 35b, 36c] several factors can

287 contribute to phase contrast in PFM such as (i) ion migration, (ii) local charge accumulation
288 (i.e., electrostatic effects), (iii) electrochemical phenomena inducing local changes in the
289 dielectric constant. All of these factors are expected to be present in perovskites, hence it is
290 important to differentiate the various microscopic mechanisms that contribute to the apparent
291 piezoresponse in order to confirm its intrinsic piezoelectricity. It has also been pointed out that
292 the identification and distinction of ferroelectricity from piezoelectricity and ferroelasticity
293 need be considered.^[36a, 37] Ferroelasticity corresponds to the mechanical equivalent of
294 ferroelectricity.^[33, 38] A ferroelastic material is a solid that exhibits a spontaneous strain in its
295 interior. This ferroelastic switching induced by a high mechanical stress can mediate the
296 formation of twin domains of alternating crystal phases or orientations. However, purely
297 ferroelastic domains are mechanical in nature and do not possess electrical dipoles, hence are
298 not influenced by external electric fields.^[33] The twin domains in MAPbI₃ were assigned to the
299 internal stress induced by the cubic-to-tetragonal phase transition stabilized during sample
300 annealing. The studies above show that ferroelectric switching in perovskites is yet to be
301 unambiguously established. Furthermore, exploration of light exposure effects on surface
302 polarization phenomena will be technologically relevant. New strategies of strain engineering
303 warrants further investigation and may aid designing high performing and stable PSCs.^[33]

304

305 Local heterogeneities in the structure, chemical composition, and phase^[39] in the perovskite
306 layer were identified to trigger the local physico-chemical dynamics upon a stimulus leading to
307 changes as a function of time from their starting original material. Halide segregation is an
308 example of these local changes eventually leading to degradation in mixed-cation and mixed-
309 halide perovskites.^[40] Ginsberg and co-workers^[41] performed combined cathodoluminescence
310 (CL) mapping coupled with a scanning electron microscopy (SEM) to visualize the spatial
311 segregation into iodide- and bromide-rich domains. After 5 min illumination at 100 mW/cm²,
312 small clusters enriched in iodide were observed to localize near grain boundaries. The

313 experimental results were compared with molecular dynamics (MD) simulations explaining the
314 fundamental processes: photoinduced phase separation arises when charged excitations
315 generate enough lattice strain to destabilize the solid solutions, favoring phase-segregation.
316 Their proposed model for the simulations indicates that naturally occurring small variations in
317 perovskite compositions after sample preparation is a main factor causing phase-segregation
318 upon light irradiation. Recently, Qi, Yan and co-workers^[27] revealed the exact locations of I
319 and Cl anions in real-space with atomic resolution on the surfaces of the MAPbBr_{3-y}I_y and
320 MAPbBr_{3-z}Cl_z mixed halide perovskites by STM. The surface reconstruction of a pristine
321 MAPbBr₃ surface has been previously described to show the characteristic dimmer and zig-zag
322 structures, with preference of the dimmer structure (Figure 2c).^[26, 42] The incorporation of I and
323 Cl leads to an additional randomly distribution of bright and dark protrusions (Figure 2d,e).
324 STM measurements probe local properties of a surface. To check the local inhomogeneity,
325 statistic data are acquired by scanning multiple areas on the same sample surface as well as
326 multiple samples of the same type. In Figure 2,^[27] STM measurements were performed on
327 different regions of the sample surface, and the statistical data of the STM height were provided
328 to show that the observed local atomic structure is indeed representative for the whole sample
329 surface. These findings are supported by the fast Fourier transform (FFT) analyses of the STM
330 images (insets in Figure 2c-e), which do not show any additional peak at low k -values for the
331 mixed-halide perovskites compared to pristine MAPbBr₃. On the basis of density functional
332 theory (DFT) calculations, the single bright or dark protrusion was assigned to the substitution
333 of Br with I or Cl, respectively. The energy barrier for the formation of two isolated Cl-Br pairs
334 is lower than the energy formation of a single Cl-Cl pair ($E_{2(\text{Cl-Br})} < E_{\text{Cl-Cl}}$). These results
335 suggest that at a low coverage Cl prefers to form isolated Cl-Br pairs rather than clustering
336 together to form Cl-Cl pairs or phase segregating. The same trend was found for the iodine
337 case, i.e., $E_{2(\text{I-Br})} < E_{\text{I-I}}$. This was proposed as the reason why the substitution of halide ions was
338 mainly found to be randomly distributed at the surface of the perovskite, leading to the

339 disordered surface structure. Furthermore, several other reports^[43] corroborate variations not
340 only in halide distribution, but also in cation distribution. Because PSCs are typically tested
341 under AM1.5 conditions (100 mW cm^{-2}), it is necessary to develop strategies to keep perovskite
342 systems resilient against phase segregation.^[44] Perovskite materials are inherently hygroscopic,
343 hence it is necessary to protect them against ambient air exposure for prolonged lifetime. On
344 the other hand, controlled small amounts of O_2 and/or H_2O were shown to be beneficial for
345 enhancing PL. For example, the impact of atmosphere (O_2 , H_2O , N_2) on the local luminescence
346 of individual perovskite grains was studied by Stranks and co-workers^[45] The response of each
347 grain to continuous light illumination and atmospheric environment was systematically studied
348 (Figure 3). PL mapping in N_2 shows the grain-to-grain heterogeneity with bright and dark grains.
349 When moisture is introduced in the form of $\text{N}_2 + \text{H}_2\text{O}$ ($\sim 45\%$ RH), PL maps reveal that both
350 the bright and dark grains show a gradual rise in PL intensity (Figure 3a). It is noticed that the
351 PL baseline (i.e., before any light illumination, $t = 0$) of the dark grain, which likely has a higher
352 defect density than the bright grain, increases to double. The same experiments but performed
353 in dry air (Figure 3b) reveal that the bright grain exhibits stable PL over time, while the dark
354 grain shows significant PL enhancement under illumination and eventually reaches the same
355 intensity as the bright grain. When PL mapping is measured under air + H_2O ($\sim 45\%$ RH), an
356 initial baseline increase ($t = 0$) in the emission intensity for both bright and dark grains is
357 observed. Then the emission from both bright and dark grains slowly rises over time under
358 illumination with a greater relative increase for the dark grain than the bright grain.
359 Summarizing above findings, dark grains show substantial enhancements under illumination in
360 the presence of O_2 and/or H_2O molecules, while bright grains show less of this effect. On the
361 basis of DFT, oxygen in the presence of photoexcited carriers was proposed to bind strongly to
362 iodide vacancies. As a consequence, this removes electronic trap states within the band gap,
363 leading to an increase in PL intensity over time. Because exposure to O_2 and H_2O can lead to

364 eventual degradation of perovskite films considering long-term exposure, it is necessary to
365 search for alternative molecules with passivating effects (extended discussion in [Section 4](#)).

366

367 In this section, recent studies show that understanding of fundamental dynamical processes at
368 the micro/nanoscale and at the atomic scale probed by microscopy techniques helps make
369 connections between the structural properties and the overall performance and stability of PSCs.
370 Simultaneous mapping of spatially- and time-resolved dynamics of perovskite materials will
371 likely impact further the design of next-generation highly efficient and stable PSCs. Above-
372 mentioned STM/STS is also a strong technique to probe both the valance band (VB) and
373 conduction band (CB) at the same time. Band-edges, band-alignment and band-diagram of
374 heterojunction solar cells can be probed by STM/STS. Pal and coworkers systematically studied
375 the band diagram and the type of conductivity of MAPbI₃ with different MAI/PbI₂ ratio by
376 STS.^[46] Pal and coworkers further studied the Cu₂O/MAPbI₃/PCBM interface and obtained a
377 band diagram by STS.^[47] The band diagram helps check whether the interface is energetically
378 favorable for charge separation. Further studies on the band diagram that probed ensemble
379 averaged properties and their influence on solar cell parameters are discussed in the next section
380 ([Section 3](#)).

381

382 **3. Ensemble averaged properties influencing solar cell parameters**

383

384 In addition to microscopy-based techniques, perovskite layers as well as their adjacent
385 functional layers are often characterized by techniques that provide ensemble averaged bulk
386 and/or surface properties such as XRD, UV-visible (UV-vis) spectroscopy, time-resolved PL
387 (TRPL), time-of-flight secondary ion mass spectrometry (TOF-SIMS), x-ray fluorescence
388 (XRF), x-ray photoelectron spectroscopy (XPS), ultraviolet photoemission spectroscopy (UPS),
389 and inverse photoemission spectroscopy (IPES). These ensemble averaging techniques have

390 the typical probing spot size in the micrometer to millimeter range, which are close to device
391 sizes (solar cell active areas have sizes in the millimeter scale or even larger). Hence, the
392 extracted averaged properties from the techniques above can provide a direct relationship with
393 the solar cell device performance such as J-V profiles and quantum efficiency measurements.
394 For instance, the characterization of valence and conduction band features of functional layers
395 and their energy levels, such as Fermi level (E_F), vacuum level (E_{Vac}), WF, ionization energy
396 (IE) or electron affinity (EA), are of paramount importance for explaining the device working
397 principles, such as charge carrier injection properties at the interface of two adjacent functional
398 layers and charge transport properties across the layer.^[48]

399
400 In this section, we discuss determination of the energy levels in perovskites by surface science
401 techniques of UPS and IPES. Emphasis is given to how (i) the presence of high density of
402 defects, (ii) and how the underneath substrate influence the determination of energy levels
403 (**Section 3.1**). We then discuss unintentional variations in the perovskite film compositions and
404 their influence on the electronic properties (**Section 3.2**). Subsequently, we discuss the energy
405 level alignments between perovskite and its adjacent selective contacts (ETL or HTL) (**Section**
406 **3.3**).

407

408 **3.1. Electronic structures of perovskites**

409

410 The most direct and quantitative measurements of IE, EA, E_F positions and WF are obtained
411 with a combination of UPS and IPES.^[48-49] The working principles of UPS and IPES, and
412 extraction of the WF, valence band maximum (VBM) and conduction band minimum (CBM)
413 from the raw spectra as well as calculation of IE and EA can be found in a review article.^[48b]
414 We only introduce those concepts briefly that are pertinent to this section. CBM and VBM
415 correspond to the electron and hole single-particle transport levels, respectively. Hence, the

416 energy difference between CBM and VBM (or EA – IE) is commonly designated as transport
417 band gap (E_G) to distinguish from the optical band gap (E_{Opt}), which is often determined by
418 UV-vis.^[48a, 49q] When IPES is not available, it is a common practice to extract EA' by
419 subtracting E_{Opt} from IE (i.e., $EA' = IE - E_{Opt}$). E_G is expected to be larger than E_{Opt} , because
420 E_{Opt} corresponds to the excitation of an exciton (the electron-hole bound pair) by photon
421 absorption in UV-vis.^[48a] In this context, it is possible to extract the exciton binding energy
422 ($E_{Exciton}$) from the energy difference between E_{Opt} and E_G . Gratzel, Park and co-workers reported
423 the first UPS measurements on MAPbI₃ deposited on TiO₂ estimating an IE of ~5.43 eV. EA'
424 of ~3.93 eV (i.e., $EA' = IE - E_{Opt}$) was extrapolated based on the optical band gap ($E_{Opt} \sim 1.5$
425 eV) determined by Tauc plots of the UV-vis spectrum. The first IPES measurements in
426 MAPbX₃ (X₃ = Br₃, I₃, I_{3-x}Cl_x) were reported by Kahn and co-workers.^[49a] In the particular case
427 of MAPbI₃, a smaller EA of ~3.7 eV was extracted from IPES and when compared to EA' (~3.9
428 eV). Because a similar IE of ~5.4 eV was extracted from UPS, E_G is larger than E_{Opt} in
429 agreement with the model ($E_G > E_{Opt}$).^[48a] Kanai, Kera, Tang and co-workers employed
430 UPS/IPES/UV-vis to extract $E_{Exciton}$ on perovskites with varying halide compositions: MAPbI₃
431 (~180 meV), MAPbBr₃ (~480 meV), MAPbCl₃ (~120 meV), MAPbI_{2.1}Cl_{0.9} (~160 meV),
432 MAPbI_{2.1}Cl_{0.9} (~40 meV), and MAPbBr_{1.5}Cl_{1.5} (~140 meV).^[49q] These values are in good
433 agreement with previous reports.^[49q, 50] For example, MAPbBr₃ has the characteristic excitonic
434 feature in UV-vis and it shows the highest $E_{Exciton}$. The smaller $E_{Exciton}$ means that the
435 photoinduced excitons can dissociate easily to become free carriers, which is an important
436 figure of merit for PSCs.

437
438 Mixed cations and mixed halide perovskites (or composition engineering) are reported to show
439 enhanced photo, thermal, and moisture stability with high PCEs compared to counterparts of
440 pristine MAPbI₃ and FAPbI₃.^[44, 51] Efforts are being made to understand the evolution of the
441 energy levels in perovskites as a function of composition.^[49c, 49q, 51] Recently, Tao, Olthof, and

442 co-workers determined systematically the IE and EA values of 18 primary Sn- and Pb-based
443 perovskites using UPS and IPES (**Figure 4a,b**).^[49c] DFT calculations were carried out to aid
444 the determination of the absolute positions of VBM and CBM.^[49b, 52] In addition, tight-binding
445 analysis was performed to explain the variations in energy levels of CBM and VBM as a
446 function of the ABX₃ perovskite composition, i.e., varying X (I, Br, Cl), B (Pb, Sn), and A (Cs,
447 FA, MA). The analysis of varying X shows that the energy of CBM is influenced by the Pb-X
448 distance (or the confinement effect). As the Pb-X distance decreases going from I to Br to Cl,
449 electrons on the Pb atom become more confined and their energy increases leading to up-shift
450 of the CBM (**Figure 4c**, left panel). VBM position shifts downward going from I to Br to Cl,
451 which is reflected by the predominant increase in electronegativity (**Figure 4c**, left panel).
452 When varying the B cation from Pb to Sn while keeping the X halide and A cation the same,
453 both IEs and EAs of Pb perovskites are larger than those of corresponding Sn ones (**Figure 4c**,
454 middle panel). This was rationalized by the fact that Sn has a smaller electronegativity than Pb.
455 When varying the A cation, both IEs and EAs do not show a uniform trend. The A site cation
456 does not contribute directly into the chemical bonding of the B-X framework and only
457 influences indirectly the electronic structure of B-X when changing the ABX₃ volume or
458 introducing distortion in the structure.^[53] Increasing the size of the A cation from Cs to MA to
459 FA leads to increase in the B-X framework. This lowers the B atomic levels due to moderation
460 in the confinement effect leading to down-shifts in VBM and CBM, but EA is affected the most
461 because it is more sensitive to the B levels. Structural distortion (octahedral tilting and lattice
462 deformation) reduces the hybridization between B and X states. Again, this leads to down-shifts
463 in VBM and CBM, but VBM is more affected because it is more sensitive to hybridization
464 (**Figure 4c**, right panel). This type of studies not only provide the fundamental understanding
465 of the evolution of key factors that determine the absolute energy levels (IE, EA, and E_G), but
466 also open up possibilities for rational material design for composition- and interface-
467 engineering strategies.

468

469 As pointed out in several reports,^[49b, 49c, 52] there is a challenge to reliably extract the onset of
470 VBM or CBM from UPS and IPES, respectively, on perovskites. Kahn and co-workers pointed
471 out that the frontier electronic states in lead halide perovskites have a low intensity on a linear
472 scale due to the small density of states (DOS) at the VBM and CBM frontiers. Hence, these
473 onsets could be missed with conventional fitting procedures (linear extrapolation of the lowest
474 binding energy features in a linear intensity scale). The logarithmic plot in intensity and the
475 fitting of DFT-calculated DOS to the experimental DOS at the band edges were proposed to
476 determine with better accuracy the VBM and CBM onsets. In addition to the inherent
477 difficulties of VBM and CBM onset determinations in perovskites, these energy levels depend
478 sensitively on the (i) orientation of crystal structure, (ii) density of defects introducing
479 additional states at the band edges, (iii) surface morphology, (iv) chemical composition
480 variations between grains and grain boundaries, and (v) insufficient coverage leading to the
481 underneath substrate features overlap in UPS/IPES spectra. With the aim to attain the pristine
482 electronic structures of perovskites without the convolution of the parameters above, Koch and
483 co-workers studied the band structure of single crystalline perovskites of MAPbBr₃ and
484 MAPbI₃ by using angle-resolved photoemission spectra (ARPES) and low-energy electron
485 diffraction (LEED).^[52] LEED was employed to determine the surface orientation, lattice
486 parameters, and crystal symmetry group. LEED patterns measured on MAPbI₃ single crystal
487 samples at room temperature exhibited the coexistence of cubic and tetragonal structures
488 (**Figure 5a**).^[39] The determined lattice parameters are $a^T = 7.96 \pm 0.16 \text{ \AA}$ (assigned to the (001)
489 surface of the tetragonal phase) and $a^C = 6.02 \pm 0.11 \text{ \AA}$ (assigned to the cubic phase). On the
490 basis of the LEED spot intensity analysis, it has been suggested that the MAPbI₃ surface is
491 predominantly composed of the cubic phase. ARPES measurements along the high symmetry
492 directions (X—M and X—R momentum directions, **Figure 5a**) were overlaid with the DFT

493 calculated band dispersion showing good matching (insets in **Figure 5b**). The detailed
494 knowledge of the single crystal band structures allows reliable determination of the VBM onset.
495 Selected cuts through the band structure between X—M and X—R shown on a linear scale
496 (directions of the cuts are marked in the insets in **Figure 5b**), reveal large variation in the VBM
497 with the highest VBM onset at X (~1.9 eV) and the lowest VBM onset at R (~1.4 eV). The
498 single crystal electronic structure can be translated to the polycrystalline MAPbI₃ film by
499 integrating the individual cuts for each direction of k_{\parallel} in M—X—R (**Figure 5c**). It is observed
500 that the VBM onset is overestimated when evaluated from the extrapolation on the linear scale.
501 However, from the semi-log plot, the VBM onset is found at 1.40 eV matching well the global
502 VBM found from the ARPES spectrum taken at point R. The same analysis of VBM
503 determination in semi-log plots was also applied for MAPbI₃ polycrystalline thin films that are
504 expected to have random crystal orientation (**Figure 5d**). Similar to the observations obtained
505 for the integrated ARPES spectra in single crystals (**Figure 5c**), the logarithmic scaled intensity
506 plots for polycrystalline film (normal-emission UPS) leads to the VBM onset value close to the
507 global VBM (**Figure 5d**). In contrast, the linear scale plots give rise to overestimated VBM
508 onset. This study highlight the necessity to use a logarithmic intensity scale to determine the
509 VBM onset (with a remaining fundamental uncertainty of ~50 meV, mostly underestimating
510 the onset).^[49b, 49c, 52] On a separate note, ARPES allows the evaluation of the hole effective mass
511 (m_h^*) by performing a parabolic fit of the VBM at points R and M.^[49i, 52, 54] Values of $0.18 \pm$
512 $0.06 m_0$ at M (along X—M) and $0.50 \pm 0.10 m_0$ near R (along X—R). On the basis of these m_h^*
513 values, a lower-limit hole mobility values in the range of several tens of $\text{cm}^2/\text{V}\cdot\text{s}$ was deduced,
514 which is another important figure of merit for PSCs.^[52]
515
516 Surface defects states lead to band bending at the surfaces of perovskite polycrystalline films
517 and single crystals.^[55] However, the electronic influences of surface bend banding and how

518 much band bending extends to the bulk (that has a much lower concentration of defect
519 density^[56]) is still not well understood. A flat-band condition is commonly assumed for the bulk
520 in terms of energy level alignments.^[49a, 57] From theoretical calculations, the energetically
521 favorable intrinsic defects (i.e., with low formation energies such as MA or iodide vacancies)
522 in MAPbI₃ films induce shallow states that are close to either CBM or VBM.^[58] Based on the
523 different defects states, perovskites could be either n-type or p-type semiconductors depending
524 on growth conditions and substrates. Koch and co-workers reported that for MAPbI₃ thin films
525 and single crystals, E_F is strongly pinned to CBM due to the surface defect states and donor
526 agent of Pb⁰.^[55b] While under light illumination, VBM detected in UPS would shift up to 0.7
527 eV, due to filling up of the surface trap states by photoexcited electrons and reduction of the
528 surface band bending (**Figure 6a**).^[55b] They further investigated the relationship between the
529 band structure and the density of the surface trap states (**Figure 6b**).^[55a] It is shown that with a
530 low density of trap states, the photovoltage effect could modify the surface and reduce the
531 surface band bending. While for a high density of the surface defect states the E_F is strongly
532 pinned to the CBM. This surface defect states also influence the energy level alignment between
533 perovskite surface and charge transport layers. For example, ETLs like 1,4,5,8,9,11-
534 Hexaazatriphenylenehexacarbonitrile (HATCN) and 1,3,4,5,7,8-hexafluoro-
535 tetracyanonaphthoquinodimethane (F6TCNNQ) with large EA values coated on top of MAPbI₃
536 with different density of surface defects were investigated (**Figure 6b**).^[55a] When HATCN was
537 coated on MAPbI₃ with a low density of surface defect states, the band bending is reduced and
538 flat band structure is formed with a suitable energy level alignment between MAPbI₃ and
539 LUMO of ETL. While in the case of a high density of surface states, CBM of MAPbI₃ is
540 strongly pinned to E_F and there is a large energy barrier for electron transferring from MAPbI₃
541 CBM to LUMO of ETL (**Figure 6b**). On the other hand, the hole blocking properties might
542 also be reduced due to the smaller barrier between VBM of MAPbI₃ and HOMO of ETL
543 (**Figure 6b**).^[55a] Differences in the density of surface states are attributed as one of the reasons

544 leading to variations in energy level alignment properties reported in several different studies
545 even on the same material system, for example, MAPbI₃/C60.^[49f, 49g, 57]

546

547 In a typical PSC device, the perovskite layer is sandwiched between the selective contacts or
548 electrodes (e.g., carbon-electrode), forming a multi-layered stacked structure with several
549 interfaces. Hence, the energy levels dictated by the intrinsic properties of the perovskite
550 material can also be influenced when in contact with another material, which is associated with
551 the dipole formation and band bending phenomena at interfaces.^[49s, 57, 59] In this sense, the
552 reported energy level alignment based on the vacuum level alignment may miss the effects of
553 interfacial states, interfacial dipoles, and band bending.^[11, 48b, 48c, 59b, 60] Film deposition by
554 vacuum methods are suitable for studying the energy level alignments because the incremental
555 deposition followed by UPS, IPES, and XPS measurements allow detailed studies of energy
556 levels and chemical composition across the whole film thickness. A large number of works
557 investigated the energy level diagrams at interfaces that form heterojunctions with perovskites
558 by depositing a top layer corresponding to commonly employed HTLs or ETLs: MAPbX/spiro-
559 MeOTAD (X = I₃, I_{3-x}Cl_x,Br₃),^[49a] MAPbIBr₂/spiro-MeOTAD,^[61] MAPbIBr₂/1,4,5,6,8,11-
560 hexaazatriphenylene hexacarbonitrile (HAT-CN),^[61] MAPbI₃/Au,^[49g, 62] MAPbIBr₂ and
561 MAPbI₃/MoO_x,^[61, 63] MAPbI₃/copper phthalocyanine (CuPc),^[64] MAPbI₃/pentacene,^[65]
562 MAPbIBr₂/N,N'-di(naphthalene-1-yl)-N,N'-diphenylbenzidine (NPB),^[61] MAPbIBr₂/copper-
563 hexadecafluoro-phthalocyanine (F16CuPc),^[61] and MAPbI₃/C60.^[49d, 49g, 57, 66]

564

565 There are studies that perovskite films coated on different substrates may change the position
566 of E_F.^[49s, 57, 59a, 59b, 67] Interestingly, not only the electronic properties at the interfaces are
567 influenced by the underneath substrate, but also the bulk properties of the perovskites (typically
568 a film with a thickness of ~200-300 nm) are also affected.^[49s, 57, 59a-c] In fact, it has been
569 hypothesized that the underneath substrates may change doping densities in perovskites and

570 turn the perovskites from n-type to p-type or *vice versa*.^[68] The nature of the substrate not only
571 changes the energetic alignment of the perovskite layer, but also introduces gap states and
572 influences the film formation and morphology. In a study by Kahn and co-workers using PES
573 and IPES, for MAPbI₃ films deposited on NiO and TiO₂, it is demonstrated that MAPbI₃ films
574 show a slightly p-type characteristic on top of NiO and better energy level alignment with the
575 top ETL (C60). While the MAPbI₃ film on TiO₂ is more n-type due to the n-type properties of
576 the bottom oxide layer.^[57]

577
578 On the other hand, a few studies succeeded in growing perovskite layers by co-evaporation in
579 vacuum or in a step-wise deposition manner for the energy level studies of perovskites when
580 deposited on different substrates.^[59a, 59d, 60] Zou and co-workers studied the substrate effect on
581 the surface electronic structure of evaporated MAPbI₃ films on Al (AlO_x), Si (SiO_x), TiO₂, ZnO,
582 ITO, Au, PEDOT:PSS, MoO₃ (**Figure 7a,b**).^[59a] Similarly the WF of MAPbI₃ increases with
583 the substrate WF. The shifts in VBM to lower binding energy also indicate a transition from n-
584 type to p-type due to the substrate effect.^[59a] Olthof, Meerholz and co-workers studied
585 systematically the electronic structure changes of vacuum-deposited MAPbI₃ on four different
586 substrates (PEIE, ITO, PEDOT:PSS, MoO₃; where PEIE = polyethylenimine ethoxylate and
587 ITO = indium-doped tin oxide) by incremental deposition with film thicknesses from 3 nm up
588 to 200 nm.^[59b] In contrast with a thick solution-prepared film, the incremental thickness helps
589 the study of interface dipole and band bending within the perovskite layer. The WF of
590 evaporated MAPbI₃ depends on the substrate within the investigated thickness. But the
591 observed interface dipoles and band bending with increasing thickness suggest that the vacuum
592 level alignment and flat band structure is not the case in this study.^[59b]

593
594 As mentioned above, the WF determination by the substrate might be valid for a perovskite
595 film with a gap state-free interface and a low doping concentration, as systematically studied

596 for organic semiconductors.^[67, 69] Cahen and co-workers studied the WF evolution of the lead
597 bromide based perovskites as a function of the WF for the different substrates (**Figure 7c and**
598 **d**). For mixed cation based perovskite (FA_{0.85}MA_{0.1}CS_{0.05})PbBr₃, the free carrier concentration
599 is determined to be low^[69] and WF increases with the increase of the substrate WF (**Figure**
600 **7c**).^[67] While for other Br based perovskite films (**Figure 7d**) WF did not show a positive
601 relationship with the substrate WF,^[67] which was attributed to the higher doping density and
602 higher free carrier densities.^[69]

603
604 The above studies demonstrate that the electronic structure of perovskite materials are
605 determined by their composition, density of surface defect states, and substrate WF.
606 Furthermore, whether the substrate WF influences the perovskite surface energy level diagram
607 also depends on the perovskite doping density and free carrier densities. These provide hints
608 for the device architecture design once the energy level diagrams for each material layer are
609 determined. On the other hand, the composition is not always uniformly distributed as in the
610 precursor solution, especially for the two-step mixed cation perovskite formation. How the
611 unintentional variations in the chemical composition and distribution influence energy level
612 alignment is discussed in the next section.

613

614 **3.2. Unintentional variations in chemical composition**

615

616 The electronic and optical properties of perovskites are sensitive to the chemical composition
617 (**Section 2.3**). Often a scenario exists in attempting to link the microstructure and opto-
618 electronic properties of perovskite films and devices to the initial nominal precursor ratios or
619 chemical composition, where a correlation cannot be found. One of the origins for these large
620 variations and difficulties in PSC reproducibility is related to the unintentional variations in
621 chemical composition in perovskites during film processing.^[70] Perovskite films can be

622 deposited by a diversity of techniques including solution- and vapor-based methods.^[71] In
623 addition, the several precursor materials with different stoichiometries^[70, 72] as well as
624 employment of additives^[73] aiming at optimization of perovskite film morphology (e.g.,
625 uniform coating, large grains), may lead to an unintentional unbalanced chemical composition
626 of perovskites. The commonly employed post-annealing treatment after the perovskite
627 deposition may also change the composition and thus lead to variations on the energy levels of
628 perovskites (VBM, CBM, WF)^[49d, 72d, 74] as well as to self-doping phenomenon (showing
629 characteristic n- or p-type behavior).^[74-75] XPS is a widely employed surface science technique
630 to investigate the surface chemical composition. A few systematic studies provide insights on
631 the large variations in IE (ranging from 5.1 eV to 6.6 eV) and EA (3.9 eV to 4.6 eV) reported
632 in literature.^[70, 72c, 72e] Meerholz, Olthof, and co-workers investigated the dependence of
633 chemical composition (XPS) and corresponding energetics (UPS) by preparing 15 solution
634 processed samples and 23 vapor deposited samples with various preparation conditions such as
635 varying precursors molar ratios and annealing parameters (**Figure 8a**).^[72c] As a result, MAPbI₃
636 films with diverse surface chemical composition was observed by XPS measurements. The ratio
637 of R_{exp} , i.e. the ratio of Pb/N content, was extracted to provide the information of the contents
638 of PbI₂ and MAI in perovskite. R_{exp} ranging from 0.4 to 1.5 was observed to correlate
639 proportionally to IE, showing that a perovskite film with excess PbI₂ film exhibits a higher IE,
640 while perovskites with excess MAI show smaller IE (**Figure 8a**). This similar trend can also be
641 found by using one step solution method and varying the precursor ratios of a lead acetate
642 trihydrate (Pb(Ac)₂·3H₂O) and MAI.^[70] Furthermore, these trends in the energy levels variations
643 are not characteristic only to MAPbI₃, but also to mixed halide perovskites of MAPb(I_{1-x}Br_x)₃
644 and MAPb(I_{1-x}Cl_x)₃.^[72e] These works highlight the low tolerance of perovskite surfaces to small
645 deviations from the nominal precursor stoichiometry. As a consequence, self-doping
646 phenomenon (i.e., variation in the relative position of E_{F} with respect to the VBM or CBM)
647 leading to n-type (E_{F} close to CBM) or p-type (E_{F} close to VBM) behavior is observed in the

648 same perovskite material. For example, a consensus exists that stoichiometric MAPbI₃
649 (PbI₂:MAI ~ 1.0) leads to weakly n-type behavior in MAPbI₃ perovskites, while a high
650 PbI₂:MAI ratio (> 1.7) leads to heavily n-type behavior. On the contrary, MAPbI₃ with excess
651 of MAI (PbI₂:MAI < 0.6) leads to only weakly p-type behavior.^[49d, 72d, 74] These observations
652 were associated with the DFT calculated point defects (**Section 4**) and associated with MA⁺-
653 deficient defect.^[48b, 49d, 58a, 76] The MA vacancy (V_{MA}) leads to shallow acceptor levels within
654 the band gap. However, a close inspection of the XPS C 1s core level signal in MAPbI₃ shows
655 actually two distinct peaks meaning the coexistence of at least two C-related species; see
656 spectrum (i) in **Figure 8a**.^[49m] The peak fitting analyses lead to the assignments of the high
657 binding energy (BE ~ 286.5 eV) species to the MA in MAPbI₃ crystal lattice.^[49m] A careful
658 analysis of XPS atomic concentrations after normalization by the atomic sensitivity factors
659 (ASFs) confirms that MAPbI₃ shows close to the ideal ratios of [Pb] : [I] : [C(CH₃NH₃⁺)] : [N]
660 ratios of 1 : 3 : 1 : 1. In the particular example shown in **Figure 8a**, [Pb] : [I] : [C(CH₃NH₃⁺)] :
661 [N] ~ 1 : 2.9 : 1.1 : 1.1 was reported.^[49m] The origin of the C 1s peak at a lower BE of ~284.8
662 eV (**Figure 8a**) remains controversial at present and it has been proposed that this peak could
663 originate from C in CH₃I,^[49m, 59b, 72a, 72b, 77] CH₃NH₂,^[49m, 59b, 78] adventitious carbon,^{[59a, 70, 72d, 73,}
664 ^{75b]} and/or remaining solvents.^[72e] The assumption of CH₃I generation due to MAI dissociation
665 was further corroborated by mass spectrometry^[58b, 79] and soft X-ray absorption and emission
666 techniques.^[77b] Park, Qi, and co-workers performed a comprehensive study of depositing MAI
667 with different thicknesses (ranging from 1 nm up to 32 nm) by vacuum evaporation on the
668 surface of MAPbI₃ perovskite (**Figure 8a**).^[49m] While no changes are observed in Pb 4f, I 3d,
669 and N 1s (no O 1s features were observed in this study) core levels, C 1s shows the appearance
670 of additional two species as MAI content is increased. The assignments of these two species
671 were performed on the basis of atomic ratios analyses. MAI deposition up to 4 nm leads to [C] :
672 [N] ~ 1.5 : 1 indicating the excessive carbon from the dissociated MAI species. The nitrogen
673 signal did not follow the carbon contents, most likely due to release of ammonia gas^[58b, 79] or

674 other nitrogen-containing gas species. Upon 32 nm MAI deposition on MAPbI₃, the [N] : [I]
675 ratio decreased from ~1 : 3 (corresponding to pristine MAPbI₃) to approximately 1 : 2 meaning
676 that approximated closer to optimal MAI ratio of [N] : [I] ~ 1 : 1. Similar trends of partial MAI
677 decomposition were reported when deposited on different substrates.^[59a, 59b, 59d] More
678 importantly, the analysis of UPS showed a better alignment of VBM of MAPbI₃ with the highest
679 occupied molecular orbital (HOMO) level of spiro-MeOTAD HTL when excess of MAI (4 nm)
680 was deposited on MAPbI₃ (left panel in **Figure 8b**). On the basis of XPS, it has been concluded
681 that it is not the MAI layer, but the dissociated species of MAI that lead to the interfacial energy-
682 level tuning. The optimized interface energetics were verified with solar cell performances
683 (right panel in **Figure 8b**), showing an enhancement of 19% in average steady-state PCE. These
684 studies demonstrate that although UV-vis, SEM, and XRD that provides bulk-related properties
685 show marginal changes in the perovskite film quality, the surfaces and interfaces of perovskites
686 show large variations in chemical composition. Hence, a strong dependence of the overall PCEs
687 with the surface and interface phenomena of stoichiometry ratios (right panel in **Figure 8b**).
688 These studies clearly underscore the necessity of performing surface science studies in parallel
689 to device research.

690

691 The photoemission spectra determine not only the surface electronic properties and composition,
692 but also provide information for the bulk. Synchrotron-based techniques are strong and
693 complementary tools for this purpose.^[80] Here the usage of hard x-ray photoelectron
694 spectroscopy (HAXPES) is discussed. XPS is mainly for surface composition information.
695 While how the cations distribute inside the bulk is related to the bulk properties, especially for
696 recently developed quadruple cation perovskite with Cs, Rb, MA and FA. Philippe, Saliba and
697 co-workers applied HAXPES with different energies, thus probing different depths within the
698 film to understand the chemical distribution of the four cations.^[43g] With a higher energy of
699 4000 eV the probing depth could be up to 18 nm, which could be considered as the bulk

700 composition. As reported there is a remaining PbI_2 in the double- and triple- cation perovskite.
701 For double cation, even the unreacted FAI is present at the surface. With the increase of cation
702 numbers, the excess PbI_2 reduced and in the quadruple cation perovskite there is no excess of
703 PbI_2 . In addition, the insertion of Cs could uniformly distribute both at the surface and in the
704 bulk, while Rb tends to locate towards the bulk.^[43g]

705
706 To conclude this part, the surface electronic properties rely on the surface composition.
707 However, the surface composition is not always the same as in the precursor solution.
708 Furthermore, the distribution of cations and halides is different from the surface to the bulk.
709 Intentional addition of extra PbI_2 or MAI in the interface will be helpful to passivate the surface
710 defect states, which reduces the non-radiative recombination and enhances the charge transport
711 with better energy level alignment. This also highlights the importance of surface passivation,
712 which is discussed in [Section 4](#).

713

714 **3.3. Energy level alignment at interfaces and the universal energy level tailoring**

715

716 One important role for achieving high V_{oc} and J_{sc} is the optimally aligned energy levels
717 throughout the whole device. The energy level diagram is often adopted as a versatile tool to
718 understand how the combination of functional layers could serve to transfer the charges and
719 block recombination. However, this is only one of the considerations and does not completely
720 determine the overall device efficiency. The in-gap states and built-in potential related to the
721 interfacial defect states are also crucial for achieving high V_{oc} .^[67] V_{oc} of a solar cell is
722 considered as the difference between the quasi Fermi levels of perovskite under illumination.^[81]
723 Energy level matching is required in the interface between ETL/perovskite and HTL/perovskite
724 for electrons and holes to be transferred with minimum energy losses (V_{oc} deficit). For example,
725 one can determine the electron/hole transfer or blocking properties from combined UPS/IPES

726 spectra.^[82] The widely employed NiO_x, PEDOT:PSS, spiro-MeOTAD, poly(3-hexylthiophene-
727 2,5-diyl) (P3HT) and poly(triaryl amine) (PTAA) are characterized as good HTLs.^[49h, 83]
728 Similarly, TiO₂, SnO₂, C60, and phenyl-C₆₁-butyric acid methyl ester (PCBM) are
729 characterized as good ETL because the CBM of the mentioned ETL matches well with CBM
730 of the typically used perovskite for single junction solar cells.^[57, 82a, 84] Other than the CBM
731 matching with ETL for efficient charge transfer, the hole blocking property with a deep VBM
732 level is also required to reduce recombination. For example, C60 is a suitable layer for electron
733 extraction from perovskite, but the small band gap leads to recombination processes. The barrier
734 for hole blocking is small, and is considered to be the main reason for the lower Voc for inverted
735 structure device compared with normal structure device.^[57] The interfacial defect states from
736 the ETL also influence the device performance. Qi and co-workers recently studied
737 systematically the in-gap states of the sputtered SnO₂ induced by Ar plasma.^[84a] It is shown that
738 with minimized Ar plasma power and processing time during the sputtering deposition of SnO₂
739 layer, the interfacial defect states is much reduced leading to improved Voc in devices with
740 normal structure.

741
742 Recently, Neher and co-workers studied systematically the energy level alignment of the
743 following stacks: ITO/perovskite, PEDOT:PSS/perovskite, P3HT/perovskite, perovskite/spiro-
744 MeOTAD, PTAA/Poly((9,9-bis[30-((N,N-dimethyl)-N-ethylammonium)-propyl]-2,7-
745 fluorene)-alt-2,7-(9,9-di-n-octylfluorene)) dibromide (PFN)/perovskite, SnO₂/perovskite,
746 TiO₂/perovskite, perovskite/PCBM, perovskite/C60, perovskite/LiF/C60; which are commonly
747 used in normal and inverted structure PSCs.^[81] The quasi Fermi levels determined in above
748 mentioned stacks were observed to correlate directly with the Voc of corresponding high
749 performance devices. For poor performing devices, the Voc is substantially lower than the quasi
750 Fermi level, which is due to the energy level misalignment at the HTL.^[81] More detailed

751 descriptions about the energy level alignment for specific interfaces can be found from several
752 recent review articles.^[48b, 48c]

753

754 Regarding the design of interfaces favorable for charge extraction and transport, a promising
755 approach is searching for energy-level tailoring molecules/polymers as interface modifiers and
756 is a hot topic recently. In recent studies, the heterojunction or homojunction structure with inter
757 band energy level alignments help further improve the charge transfer. In recent works, there
758 are many works reporting the gradient perovskite structure, for example 2D/3D hybrid interface
759 or homojunction formation. As we discussed above, the electronic properties of perovskites
760 formed on different substrates are different.^[57, 59b] On a n-type substrate the perovskite is more
761 n-type and on a p-type substrate the perovskite behaves as p-type as studied by Kahn and co-
762 workers.^[57] This is especially important for optimization in p-i-n junction structured device
763 because a p-type surface will be formed in contact with top ETL. Yan and co-workers recently
764 reported that with a treatment of guanidinium bromide (GABr) aiming wide band gap
765 perovskite in inverted structure device, the surface is n-type with Fermi level shifting towards
766 vacuum level. The as prepared device showed improved Voc with a better energy level
767 alignment.^[85] In a work by Bawendi and co-workers, the formation of layered perovskite
768 interface helps reduce voltage loss by the formation of electron blocking layer that reduce the
769 interface recombination.^[86]

770

771 Energy level alignment determines the quasi Fermi level for a perovskite film under light
772 illumination. This section highlights the importance of the energy level alignment of perovskite
773 materials and the design of neighboring interfaces. With better energy level alignments (i.e.,
774 less energy barrier for charge transfer), the device efficiency could be further improved with
775 less non-radiative recombination and higher Voc.

776

777 4. Defects and interface engineering

778

779 The fundamental origin of the dynamical processes discussed in [Sections 2](#) and [3](#) are closely
780 related to defects in perovskites.^[58b] For example, ion migration can be mediated by point
781 defects in perovskites ([Figure 9a](#));^[87] the type of defects such as MA⁺ vacancies (acceptor) and
782 I⁻ vacancies (donor) determines the p-type and n-type behavior in MAPbI₃ ([Figure 9b](#));^{[58a, 76a,}
783 ^{88]} carrier density enhancement and light-induced degradation in MAPbI₃ are related to defect
784 dynamics leading to I₂ generation as discussed later in details ([Figure 9c](#)),^[89] and so on. In
785 semiconductor technology, the generation of electronic defects within the semiconductor band
786 gap limit performance, lifetime, as well as reproducibility.^[7b, 14f, 87d, 90]

787

788 In this section, discussion on the current understanding of the origin and nature of defects in
789 perovskites and their impact on the dynamical processes as well as their influences on the
790 overall solar cell performance will be discussed. The characterization of defects based solely
791 on experimental techniques are usually inconclusive. The combination of experiment and
792 theory is necessary to gain the understanding of the system being studied. The classification of
793 defects in semiconductors and their electronic properties are important to be understood first
794 ([Section 4.1](#) and [Table 2](#)). Efforts are being made to verify experimentally the theoretical
795 predictions of trap states energy levels and trap densities. The commonly employed techniques
796 will be discussed further ([Section 4.2](#) and [Table 2](#)). Last, approaches (interface or passivation
797 engineering) and their passivated effects on device performance used to lower the density of
798 defects in crystals and layers are presented and discussed ([Section 4.3](#) and [Table 2](#)).

799

800 4.1. Theories on the type of defects and experimental results

801

802 Formation of defects is unavoidable during the crystal growth and post-treatment processes due
803 to a relatively fast crystal growth dynamics of perovskite films. Further generation of defects
804 are also expected during the operation of PSCs. Compared with the perfect structure of
805 perovskite, the possible different types of defects are summarized in **Figure 9d**.^[91] It can be
806 divided into two categories including point defects and dimensional defects.

807

808 4.1.1. Point defects

809

810 For the basic point defects, they are formed from intrinsic vacancy, interstitial, antisite
811 substitution, or by extrinsic introduction of foreign atoms (**Figure 9d**). Based on the point defect
812 theory, the two common defect pairs are Frenkel defects, i.e. simultaneous vacancy and
813 interstitial of the same ion, and Schottky defects, i.e. vacancies of two different anions and
814 cations.^[90c] Furthermore, while DFT results have shown that Frenkel defects (e.g., Pb^{2+} , I^- , Br^- ,
815 MA^+) lead to both deep and shallow trap states in perovskites,^[58a, 76a] Schottky pair defects (e.g.,
816 PbI_2 and PbBr_2 vacancies and MAI and MABr vacancies) do not generate trap states within the
817 band gap.^[90f, 90g, 92] DFT is one of the important tools that provide useful guidance to deeply
818 understand point defects and defect pairs and to further help the design of perovskite preparation
819 with a minimal defect density associated with high performing devices. The formation energies
820 of different defects are calculated by first-principle calculations to evaluate the expected type
821 of defects in perovskites.^[76a, 93] MAPbI_3 has been the most investigated perovskite materials as
822 it is one of the most well-known perovskite absorber, but the calculations have shown
823 conflicting results. All possible intrinsic point defects in α - MAPbI_3 (pseudo-cubic high-
824 temperature phase)^[94] was first studied: three vacancies (V_{MA} , V_{Pb} , V_{I}), three interstitial (MA_i ,
825 Pb_i , I_i), two cation substitutions (MA_{Pb} , Pb_{MA}), and four anti-site substitutions (MA_{I} , Pb_{I} , I_{MA} ,
826 I_{Pb}) using the generalized gradient approximation without spin-orbit coupling (SOC).^[58a] It was
827 found that defects of V_{MA} , V_{Pb} , V_{I} , MA_i , I_i , MA_{Pb} , Pb_{MA} , MA_{I} have low formation energies

828 leading only to shallow energy levels. Defects of Pb_i , Pb_I , I_{MA} , I_{Pb} have relatively high formation
829 energies with deep energy levels (**Figure 10a**). It was suggested that MAPbI_3 is an ionic
830 material showing very weak covalence, which is the key for the absence of deep-level defects,
831 contributing to the good defect tolerance properties.^[76a] On the contrary, DFT calculations by
832 Sun, Zhang, and co-workers identified a strong covalency of both the Pb cations and I anions
833 in β - MAPbI_3 (tetragonal room-temperature phase),^[94] leading to formation of Pb dimers and I
834 trimmers (**Figure 10b**).^[95] The consequence of the strong covalency in MAPbI_3 is that it leads
835 to deep charge-state energy levels (**Figure 10c**). For example, when iodine vacancy (V_I) is
836 generated, which leads to only a shallow-level state within the band gap, actually the structure
837 undergoes a significant distortion (because the V_I defect becomes negatively charged).
838 Furthermore, upon capture of an extra electron, the two Pb atoms that are originally separated
839 move towards each other and form a dimer (**Figure 10b**).^[95] On the basis of band structure
840 calculations, the formation of the Pb dimer leads to a deep defect level within the band gap
841 (**Figure 10c**).^[95] For the I_{MA} case, it has been proposed that the deep level state (**Figure 10a**)
842 arises from the formation of an I trimmer in the neutral state (**Figure 10a,b**).^[95] This work
843 highlights the importance of the dynamical processes taking place after a I-related defect is
844 generated in MAPbI_3 . Qi and co-workers proposed that the generation of I_2 would lead further
845 to subsequent degradation in a cascade effect highlighting the importance of iodine
846 management.^[79a, 96] Recently, it was shown that I_2 generation is mediated by $\text{I}_i^+/\text{I}_i^-$ defect pair
847 (**Figure 9c**).^[89] Du studied also the defects in β - MAPbI_3 by partially correcting the self-
848 interaction error and including the SOC.^[94] It was shown that only the I_i ^[94] and its complexes
849 (such as I_{MA}) induce deep levels inside the band gap, acting as nonradiative recombination
850 centers.^[97] γ - MAPbI_3 (orthorhombic low-temperature phase) was also studied with SOC to
851 show that Frenkel defects V_{Pb} , V_I , and V_{MA} are shallow-level defects and the Schottky defects
852 do not generate trap states within the band gap.^[92] Besides MAPbI_3 , intrinsic defects of Pb-free

853 halide perovskites such as CsSnI₃^[98] CsGeI₃^[99] halide double perovskites such as
854 Cs₂AgInBr₆^[100] Cs₂AgBiBr₆^[101] have also been systematically examined theoretically.

855
856 Most of theoretical studies show that the deep-level point defects of MAPbI₃ are related to iodine.
857 It should be paid more attention to this type of defects as point defects of perovskite especially
858 the deep level defects severely limit the performance of the solar cell due to the nonradiative
859 recombination losses caused by the defects. Having a good understanding of deep-level defects
860 can help us to develop suitable strategies to passivate these defects to achieve higher efficiencies
861 of PSCs.

862
863 For dimensional defects, they are formed by combining the point defects with defect pairs
864 including one-dimensional defects, i.e. edge dislocation in plain; two-dimensional defects, i.e.
865 the grain boundaries produced by differently oriented crystallites in contact; and three-
866 dimensional defects, i.e. volumetric defects produced by precipitation, voids and second-phase
867 domains (**Figure 9d**).^[90c] In addition to perovskite bulk properties, characterization of surfaces
868 and interfaces is equally important as they influence significantly on the performance of PSCs.
869 In the following subsections, the dimensional defects are separated into atomic structures and
870 defects of surfaces (i.e., the interface between perovskite atomic structure and a vacuum slab)
871 (**Section 4.1.2**), heterojunction interfaces (i.e., the boundary between perovskite and a
872 dissimilar material, e.g., ETL and HTL; **Section 4.1.3**), and grain boundary (i.e., the interface
873 between two adjacent perovskite atomic structured layers; **Section 4.1.4**) to be discussed.

874

875 **4.1.2. Surface defects**

876

877 In DFT calculations, the 3D periodic boundary condition is a requisite. The perovskite surfaces
878 are often modelled as a supercell slab with atomic structured layers and a vacuum layer.

879 Evaluation of the number of atomic layers and the top vacuum layer thickness is important to
880 ensure that the total DFT energy (e.g., surface formation energy) is not influenced by the
881 modelling parameters.^[90h] The atomic structure of surfaces of MAPbI₃,^[56, 102] MAPbBr₃,^[103]
882 and CsPbBr₃^[104] perovskites were described on the basis of DFT calculations. Various
883 thermodynamically stable MAPbI₃ surfaces along the different crystallographic directions such
884 as (110), (100), (101), and (001) were characterized.^[56, 102] Corroborated by STM studies
885 (**Section 2.4**),^[11, 26-27, 38, 42a-d] DFT calculations revealed that the (001) MAPbI₃ surface was the
886 most thermodynamically stable, hence it has been extensively modelled. Two different
887 terminations for the (001) MAPbI₃ surface found to be stable at room temperature were
888 proposed: PbI₂- and the MAI-terminated surface (**Figure 11a**).^[56, 102] The perovskite surfaces
889 were characterized to have some similarities in electronic properties compared to their bulk
890 counterparts. For example, these surfaces do not show the presence of neither deep surface
891 states nor shallow surface states; the valence and conduction bands are characterized by the I-
892 5p and Pb-6p orbitals. However, in comparison to their bulk structure, the surface of MAPbI₃
893 shows a larger band gap (**Figure 11b**). Experimentally, monolayers of ultrahigh vacuum
894 deposited MAPbI₃ films and scanned by STM revealed the presence of only MAI-terminated
895 surfaces.^[11, 26-27, 38, 42a-d] Similarly, vacuum cleaved MAPbBr₃ single crystals also revealed the
896 presence of only MABr-terminated surfaces.^[42a] A question prevails on the non-observation of
897 PbI₂- or PbBr₂-terminated surfaces experimentally under ultrahigh vacuum (UHV), which is
898 under investigation.^[42a] Nevertheless, it is pointed out that the preparation conditions of
899 perovskite polycrystalline films lead to a myriad of surface terminations in addition to the
900 introduction of several defects as probed by several techniques of XPS (i.e., non-stoichiometric
901 perovskite surface composition) and PL (i.e., carrier recombination events).^[19a, 72c, 105] The
902 several types of intrinsic point defects such as vacancies (V_I , V_{MA} , V_{Pb}), interstitials (I_i , Pb_i),
903 and anti-sites (Pb_i , Pb_{MA}) were simulated on the different MAPbI₃ terminated surfaces (**Figure**
904 **11b**).^[102c] The defect energy levels within the band gap and defect formation energy resulted

905 from surface point defects were analyzed. On the MAI-terminated surface, MA vacancies (V_{MA})
906 can be easily formed due to low formation energy (i.e., high volatility of MA^+). However, V_{MA}
907 does not lead to the deep defect state meaning that very few carrier traps form on the MAI-
908 terminated surface regardless of sample preparation conditions. When the perovskite film is
909 prepared under I-rich conditions, excess of I in the form of iodine interstitials (I_i) can be
910 introduced. This I_i on both MAI- and PbI_2 -terminated surfaces has a remarkably low formation
911 energy (-0.03 eV) and leads to deep carrier-trapping states. Recently, Meggiolaro, Mosconi,
912 and De Angelis proposed an alternative model of the dynamics of I_i^-/V_I^+ Frenkel pair defect
913 formation (charge neutrality is obeyed) at the surfaces of $MAPbI_3$ (**Figure 11c**).^[56] The
914 formation of an interstitial iodine (I_i^-) is followed by the formation of iodine vacancy (V_I^+) upon
915 stimulus (e.g., photo, thermal, etc.), that could take place in the bulk or at different terminated
916 surfaces (**Figure 11c**). However, formation of the I_i^-/V_I^+ Frenkel pair defect is favorable at the
917 surface than in bulk because of the steric hindrance required to accommodate the extra iodine
918 in the bulk lattice. Despite the fairly high density of defects determined experimentally (**Table**
919 **2**) in the order of 10^{16} to 10^{18} cm^{-3} , only the less abundant I_i defects were shown to introduce
920 deep electron/hole traps in $MAPbI_3$.^[106]

921
922 The above discussions highlight the negative impact of excessive iodine on the performance of
923 PSCs and the importance of iodine management or surface passivation for enhancing PCE
924 (**Table 2**).^[79a, 89, 96, 102c, 106]

925

926 **4.1.3. Interfacial defects**

927

928 When two materials with different structural symmetries are contacted together forming an
929 heterojunction interface, the physico-chemical interactions may lead to complex structural
930 faults, distortions, and stoichiometrically deficient interfaces.^[107] The electronic structures of

931 the heterojunction interfaces formed with perovskites were described by UPS and XPS
932 techniques. However, the atomic structure of the heterojunction interface such as the type of
933 coordination formed was mainly described by computational simulations due to lack of
934 experimental tools to probe the buried interfaces. In this sub-section we focus on the theoretical
935 description of defects at the two interfaces of perovskite/ETL and perovskite/HTL systems.

936

937 The atomic structure of perovskite/ETL interfaces such as MAPbI₃/TiO₂,^[87a, 108] MASn_xPb_{1-x}
938 I₃/TiO₂,^[109] MAPbI₃/ZnO,^[110] MAPbI₃/C60^[102e], MAPbI₃/PCBM,^[102f] α-FAPbI₃/TiO₂,^[111]
939 CsPbBr₃/TiO₂^[112] were described using first-principle calculations. In particular, the interfacial
940 atomic structure and the electronic properties of the interface between TiO₂ and MAPbI₃ were
941 extensively studied, which is discussed next.^[87a, 102e, 102f, 108] On the planar TiO₂, they found that
942 MAPbI₃ and MAPbI_{3-x}Cl_x perovskite grows preferentially with (110)-oriented film than (001)
943 orientation.^[108a] The TiO₂ with the (110)-oriented perovskite has a stronger interaction, leading
944 to a stronger interfacial coupling and to TiO₂ conduction band energy upshift. On the meso-
945 structured TiO₂ (MS-TiO₂), by combining several spectroscopic techniques it was also
946 demonstrated that the perovskite close to the MS-TiO₂ surface was locally ordered, which was
947 induced by interfacial interactions. The locally ordered layer enhances generation of free charge
948 carriers and efficient charge carrier transport to the contact.^[108d] Transfer of the photoexcited
949 electrons in MAPbI₃/planar TiO₂ is more difficult compared to MAPbI₃/MS-TiO₂.^[108f] This
950 may account for the reason why PSCs based on the MS-TiO₂ usually show better performance
951 than those based on the planar TiO₂. It seems that no deep defect states were found at the
952 MAPbI₃/TiO₂ interface, which is consistent with experimental observations that the
953 MAPbI₃/TiO₂ interface is more electrically active than the MAPbI₃/HTL interface.^[113] The
954 residual PbI₂ at grain boundaries of MAPbI₃ was shown to have a detrimental impact on the
955 performance of PSCs.^[114] However, PbI₂ at the interface of MAPbI₃/TiO₂ can enhance the
956 interfacial electronic coupling.^[108c] The calculated results are also consistent with the

957 experimental results.^[115] A few studies describe the atomic structures at perovskite/HTL
958 interfaces based on DFT calculations.^[102a, 102b] By examining the various types of PbI_x
959 polyhedron terminations, a PbI_x vacant-type terminated surface is not beneficial to the hole
960 transfer to the HTL. PbI_2 -rich terminated surface enables the photogenerated holes to transfer
961 to HTL smoothly. This is in agreement with another reported calculation, which shows that
962 nonpolar MAPbI_3 (001) and (110) surface tends to favor hole injection to Spiro-OMeTAD.^[102f]
963 While, for PCBM, it is the polar MAPbI_3 (100) surface that tends to facilitate electron transfer
964 to PCBM due to largely delocalized surface states and orbital coupling.^[102f]

965
966 DFT calculations show that heterojunction interfaces can lead to defect states within the band
967 gap, impacting significantly not only solar cell efficiency, but also stability and hysteresis. The
968 passivation of the interface between the perovskite layer and HTL / ETL are vital to the further
969 improvement of the solar cell performance.

970

971 **4.1.4. Grain boundary**

972

973 In regard to dimensional defects, grain boundaries are a central discussion in perovskite
974 research. The formation of grain boundaries is inevitable as perovskite films for PSCs are
975 fabricated with multicrystalline nature. It is well-known that grain boundaries play a vital role in
976 conventional inorganic photovoltaic polycrystalline absorbers (GaAs, CIGS, CZTS, and CdTe).
977 Grain boundaries produce deep trap states within the bandgap, which in turn increase carrier
978 recombination rate and reduce V_{oc} significantly.^[116] The coincidence site lattice (CSL) model
979 is a mathematical tool often employed to characterize grain boundaries in computational
980 studies.^[117] This model provides the idea that grain boundaries are not formed randomly based
981 on the principle of energy minimization of the system upon its formation. Briefly, a grain
982 boundary is modeled as two adjacent grains connected forming an interface (**Figure 12**).^[117d]

983 This interface or grain boundary can be generated by (i) the two aligned adjacent lattices of
984 grains (or Ruddlesden-Popper faults), (ii) twisting a grain with the axis of rotation
985 corresponding to the normal plane, (iii) tilting a grain with the axis of rotation perpendicular to
986 the normal plane, or by a combination of all the geometrical operations above (Figure 12).^[117d]
987 The atomistic models of grain boundaries will exhibit a variety of interfacial structures. Because
988 of the periodicity in the crystal structure, the geometrical operations above (Figure 12) may
989 also generate atomic arrangements at the interface with certain periodical features (suitable for
990 DFT calculations). The grain boundaries that have a certain number of atoms sharing the same
991 lattice in both of two adjacent grains (or CSL) are of particular interest in many computational
992 studies due to their periodicity (i.e., a more realistic non-periodic atomic structures require large
993 computational efforts). These special type of grain boundaries are distinguished by the
994 reciprocal of $\Sigma = (\text{number of coincidence sites in the unit cell}) / (\text{number of all lattice sites in}$
995 $\text{the unit cell})$ value and specifying the combination of the grain boundary planes (Figure
996 12a).^[117] For easy visualization, some of the crystallographic planes for β -MAPbI₃ are provided
997 in ref. ^[118]. A large reciprocal value of Σ means the periodicity is long-ranged (characterized as
998 random boundary). This random boundary possesses a high interfacial energy because the
999 atomic arrangement differs significantly from its original bulk structure.^[117b] On the contrary,
1000 low Σ values have short-range periodicity (i.e., larger number of atomic coordination at the
1001 boundary interface between two adjacent grains), thus leads to lower interfacial energy than
1002 random boundaries. Yan and co-workers provided the first DFT calculations of [100](111) Σ 3,
1003 which corresponds to a twin grain boundary with two (111) planes of MAPbI₃ oriented along
1004 [100] direction (Figure 12a; i.e., the simplest boundary when the crystals on each side of a
1005 plane correspond to mirror images of each other. There is no region of disorder and the
1006 boundary between the twinned crystals will be a single plane of periodic atoms. DFT
1007 calculations showed that [100](111) Σ 3 structured grain boundaries are electronically benign,

1008 i.e. they do not introduce deep trap states.^[76] The other type of [100](310) Σ 5, which also shows
1009 symmetric and periodic atomic structured grain boundary (supercell depicted in **Figure 12b**)
1010 was considered based on the fact that atomic structure in this type of grain boundary was
1011 previously observed in SrTiO₃ perovskite by high resolution transmission electron microscopy
1012 (HR-TEM).^[119] MD simulations were performed on the [100](310) Σ 5 grain boundary (**Figure**
1013 **12b**) at 300 K to implement the temporal evolution of structural disorder and imperfections due
1014 to thermal fluctuations. MD simulations were unable to show generation of deep defects states
1015 within the band gap.^[76, 119a] The grain boundary sites in [100](310) Σ 5 were found to increase
1016 the hole effective mass leading to only shallow trap state near VBM.^[76b]

1017
1018 Experimental mapping of grain boundaries in organic lead halide-based perovskites is
1019 challenging because of their inherent sensitivity to vacuum and when exposed to excitation
1020 probes (e.g., electron beam, X-ray, light, etc.).^[79a] In contrast, inorganic perovskites (e.g.,
1021 CsPbBr₃) have a better structural stability and efforts have been made to characterize the grain
1022 boundaries by electron microscopy techniques.^[8a, 120] For example, Mishra and co-workers
1023 determined the atomic structures of grain boundaries in inorganic CsPbBr₃ perovskite
1024 nanocrystals by scanning transmission electron microscopy-annular dark field (STEM-HAADF)
1025 imaging combined with DFT modeling (**Figure 12c**).^[8a] The grain boundary planar defects of
1026 Ruddlesden-Popper (RP) and Br-terminated and Br-deficient [001](210) Σ 5 were identified.
1027 Statistically, the Br-terminated [001](210) Σ 5 type grain boundary was the majority (amounting
1028 to 19 out of 42 analyzed). Other type of asymmetrical grain boundaries such as
1029 [001](110)(260) Σ 17 were also identified, but with a lower frequency of occurrence. The other
1030 typical planar defect analyzed is the RP planar faults, which consists of two CsBr layers stacked
1031 between two CsPbBr₃ domains. The RP planar faults propagate along the (010) and (100) planes
1032 forming a 90° steps at each intersection (**Figure 12c**). Further examination of the band diagram

1033 across the grain boundary reveals that neither of Br-terminated $[001](210)\Sigma 5$, RP planar fault,
1034 as well as $[001](110)(260)\Sigma 17$ induce deep defect levels. However, the Br-deficient
1035 $[001](210)\Sigma 5$ associated with the presence of Pb dangling bonds or Pb-Pb bonds were identified
1036 to lead to deep trap levels. Calculations by Guo, Wang, and Saidi also corroborates that grain
1037 boundaries in CsPbX_3 ($X = \text{Cl, Br, and I}$) as well as MAPbI_3 perovskites do not generate midgap
1038 states inducing only shallow states near the VBM.^[121] As comparison, grain boundaries in lead-
1039 free halide double perovskites of $\text{Cs}_2\text{AgInCl}_6$, $\text{Cs}_2\text{AgBiCl}_6$,^[122] as well as kesterite of
1040 $\text{Cu}_2\text{ZnSnSe}_4$,^[123] were also evaluated using DFT. The simulated $[001](310)\Sigma 5$ grain boundaries
1041 of $\text{Cs}_2\text{AgInCl}_6$ and $\text{Cs}_2\text{AgBiCl}_6$ and $[001](114)\Sigma 3$ grain boundaries of $\text{Cu}_2\text{ZnSnSe}_4$ with low-
1042 formation-energy can result in deep-level defect states in the bandgap and act as the carrier
1043 recombination centers deteriorating their optoelectronic properties.

1044
1045 According to the simulation results, to increase photon-to-electron conversion efficiencies,
1046 grain boundary passivation was suggested. To date, although there are experimental reports
1047 about the beneficial roles of grain boundaries in separating and collecting charge carriers
1048 efficiently,^[10b] there is also experimental evidence showing that grain boundaries notably
1049 deteriorate the film optoelectronic properties (**Section 2**).^[12d, 14e, 19a, 124] Hence, passivation of
1050 grain boundaries generally enhances the PV performance as well as decreases the hysteresis
1051 phenomenon in the J-V curves. For instance, although MAPbI_3 grain boundaries leads to defects
1052 close to VBM that can still acts as a shallow hole trap states, the spontaneous passivation of
1053 extrinsic elements such as Cl (in $\text{MAPbI}_{3-x}\text{Cl}_x$)^[76b, 125] and O (from air exposure process)^[76b]
1054 can weaken the wrong bonds at grain boundaries and thus reduce the shallow trap states.^[76b]
1055 Other calculated results^[125] also demonstrated that the introduction of substitutional Cl dopants
1056 at the $[001](012)\Sigma 5$ grain boundary of MAPbI_3 is beneficial in reducing the electron-hole
1057 recombination events.^[12d, 14e, 19a, 124] These studies highlight that the role of defect tolerance in

1058 grain boundaries as well as grain boundary induced deterioration of pristine perovskite
1059 optoelectronic properties as the fundamental origin.

1060

1061 **4.2. Passivation strategies**

1062

1063 Thanks to the theoretical and experimental tools to detect the defects, a deep understanding of
1064 the defects of perovskite is obtained. Defects especially the deep-level defects are proven to
1065 result in nonradiative recombination losses and limit the performance of the resultant PSCs.^[58a]
1066 It is necessary to develop effective approaches to decreasing the defect density. Several
1067 strategies have been developed, which can successfully passivate defects including point
1068 defects and dimensional defects of surface, interfacial and grain boundary defects (summarized
1069 in [Table 2](#)).

1070

1071 **4.2.1. Point defects passivation**

1072

1073 The common route to passivate point defects is by adding dopants or additives in the perovskite
1074 precursor solutions to minimize the defect formation during the perovskite growth process. The
1075 dopants or additives of inorganic dopants such as K^+ , Ni^{2+} , I_3^- , Al^{3+} , Cs^+ and Rb^+ ions^[96a, 126]
1076 and organic dopants such as MA^[127] and 2,3,5,6-Tetrafluoro-7,7,8,8-tetracyanoquinodimethane
1077 (F4TCNQ)^[128] are successfully applied into the precursor solutions to passivate the different
1078 type of defects density in different degrees. In addition to adding dopants or additives, light has
1079 impact on the defect density. It was found that under the light irradiation, the
1080 photoluminescence quantum efficiency was enhanced.^[129] Combined with theoretical
1081 investigations, they proposed that the light irradiation promotes the annihilation of V_I^+/I_i^-
1082 Frenkel pairs. Recently, a new behavior in hybrid perovskite was proposed that local distortions
1083 can be passivated under light illumination.^[130] Mohite and co-workers found that a uniform

1084 lattice expansion in hybrid perovskite thin films of $\text{FA}_{0.7}\text{MA}_{0.25}\text{Cs}_{0.05}\text{PbI}_3$ occurred under
1085 continuous light illumination. After passivation by light, PCE was enhanced from 18.5 to 20.5%
1086 with improved stability. However, it was proposed that the limited stability of organometallic
1087 PSC during long solar irradiation was due to the formation of light-activated meta-stable deep-
1088 level trap states.^[130-131] Long light exposure time is detrimental for the performance. They also
1089 mentioned that it can self-heal completely by resting them in dark.

1090

1091 The performance of PSCs enhanced after passivation of point defects in perovskite. However,
1092 compared with single crystals, perovskite grains behaving as large dimensional defects
1093 including surface defects and grain boundaries play a vital role in the influence of the PSC
1094 performance. The degradation of perovskite grains was studied to be triggered by the defective
1095 surface and grain boundaries.^[132] It is desirable to passivate these dimensional defects to boost
1096 the performance. In the next subsections, passivation strategies on dimensional defects are
1097 described.

1098

1099 **4.2.2. Surface/Interface passivation**

1100

1101 Theoretical studies of defects ([Section 4.1](#)) are often divided into the surface defects (i.e., the
1102 interface between perovskite atomic structure and a vacuum slab) and interface defects (i.e., the
1103 boundary between perovskite and a dissimilar material). As the perovskite layer directly
1104 contacts HTL and ETL in PSCs, the surface/interface passivation are discussed together in this
1105 section according to the contact layer, i.e., at the perovskite/ETL interface and perovskite/HTL
1106 interface. For the surface/interface passivation, a number of passivation molecules were applied
1107 on the surfaces of perovskites as they serve as electron donors or electron acceptors, which can
1108 interact with charged defects in perovskite.

1109

1110 For perovskite/ETL interface passivation, a fullerene derivative material of PCBM was firstly
1111 introduced to passivate the interface of MAPbI₃/C₆₀ in the structure of
1112 ITO/PEDOT:PSS/MAPbI₃/passivation layer/C₆₀/BCP/Al by depositing it on the surface of
1113 perovskite layers.^[133] The resulted PSC exhibited negligible photocurrent hysteresis and
1114 improved device performance. PCBM effectively passivated the trap defects on the surface by
1115 almost two orders of magnitude decrease in the range of energy level above 0.40 eV. Other
1116 fullerene derivative material such as ethanolamine (ETA)-functionalized fullerene C₆₀-ETA
1117 was also successfully introduced to further passivate the TiO₂:TOPD (titanium oxide bis(2,4-
1118 pentanedionate)) surface in PSC with a glass/ITO/TiO₂:TOPD/C₆₀-ETA or [6,6]-phenyl-C-61-
1119 butyric acid methyl ester (PC60BM) /MAPbI₃/Spiro-OMeTAD/Au architecture.^[134] Besides
1120 fullerene derivative material such as π -conjugated Lewis base with n-type semiconductor
1121 property,^[135] the chloride can also efficiently passivate charged defects induced by both the
1122 cationic and anionic defect sites in the structure of ITO/PTAA/MAPbI₃/functional layer (L- α -
1123 phosphatidylcholine, choline iodide or choline chloride)/C₆₀/BCP/Cu.^[136] TiO₂, a typical and
1124 common used ETL, behaves as photocatalyst degrading perovskite. CsBr as an interfacial
1125 modifier between perovskite/ETL not only passivated trap states to improve the PCE from 11.5
1126 to 15.3%, but also inhibited the photocatalytic active sites on the TiO₂ to enhance the stability
1127 under UV irradiation.^[137] As discussed before (**Section 4.1.3 Interfacial defects**), the planar
1128 TiO₂ with the (110)-oriented perovskite has a stronger interaction, leading to a stronger
1129 interfacial coupling. However, so far the perovskite cannot be well-prepared with all the (110)-
1130 oriented perovskite. To enhance the interfacial binding in planar PSCs, the interfacial Cl atoms
1131 on the TiO₂ colloidal nanocrystals was introduced.^[1081] It forms stronger binding and also
1132 suppressed deep trap states at the TiO₂/FA_{0.85}MA_{0.15}PbI_{2.55}Br_{0.45} perovskite interface and thus
1133 considerably reduce interfacial recombination.

1134

1135 Other than TiO_2 , SnO_2 is also well developed for high performance PSCs specially with a planar
1136 structure. Compared with TiO_2 , SnO_2 shows higher mobility and chemical stability, and the
1137 SnO_2 layer can be readily deposited by low temperature solution coating,^[138] commercially
1138 available precursor solutions,^[82a, 84d] atomic layer deposition (ALD),^[139] sputtering
1139 deposition^[84a] and chemical bath,^[140] which all show performance over 20%. Qi and coworkers
1140 found that for the sputtered SnO_2 , the gap states close to the valence band of SnO_2 significantly
1141 deteriorated the device performance.^[84a] The passivation of the SnO_2 surface helped improve
1142 the performance with reduced hysteresis. Liu and coworkers applied ethylene diamine
1143 tetraacetic acid (EDTA) to passivate the commercially available SnO_2 nanocrystals.^[141] The
1144 energy level for the EDTA passivated SnO_2 is better aligned with the conduction band of
1145 perovskite thus a higher V_{OC} and a certified 21.52% PCE were obtained. The passivation of
1146 SnO_2 with EDTA not only improves the efficiency, but also enhances the device operational
1147 stability under light illumination. Fullerene and its derivatives are also good candidates to
1148 modify SnO_2 for high performance PSCs.^[142] Zhan, Meng, Tu and coworkers developed a
1149 fullerene derivative 9-(1-(6-(3,5-bis(hydroxymethyl)phenoxy)-1-hexyl)-1H-1,2,3-triazol-4-
1150 yl)-1-nonyl [60]fullerenoacetate (C9), and anchored C9 to the surface of SnO_2 ETL.^[143] The
1151 anchored C9 could efficiently passivate the oxygen-vacancy-related defects on the surface of
1152 the SnO_2 and suppresses charge recombination. The reduced injection barrier also enhanced
1153 charge extraction. Li and coworkers introduced NH_4Cl into commercial SnO_2 precursors and
1154 found that NH_4Cl induced the coagulation of SnO_2 colloid and enhanced electron mobility with
1155 a better energy level alignment.^[144] The introduced NH_4^+ and Cl^- could suppress the formation
1156 of deep-level defects thus optimize the SnO_2 /perovskite interface and reduce charge
1157 recombination.

1158

1159 Regarding the studies on perovskite/HTL interface, the organic Lewis bases of thiophene and
1160 pyridine was firstly introduced to passivate the $\text{MAPbI}_{3-x}\text{Cl}_x$ /Spiro-OMeTAD interface,

1161 inducing less defect density and enhanced performance.^[19b] Snaith and co-workers proposed
1162 that the Lewis bases could passivate under-coordinated Pb ions in the perovskite crystal via the
1163 coordinate bonding between the sulfur atom in thiophene or nitrogen atom in pyridine with
1164 under-coordinated Pb ions in the perovskite. Other organic passivation materials such as PCBM
1165 was also reported to passivate perovskite/spiro-OMeTAD interface through passivation of
1166 under-coordinated I atoms (I^-) at the surface.^[145] Besides organic passivation materials (such
1167 as poly(methyl methacrylate) (PMMA)^[146]), ionic material such as MABr was also used to
1168 passivate the perovskite/Spiro-OMeTAD interface.^[147] Mhaisalkar, Mathews and co-workers
1169 proposed the ions (MA^+ and Br^- ions) can diffuse into the vacancies created by the loss of
1170 organic cations and I^- , thus passivate the defects. The modification of the perovskite layer with
1171 an ultra-thin inorganic layer like Al_2O_3 could also enhance the perovskite stability against
1172 humidity.^[148] Koushik and coworkers introduced an ultra-thin Al_2O_3 layer by ALD which could
1173 effectively protect the perovskite layer against humidity. In the meantime, charges could also
1174 transfer efficiently and the performance was improved with an optimized Al_2O_3 thickness.
1175 Although 3D perovskite materials have stronger light absorption and good charge carrier
1176 transport properties than 2D perovskites, their moisture stability is inferior to 2D perovskites
1177 considering the hydrophobic feature of the large organic cations in 2D perovskite segment. To
1178 combine their advantages, a 2D layered PEA_2PbI_4 perovskite layer was in situ grown on the
1179 surface of 3D perovskite film to improve the stability of PSCs.^[149] In addition, the thin 2D
1180 layers also have defect passivation effect to enhance the performance.^[150] Paetzold and
1181 coworkers recently created a hybrid 2D/3D perovskite heterostructure by spin coating n-
1182 butylammonium bromide on a wide band-gap perovskite absorber layer.^[151] This thin 2D
1183 perovskite layer efficiently mitigated non-radiative recombination and exhibits a record Voc of
1184 1.31 eV for a wide band gap (1.72 eV) PSCs with a standard structure. Recently, the
1185 performance of normal structured PSCs passivated by the organic halide salt phenyl ethyl-
1186 ammonium iodide (PEAI) was shown to be superior than that of passivated by the 2D layered

1187 PEA_2PbI_4 perovskite at the interface of $\text{FA}_{1-x}\text{MA}_x\text{PbI}_3/\text{spiro-OMeTAD}$.^[84d] The highest
1188 certified efficiency of 23.32% has been achieved by employing PEAI to suppress the surface
1189 defects of perovskite. As in the inverted structure PSCs, the bottom hole transport layer will
1190 influence the growth of the perovskite layer and its quality. The above-mentioned post growth
1191 process also works for inverted structured PSCs. Zhu, Snaith and coworkers developed a
1192 solution-processed secondary growth technique to enhance V_{oc} of inverted planar structured
1193 PSCs.^[49o] To improve the wettability of the perovskite solution on the bottom HTL PTAA, a
1194 pre-treatment with dimethylformamide (DMF) was applied. With a high-quality perovskite
1195 layer, the solution-processed secondary growth on top of perovskite helped produce a wider
1196 bandgap top layer and also mitigated non-radiative recombination, thus a high V_{oc} of 1.21 eV
1197 was obtained for perovskite with a band gap of 1.62 eV.

1198
1199 As the passivation of perovskite/ETL and perovskite/HTL are beneficial to reduce defects at
1200 the surfaces, it is easy to consider to minimize defects at both interfaces. For example, the
1201 passivated PSCs inserting an ultrathin PMMA films at both the perovskite/Spiro-OMeTAD and
1202 perovskite/ TiO_2 interfaces boosted the V_{oc} from 1.17 eV (passivated PSCs only at
1203 perovskite/ TiO_2 interface) to 1.21 V.^[152] PbI_2 was also applied as passivation layer and a
1204 double-side-passivated PSCs by distributing PbI_2 to both front/rear-side surfaces yielded PCE
1205 of 22.3%, which was better than the device with only passivation in the perovskite/Spiro-
1206 OMeTAD interface of PCE 21.6% and without passivation of 18.8%.^[115] The performance of
1207 PSCs was further enhanced after both side interface passivation compared to only one side
1208 interface passivation. Therefore, passivation of both interfaces (ETL/perovskite and
1209 perovskite/HTL) to further reduce defects is key to further improving the optoelectronic
1210 properties of PSCs.

1211

1212 **4.2.3. Grain boundary passivation**

1213

1214 In the former section ([Section 4.1.4](#)), we introduced and analyzed the theories of defects on the
1215 different types of grain boundaries. However, in real PSCs, it is difficult to control grain
1216 boundary structure and chemical composition during formation of perovskite films due to
1217 generally fast growth process and a large number of formed grains. Furthermore, it is also
1218 difficult to assign whether the passivation contributes to the interface passivation or grain
1219 boundary passivation. For instance, the passivation effect of chloride on perovskite surface
1220 treatment was comparable to those with blending the chemicals in the precursor solution, i.e.
1221 the post surface treatment of perovskite may be enough to passivate the grain boundaries in
1222 bulk.^[136] Considering these cases, we discuss grain boundary passivation according to two
1223 common methods: 1) post-treatment of passivation molecules on the perovskite films with large
1224 grain sizes and 2) one-step passivation treatment of grain boundaries with additives in the
1225 precursor solution.

1226

1227 The first approach is to decrease defects by reducing the area of grain boundaries with larger
1228 grain size. Many efforts have been investigated to obtain large grain size by varying the
1229 preparation method such as thermal annealing,^[153] solvent annealing with N,N-
1230 dimethylformamide ^[154] or dimethyl sulfoxide,^[155] hot-casting technique,^[156] recrystallize the
1231 perovskite film^[157] and tuning the precursor solution by tuning the concentration^[158] or adding
1232 additives.^[159] The grain size of MAPbI₃ crystal can be enlarged from 100-300 nm to
1233 micrometer-scale or even to millimeter-scale crystalline grains (1 to 2 mm)^[156]. Larger grain
1234 size of perovskite was shown to have reduced trap density. The resultant PSCs with larger grain
1235 size exhibited an enhanced performance including enhanced J_{sc} and V_{oc}. They usually inclined
1236 to ascribe the enhanced J_{sc} to the thicker active layer with improved light-harvesting property
1237 and the enhanced V_{oc} to decrease in trap density. The second approach has focused on the usage
1238 of additives mixed with the precursor perovskite solutions to passivate the defects in grain

1239 boundaries during the crystal growth. Especially, the Pb and I related defects, such as under-
1240 coordinated Pb^{2+}/I species and Pb-I antisite defects, in grain boundary will deteriorate the PSCs
1241 performance and need to be passivated. Various additives are applied to successfully passivate
1242 the defects in grain boundaries, such as D- π -A molecules,^[126d] methimazole (MMI),^[114]
1243 F4TCNQ,^[128] guanidinium (GA),^[160] ethyl 2-cyanoacrylate (E2CA),^[161] 1H,1H-
1244 perfluorooctylamine (PFA)^[162] and semiconducting molecules with Lewis base or acid
1245 functional groups including 7,7'-[4,4-Bis(2-ethylhexyl)-4H-silolo[3,2-b:4,5-b']dithiophene-
1246 2,6-diyl]bis[6-fluoro-4-(5'-hexyl-[2,2'-bithiophen]-5-yl)benzo[c][1,2,5]thiadiazole] (p-
1247 DTS(FBTTh₂)₂ (abbreviated as DTS), benzodithiophene (BDT) unit based DR3TBDTT
1248 (DR3T)^[163] and PCBM.^[164] After the introduction of these additives, different types of the Pb
1249 and I related defects were passivated and the performance of the PSCs with reduced defects
1250 improved.

1251
1252 These studies suggest that perovskites with larger grain sizes and less defects in grain boundaries
1253 (especially those defects related to lead and iodine) are beneficial to fabricate high-performance
1254 PSCs. Overall, passivation of intrinsic point defects, interfacial defects, and grain boundary
1255 defects have been shown to remarkably increase PCE, demonstrating the importance of these
1256 defect passivation in the cell performance. Although several passivation molecules are provided
1257 to reduce the different types of defects (**Table 2**), new types of passivation materials and
1258 techniques need be explored. The new strategies of simultaneous passivation of various types
1259 of defects present in perovskites are expected to boost the performance of PSCs closer to their
1260 theoretical limit.

1261

1262 **5. Conclusion and outlook**

1263

1264 In this review, our central focus was to analyze recent advances of metal halide PSCs from the
1265 perspective of surface science viewpoint. Surfaces and interfaces in perovskites play major role
1266 on the current technological challenges in PSCs such as performance, reproducibility, hysteresis,
1267 and stability. For example, efficient generation of charges, extraction, and transport with
1268 minimum recombination events through optimized interfaces is crucial to attain high efficiency.
1269 These interfaces can be in the form of (i) grain boundaries and/or sub-grain boundaries within
1270 a polycrystalline film composed of the same material,^[165] (ii) heterojunction interfaces (i.e., the
1271 boundary between perovskite and a dissimilar material, e.g., ETL and HTL), (iii) surfaces (i.e.,
1272 the interface between perovskite atomic structure and a vacuum slab. The initial condition of
1273 the morphology, crystal orientation, and chemical composition at interfaces in the as-prepared
1274 films are not static; i.e., interfaces are expected to show a physico-chemical dynamical process
1275 over the course of solar cell operation time. As consequence, these will sensitively affect charge
1276 carrier dynamics induced by the changes in defect density and energy level alignments at the
1277 interfaces.^[11, 38, 84c]

1278
1279 Case studies that demonstrate the feasibility of bridging the gap between surface-science-
1280 related fundamental investigations and polycrystalline film technology applied to PSCs were
1281 discussed. The fundamental understanding of correlations between local electronic properties
1282 and morphologies to technologically relevant solar cell parameters have progressed
1283 significantly (**Section 2**). For example, AFM is a well-established SPM tool for characterizing
1284 grains, grain boundaries, and surface roughness.^[11, 38, 166] The morphology of the perovskite
1285 film as well as its adjacent functional layers play a crucial role in determining the overall
1286 performance of PSCs. Larger and oriented grains often lead to enhanced carrier mobility,^[167]
1287 reduced density of electronic traps (**Section 4**),^[25, 90b] and enhanced stability.^[132, 168] SPM with
1288 multi-modality imaging capability such as pc-AFM and KPFM provide a one-to-one correlation
1289 of photocurrent and photovoltage, respectively, to the local morphology (**Section 2.1** and **2.2**).

1290 There now exists a broad consensus that ion migration is the main mechanism governing the
1291 macroscopic phenomena of photocurrent, photovoltage, as well as anomalous electronic
1292 behavior including hysteretic I-V^[169] and switchable PV effects.^[36b] As discussed in **Sections**
1293 **2.1** and **2.2**, spatially-resolved mapping techniques revealed the preferential ion migration
1294 phenomena through grain boundaries in perovskite polycrystalline films. However, ion
1295 migration is not a phenomena taking place only in polycrystalline films, but it was also reported
1296 to take place in MAPbBr₃ single crystal (bulk transport)^[12c, 170] as well as across the planes of
1297 layered 2D perovskites in the form of single crystal^[171] and 2D polycrystalline films.^[172]
1298 Although ion migration was demonstrated to exist in PSCs, questions on (i) what are the
1299 characteristic time scales for different perovskites? and (i) how it compares with electronic
1300 dynamics of charge generation, transport, recombination remains elusive (**Figure 1c**). Great
1301 efforts are been made in the direction to characterize the time scale of ion migration on different
1302 perovskite systems. A complete understanding of the time scale dynamics (e.g., interplay of
1303 charges and ionic species) is expected to help design solar cells with reliable and stable current-
1304 voltage responses. The number of reported works on this topic is still scarce. However, this
1305 number is increasing due to new advances in SPM techniques that allows to perform fast
1306 scanning and study the electrical property dynamics (**Table 1**). For example, a high speed
1307 KPFM (16 s per image) was first described by Leite and co-workers^[90e] allowing to monitor in
1308 real-time the modifications of CPD maps in perovskite films. In the report by Jesse and co-
1309 workers,^[170a] ion migration probed in a lateral device structure of Au/MAPbBr₃ single
1310 crystal/Au showed a complex potential transient dynamics in the μ s time scale. Two processes
1311 with characteristic fast (electronic) and slow (ion migration) dynamics were probed by their
1312 fast-free force recovery (F³R)-KPFM technique indicating that the imaged dynamics are not
1313 simply electronic in nature. Hundreds of μ s was the characteristic time scale that the transient
1314 behavior in the potential mapping takes to reach equilibrium after the field across the device
1315 was applied. More recently, Ginger and co-workers^[172b] studied the dynamics of ion migration

1316 in 2D layered perovskites of $(\text{C}_4\text{H}_9\text{NH}_3)_2\text{PbI}_4$ employing time-resolved G-mode KPFM and fast
1317 free time-resolved electrostatic force microscopy (FF-trEFM). Under illumination, the
1318 photovoltage also equilibrates after hundreds of μs , a time scale that was associated with ion
1319 migration and also with dynamics of trapped electronic carriers that are overlapping (**Figure**
1320 **1c**). Finally, Berger and co-workers^[12c] performed time-resolved KPFM measurements with
1321 sub-ms time resolution on a cross-section of complete device of FTO/SnO₂/(MA-FA)Pb(I-Br)
1322 mixed perovskite/spiro-MeOTAD/Au. A localized interfacial charging forms at the photoanode
1323 interface within 3-10 ms after applying a forward bias to the device. Subsequently, after
1324 switching off the forward bias, these interfacial charges were stable for over 500 ms creating a
1325 reverse electric field in the cell. This asymmetry in the kinetics indicates the complex physico-
1326 chemistry of ion migration and stabilization of the ionic species leading to interfacial
1327 charges.^[10g, 90e] The longer stabilization of this reverse electric field is associated as cause for
1328 generating higher photocurrents observed during the reverse bias scan (in comparison to the
1329 forward bias scan) in the solar cell I-V measurements (hysteresis). In all the studies of ion
1330 migration dynamics described above, the current-voltage hysteresis in PSCs is dominated by
1331 the dynamics of the formation and release of ionic charges at the interfaces.

1332

1333 As highlighted in **Sections 2.3** and **4.2.3**, investigation of dynamics at the atomic level
1334 fundamental studies by STM/STS and TEM were reported to provide also unique knowledge
1335 that correlates with macroscopic observations in PSCs (**Table 1**). These include (i) perovskite
1336 surface reconstruction with characteristic dimmer structure of halides (I or Br)^[27, 42] in dark that
1337 transforms to the complex structure with characteristic one-dimensional valley and hill pattern
1338 upon light illumination. (**Figure 2a,b**) The new structure shows enhanced charge transport
1339 properties^[26] (associated with ferroelectric domains^[31-33]); (ii) The real-space spatial
1340 distribution of I and Cl anions on the surfaces of the $\text{MAPbBr}_{3-y}\text{I}_y$ and $\text{MAPbBr}_{3-z}\text{Cl}_z$ mixed
1341 halide perovskite probed by STM^[27] were found to be randomly distributed, which has

1342 implications on the halide segregation phenomena.^[40-41] (iii) The atomic structure of grain
1343 boundaries in CsPbBr₃ perovskites measured by STEM-HAADF^[8a] and DFT studies reveal the
1344 defect tolerance properties of Br-terminated interfaces of grain boundaries; Br-deficient grain
1345 boundaries were associated with the presence of Pb dangling bonds that lead to deep-trap levels.
1346 These recent studies show the relevance of atomic level studies that leads to the bridging of
1347 surface science studies to macroscopic parameters relevant to solar cell operation.

1348

1349 In contrast to local property investigations by microscopy techniques, ensemble averaged
1350 measurement techniques also play a pivotal role for the understanding of PSC operation
1351 principles (**Section 3**). The typical probing spot sizes of ensemble averaging techniques are in
1352 the micrometer to millimeter range, which are comparable to active area sizes in devices.
1353 Therefore, fundamental information extracted from such techniques can provide a direct
1354 relationship with solar cell parameters. For example, UPS and IPES are widely employed
1355 techniques in surface science to determine the quantities of IE, EA, E_F positions and WF on
1356 perovskite surfaces (**Section 3.1**).^[48-49] XPS is often employed for the surface chemical
1357 composition determination (**Section 3.2**), while LEED determines surface crystal structure
1358 (**Figure 5a**).^[39] An important consideration during the measurements regards the stability of
1359 perovskite materials under the environment (e.g., ambient air versus ultrahigh vacuum),^[79a]
1360 which modification (chemical, structural, defects) of the material leads to artifacts,
1361 complicating the interpretation of the results. Therefore, careful consideration of environmental
1362 conditions as well as interactions between perovskite and the excitation probe (electron beam,
1363 UV, X-ray, and electric field) are important factors for avoiding misinterpretation of the results
1364 obtained. PSC is generally composed of stacks of anode/cathode, a perovskite layer as absorber,
1365 and selective contact layers (ETL and HTL), resulting in multi-interfaces between these layers
1366 (**Figure 13**). Energy level alignments at these interfaces are a versatile tool for evaluating the
1367 charge extraction and transport at the interfaces (extended discussion in **Section 3.3**).^[48b] On

1368 the other hand, STM/STS, UPS, XPS studies are mainly performed in ultra-high vacuum (UHV),
1369 which presents a “pressure gap” between these UHV studies and perovskite solar cells that are
1370 operated in ambient pressure. How these UHV results can be related to the surface of real PSCs
1371 under ambient conditions is crucial, but is not well understood at this stage. The surface
1372 evolution under controlled environment will be an important future direction. Some of the
1373 surface properties can be studied by both UHV techniques and ambient techniques, it will be
1374 helpful to cross check the two sets of results to better understand the surface evolution between
1375 UHV and ambient. An example of such studies is that the work function of a thin film can be
1376 determined by both UPS (a UHV technique) and Kelvin probe (possible to be operated in
1377 ambient or controlled gas environment).^[173] Another example is that near-ambient pressure
1378 XPS studies can provide more insights about how the surface composition and morphology
1379 changes in ambient condition or controlled condition.^[174]

1380

1381 In situ studies and time dependent measurements monitoring the evolution of perovskite
1382 surfaces during, for example, degradation processes induced by thermal heating, upon
1383 controlled gas exposure (H_2O and O_2) and/or irradiation with photons (e.g., visible light, UV,
1384 and X-rays) are scarce.^[175] Similarly, in operando measurements on PSCs with synchrotron
1385 radiation techniques was discussed as a insightful method to study photovoltaic device
1386 dynamics under a number of different stimuli such as cooling/heating, current/ voltage, light,
1387 and environmental stressing conditions.^[175b, 176] An example of in operando measurements was
1388 accomplished on a MAPbI_3 -based solar cell by designing a sample stage for simultaneous I-V
1389 curve measurements dependent on temperature and synchrotron-based X-ray diffraction.^[176a]
1390 A detailed correlation between the perovskite crystal structure and I-V profiles was established
1391 on the same device sample, revealing insights into tetragonal to cubic phase transition
1392 temperature (60.5–65.4 °C).^[176a] In another study,^[176b] the crystallinity evolution correlated
1393 with device performance was performed with in situ GIWAXS and in operando J-V

1394 measurements. To investigate the solar cell performance evolution (in-operando), perovskite
1395 films starting from its precursor solutions were deposited on substrates with interdigitated back-
1396 contact with alternating HTLs and ETLs. These structures function as working solar cells when
1397 the precursor solution deposited across the electrodes solidifies to perovskite film (i.e.,
1398 photovoltaic activity). It is found that at the first stage of conversion from the precursor solution
1399 phase, a high V_{oc} is observed even though the bulk of the material is still present as precursors.
1400 This indicates that at the earlier stage of perovskite structure formation, the semiconductor band
1401 gap is already well-defined and free of sub-gap trap states. The J_{sc} continues to increase
1402 monotonically upon a solid bulk is initially formed within the film until a complete solid film
1403 is formed. This work reveals important dynamics among the different stages of perovskite film
1404 conversion and correlation to device performance. In addition, the enhanced pathways for
1405 charge diffusion during perovskite film conversion highlights the remarkable defect tolerance
1406 of perovskite materials.^[176b] The case studies above show that in operando measurements
1407 provide further unique insights into the dynamics of PSCs under real operation conditions,
1408 which will lead to a new front of technological advances in PSCs.

1409
1410 All the dynamical processes discussed in **Sections 2** and **3** are associated with the fundamental
1411 origin of defects in perovskites (**Section 4**). The presence of electronic defects within the band
1412 gap limits the efficiency, reproducibility, and stability of PSCs:^[90] (i) point defects in
1413 perovskites assist ion migration phenomena (**Figure 9a**);^[87] (ii) semiconductor behavior of p-
1414 type or n-type in MAPbI_3 determined by MA^+ vacancy (acceptor) and I^- vacancy (donor) type
1415 defects (**Figure 9b**);^[58a, 76a, 88] (iii) light-induced degradation in MAPbI_3 related to V_{I} and I_{i}
1416 Frenkel pair defects dynamics (**Figure 11c**).^[89] Therefore, efforts are been made in the direction
1417 to characterize experimentally the type of defects in perovskites and minimize defect density
1418 by well-controlled perovskite film fabrication technology. In fact, PSCs based on thin-sliced
1419 grain boundary free single crystals can be promising for attaining both high efficiency and

1420 enhanced stability. Mohamed, Bakr, and co-workers employed single crystal MAPbI₃
1421 perovskite sample (thickness = 20 μm) showing an outstanding PCE of 21.09% and FF up to
1422 84.3%.^[4] However, technological challenges such as upscaling of perovskite single crystals
1423 prevail currently and fabrication of polycrystalline films may be a viable route for upscaling
1424 processes considering fabrication costs.^[71b, 71d, 84b, 177] The analyses of strategies in device
1425 architectures (**Figure 13**) that led to the best lab-scale research-cell efficiencies provide
1426 important insights and promising trend that enhanced performance and stability can be achieved
1427 in PSCs and solar modules.^[3, 177c, 178] From a historical view point, developments of PSC
1428 architectures could be separated into three stages. In the first stage, the replacement of liquid
1429 electrolyte to solid state HTL was a major breakthrough;^[179] the second stage is characterized
1430 by the perovskite composition engineering;^[44] and the current third stage is characterized by
1431 the interface engineering (or passivation) that boosted the certified efficiencies higher than
1432 22.67%.^[83, 84d] For example, Noh, Seo and co-workers^[83, 180] employed n-hexyl trimethyl
1433 ammonium bromide (HTAB) inserted between P3HT and (FAPbI₃)_{0.95}(MAPbBr₃)_{0.05}
1434 perovskite layer. The (N⁺(CH₃)₃⁻) moiety in HTAB coordinates with defects in Pb²⁺
1435 undercoordinated defects in perovskites, while the aliphatic (C₆H₁₃⁻) moiety coordinates with
1436 P3HT via van der Waals interaction promoting self-assembly of P3HT on HTAB improving
1437 further hole extraction. This device structure led to the high certified PCE of 22.67% due to
1438 reduction of non-radiative recombination processes (i.e., defect passivation) and enhanced
1439 physical contact between perovskite and P3HT. In another recent work, You and co-workers^[84d]
1440 employed PEAI as a passivation material and spin-coating on top of FA_{1-x}MA_xPbI₃ (x ~ 0.08)
1441 perovskite films. This strategy leads to the certified PCE of 23.3% in the NREL chart.^[3] PEAI
1442 coating on the perovskite layer was proposed to heal defects by filling the iodine vacancies on
1443 the surface and at the grain boundaries.^[84d] In all examples above, the dynamical processes of
1444 the interactions between passivating molecule and defect in perovskite was described on the
1445 basis of DFT calculations.^[90j] It is important to note that identification of the different types of

1446 defects experimentally is imperative, but challenging (Section 4 and Table 2). In this regard,
 1447 computational studies are further expected to aid a more in-depth understanding of degradation
 1448 dynamics, interfacial properties, and the role of defects on efficiency and stability that can be
 1449 corroborated by surface science techniques.

1450

1451 Acknowledgements

1452 This work was supported by funding from the Energy Materials and Surface Sciences Unit of
 1453 the Okinawa Institute of Science and Technology Graduate University, the OIST R&D Cluster
 1454 Research Program, the OIST Proof of Concept (POC) Program, and JSPS KAKENHI Grant
 1455 Number JP18K05266.

1456

1457 Received: ((will be filled in by the editorial staff))

1458 Revised: ((will be filled in by the editorial staff))

1459 Published online: ((will be filled in by the editorial staff))

1460

1461 References

- 1462 [1] N.-G. Park, H. Segawa, *ACS Photonics* **2018**, *5*, 2970.
 1463 [2] K. Yoshikawa, H. Kawasaki, W. Yoshida, T. Irie, K. Konishi, K. Nakano, T. Uto, D.
 1464 Adachi, M. Kanematsu, H. Uzu, K. Yamamoto, *Nat. Energy* **2017**, *2*, 17032.
 1465 [3] *National Renewable Energy Laboratory (NREL). Research-Cell Efficiency Chart.*
 1466 <https://www.nrel.gov/pv/cell-efficiency.html> and *Champion Module Efficiency Chart.*
 1467 <https://www.nrel.gov/pv/module-efficiency.html> (Accessed August 11th).
 1468 [4] Z. Chen, B. Turedi, A. Y. Alsalloum, C. Yang, X. Zheng, I. Gereige, A. AlSaggaf, O.
 1469 F. Mohammed, O. M. Bakr, *ACS Energy Lett.* **2019**, *4*, 1258.
 1470 [5] Y. Wang, M. I. Dar, L. K. Ono, T. Zhang, M. Kan, Y. Li, L. Zhang, X. Wang, Y.
 1471 Yang, X. Gao, Y. Qi, M. Grätzel, Y. Zhao, *Science* **2019**, *365*, 591.
 1472 [6] S. Yang, S. Chen, E. Mosconi, Y. Fang, X. Xiao, C. Wang, Y. Zhou, Z. Yu, J. Zhao,
 1473 Y. Gao, F. De Angelis, J. Huang, *Science* **2019**, *365*, 473.
 1474 [7] (a) E. Aydin, M. De Bastiani, S. De Wolf, *Adv. Mater.* **2019**, *31*, 1900428; (b) B.
 1475 Chen, P. N. Rudd, S. Yang, Y. Yuan, J. Huang, *Chem. Soc. Rev.* **2019**, *48*, 3842; (c)
 1476 Y. Rakita, I. Lubomirsky, D. Cahen, *Mater. Horizons* **2019**, *6*, 1297.
 1477 [8] (a) A. S. Thind, G. Luo, J. A. Hachtel, M. V. Morrell, S. B. Cho, A. Y. Borisevich, J.-
 1478 C. Idrobo, Y. Xing, R. Mishra, *Adv. Mater.* **2019**, *31*, 1805047; (b) Y. Zhou, O. S.
 1479 Game, S. Pang, N. P. Padture, *J. Phys. Chem. Lett.* **2015**, *6*, 4827.
 1480 [9] (a) J. Shi, Y. Li, Y. Li, D. Li, Y. Luo, H. Wu, Q. Meng, *Joule* **2018**, *2*, 879; (b) W.
 1481 Tress, *Adv. Energy Mater.* **2017**, *7*, 1602358.
 1482 [10] (a) J.-J. Li, J.-Y. Ma, Q.-Q. Ge, J.-S. Hu, D. Wang, L.-J. Wan, *ACS Appl. Mater.*
 1483 *Interfaces* **2015**, *7*, 28518; (b) J. S. Yun, A. Ho-Baillie, S. Huang, S. H. Woo, Y. Heo,
 1484 J. Seidel, F. Huang, Y.-B. Cheng, M. A. Green, *J. Phys. Chem. Lett.* **2015**, *6*, 875; (c)
 1485 J. Xu, A. Buin, A. H. Ip, W. Li, O. Voznyy, R. Comin, M. Yuan, S. Jeon, Z. Ning, J. J.
 1486 McDowell, P. Kanjanaboos, J.-P. Sun, X. Lan, L. N. Quan, D. H. Kim, I. G. Hill, P.
 1487 Maksymovych, E. H. Sargent, *Nat. Commun.* **2015**, *6*, 7081; (d) Y. Kutes, Y. Zhou, J.
 1488 L. Bosse, J. Steffes, N. P. Padture, B. D. Huey, *Nano Lett.* **2016**, *16*, 3434; (e) S. Y.
 1489 Leblebici, L. Leppert, Y. Li, S. E. Reyes-Lillo, S. Wickenburg, E. Wong, J. Lee, M.

- 1490 Melli, D. Ziegler, D. K. Angell, D. F. Ogletree, Paul D. Ashby, F. M. Toma, J. B.
1491 Neaton, I. D. Sharp, A. Weber-Bargioni, *Nat. Energy* **2016**, *1*, 16093; (f) Z. Zhao, X.
1492 Chen, H. Wu, X. Wu, G. Cao, *Adv. Funct. Mater.* **2016**, *26*, 3048; (g) Y. Shao, Y.
1493 Fang, T. Li, Q. Wang, Q. Dong, Y. Deng, Y. Yuan, H. Wei, M. Wang, A. Gruverman,
1494 J. Shield, J. Huang, *Energy Environ. Sci.* **2016**, *9*, 1752.
- 1495 [11] L. K. Ono, Y. B. Qi, *J. Phys. Chem. Lett.* **2016**, *7*, 4764.
- 1496 [12] (a) D.-H. Kang, N.-G. Park, *Adv. Mater.* **2019**, *31*, 1805214; (b) P. Liu, W. Wang, S.
1497 Liu, H. Yang, Z. Shao, *Adv. Energy Mater.* **2019**, *9*, 1803017; (c) S. A. L. Weber, I.
1498 M. Hermes, S.-H. Turren-Cruz, C. Gort, V. W. Bergmann, L. Gilson, A. Hagfeldt, M.
1499 Graetzel, W. Tress, R. Berger, *Energy Environ. Sci.* **2018**, *11*, 2404; (d) J.-W. Lee, S.-
1500 H. Bae, N. De Marco, Y.-T. Hsieh, Z. Dai, Y. Yang, *Mater. Today Energy* **2018**, *7*,
1501 149.
- 1502 [13] (a) D.-Y. Son, J.-W. Lee, Y. J. Choi, I.-H. Jang, S. Lee, P. J. Yoo, H. Shin, N. Ahn, M.
1503 Choi, D. Kim, N.-G. Park, *Nat. Energy* **2016**, *1*, 16081; (b) C. Lu, Z. Hu, Y. Wang, K.
1504 Sun, B. Shen, C. Gao, C. Yang, J. Zhang, Y. Zhu, *Adv. Mater. Interfaces* **2019**, *6*,
1505 1801253.
- 1506 [14] (a) Z. Wu, S. R. Raga, E. J. Juarez-Perez, X. Yao, Y. Jiang, L. K. Ono, Z. Ning, H.
1507 Tian, Y. B. Qi, *Adv. Mater.* **2017**, *29*, 1703670; (b) X. Zheng, B. Chen, J. Dai, Y.
1508 Fang, Y. Bai, Y. Lin, H. Wei, Xiao C. Zeng, J. Huang, **2017**, *2*, 17102; (c) X. Zheng,
1509 Y. Deng, B. Chen, H. Wei, X. Xiao, Y. Fang, Y. Lin, Z. Yu, Y. Liu, Q. Wang, J.
1510 Huang, *Adv. Mater.* **2018**, 1803428; (d) F. Zhang, D. Q. Bi, N. Pellet, C. X. Xiao, Z.
1511 Li, J. J. Berry, S. M. Zakeeruddin, K. Zhu, M. Gratzel, *Energy Environ. Sci.* **2018**, *11*,
1512 3480; (e) T. Niu, J. Lu, R. Munir, J. Li, D. Barrit, X. Zhang, H. Hu, Z. Yang, A.
1513 Amassian, K. Zhao, S. Liu, *Adv. Mater.* **2018**, *30*, 1706576; (f) C.-T. Lin, F. De Rossi,
1514 J. Kim, J. Baker, J. Ngiam, B. Xu, S. Pont, N. Aristidou, S. A. Haque, T. Watson, M.
1515 A. McLachlan, J. R. Durrant, *J. Mater. Chem. A* **2019**, *7*, 3006; (g) Z. Wang, A.
1516 Pradhan, M. A. Kamarudin, M. Pandey, S. S. Pandey, P. Zhang, C. H. Ng, A. S. M.
1517 Tripathi, T. Ma, S. Hayase, *ACS Appl Mater Interfaces* **2019**, *11*, 10012; (h) S. Ye, H.
1518 Rao, Z. Zhao, L. Zhang, H. Bao, W. Sun, Y. Li, F. Gu, J. Wang, Z. Liu, Z. Bian, C.
1519 Huang, *J. Am. Chem. Soc.* **2017**, *139*, 7504; (i) M. Wang, B. Li, J. Yuan, F. Huang, G.
1520 Cao, J. Tian, *ACS Appl. Mater. Interfaces* **2018**, *10*, 37005; (j) W. Gao, K. Zielinski,
1521 B. N. Drury, A. D. Carl, R. L. Grimm, *J. Phys. Chem. C* **2018**, *122*, 17882; (k) S.
1522 Yang, J. Dai, Z. Yu, Y. Shao, Y. Zhou, X. Xiao, X. C. Zeng, J. Huang, *J. Am. Chem.*
1523 *Soc.* **2019**, DOI: 10.1021/jacs.8b13091; (l) W.-Q. Wu, Z. Yang, P. N. Rudd, Y. Shao,
1524 X. Dai, H. Wei, J. Zhao, Y. Fang, Q. Wang, Y. Liu, Y. Deng, X. Xiao, Y. Feng, J.
1525 Huang, *Sci. Adv.* **2019**, *5*, eaav8925.
- 1526 [15] M.-C. Shih, S.-S. Li, C.-H. Hsieh, Y.-C. Wang, H.-D. Yang, Y.-P. Chiu, C.-S. Chang,
1527 C.-W. Chen, *Nano Lett.* **2017**, *17*, 1154.
- 1528 [16] T. Hwang, D. Cho, J. Kim, J. Kim, S. Lee, B. Lee, K. H. Kim, S. Hong, C. Kim, B.
1529 Park, *Nano Energy* **2016**, *25*, 91.
- 1530 [17] G. E. Eperon, D. Moerman, D. S. Ginger, *ACS Nano* **2016**, *10*, 10258.
- 1531 [18] K. Lu, Y. Lei, R. Qi, J. Liu, X. Yang, Z. Jia, R. Liu, Y. Xiang, Z. Zheng, *J. Mater.*
1532 *Chem. A* **2017**, *5*, 25211.
- 1533 [19] (a) D. W. deQuilettes, S. M. Vorpahl, S. D. Stranks, H. Nagaoka, G. E. Eperon, M. E.
1534 Ziffer, H. J. Snaith, D. S. Ginger, *Science* **2015**, *348*, 683; (b) N. K. Noel, A. Abate, S.
1535 D. Stranks, E. S. Parrott, V. M. Burlakov, A. Goriely, H. J. Snaith, *ACS Nano* **2014**, *8*,
1536 9815.
- 1537 [20] L. S. C. Pingree, O. G. Reid, D. S. Ginger, *Adv. Mater.* **2009**, *21*, 19.
- 1538 [21] V. W. Bergmann, S. A. L. Weber, F. Javier Ramos, M. K. Nazeeruddin, M. Grätzel,
1539 D. Li, A. L. Domanski, I. Lieberwirth, S. Ahmad, R. Berger, *Nat. Commun.* **2014**, *5*,
1540 5001.

- 1541 [22] M. Cai, N. Ishida, X. Li, X. Yang, T. Noda, Y. Wu, F. Xie, H. Naito, D. Fujita, L.
1542 Han, *Joule* **2018**, *2*, 296.
- 1543 [23] S. Panigrahi, S. Jana, T. Calmeiro, D. Nunes, R. Martins, E. Fortunato, *ACS Nano*
1544 **2017**, *11*, 10214.
- 1545 [24] (a) A. Guerrero, E. J. Juarez-Perez, J. Bisquert, I. Mora-Sero, G. Garcia-Belmonte,
1546 *Appl. Phys. Lett.* **2014**, *105*, 133902; (b) C.-S. Jiang, M. Yang, Y. Zhou, B. To, S. U.
1547 Nanayakkara, J. M. Luther, W. Zhou, J. J. Berry, J. van de Lagemaat, N. P. Padture,
1548 K. Zhu, M. M. Al-Jassim, *Nat. Commun.* **2015**, *6*, 8397; (c) V. W. Bergmann, Y. Guo,
1549 H. Tanaka, I. M. Hermes, D. Li, A. Klasen, S. A. Bretschneider, E. Nakamura, R.
1550 Berger, S. A. L. Weber, *ACS Appl. Mater. Interfaces* **2016**, *8*, 19402; (d) Z. Li, C.
1551 Xiao, Y. Yang, S. P. Harvey, D. H. Kim, J. A. Christians, M. Yang, P. Schulz, S. U.
1552 Nanayakkara, C.-S. Jiang, J. M. Luther, J. J. Berry, M. C. Beard, M. M. Al-Jassim, K.
1553 Zhu, *Energy Environ. Sci.* **2017**, *10*, 1234; (e) J. Will, Y. Hou, S. Scheiner, U. Pinkert,
1554 I. M. Hermes, S. A. L. Weber, A. Hirsch, M. Halik, C. Brabec, T. Unruh, *ACS Appl.*
1555 *Mater. Interfaces* **2018**, *10*, 5511; (f) P. Cui, D. Wei, J. Ji, H. Huang, E. Jia, S. Dou, T.
1556 Wang, W. Wang, M. Li, *Nat. Energy* **2019**, *4*, 150; (g) Z. Kang, H. Si, M. Shi, C. Xu,
1557 W. Fan, S. Ma, A. Kausar, Q. Liao, Z. Zhang, Y. Zhang, *Sci. China. Mater.* **2019**, *62*,
1558 776.
- 1559 [25] L. K. Ono, Y. B. Qi, *J. Phys. D. Appl. Phys.* **2018**, *51*, 093001.
- 1560 [26] H. C. Hsu, B. C. Huang, S. C. Chin, C. R. Hsing, D. L. Nguyen, M. Schnedler, R.
1561 Sankar, R. E. Dunin-Borkowski, C. M. Wei, C. W. Chen, P. Ebert, Y. P. Chiu, *ACS*
1562 *Nano* **2019**, *13*, 4402.
- 1563 [27] J. Hieulle, X. Wang, C. Stecker, D.-Y. Son, L. Qiu, R. Ohmann, L. K. Ono, A.
1564 Mugarza, Y. Yan, Y. B. Qi, *J. Am. Chem. Soc.* **2019**, *141*, 3515.
- 1565 [28] (a) L. D. Whalley, J. M. Frost, Y.-K. Jung, A. Walsh, *J. Chem. Phys.* **2017**, *146*,
1566 220901; (b) D. A. Egger, A. M. Rappe, L. Kronik, *Acc. Chem. Res.* **2016**, *49*, 573.
- 1567 [29] (a) X. Wu, L. Z. Tan, X. Shen, T. Hu, K. Miyata, M. T. Trinh, R. Li, R. Coffee, S. Liu,
1568 D. A. Egger, I. Makasyuk, Q. Zheng, A. Fry, J. S. Robinson, M. D. Smith, B.
1569 Guzelturk, H. I. Karunadasa, X. Wang, X. Zhu, L. Kronik, A. M. Rappe, A. M.
1570 Lindenberg, *Sci. Adv.* **2017**, *3*, e1602388; (b) A. N. Beecher, O. E. Semonin, J. M.
1571 Skelton, J. M. Frost, M. W. Terban, H. Zhai, A. Alatas, J. S. Owen, A. Walsh, S. J. L.
1572 Billinge, *ACS Energy Lett.* **2016**, *1*, 880; (c) J. Gong, M. Yang, X. Ma, R. D. Schaller,
1573 G. Liu, L. Kong, Y. Yang, M. C. Beard, M. Lesslie, Y. Dai, B. Huang, K. Zhu, T. Xu,
1574 *J. Phys. Chem. Lett.* **2016**, *7*, 2879; (d) J. M. Frost, A. Walsh, *Acc. Chem. Res.* **2016**,
1575 *49*, 528; (e) A. M. A. Leguy, J. M. Frost, A. P. McMahon, V. G. Sakai, W.
1576 Kockelmann, C. Law, X. Li, F. Foglia, A. Walsh, B. C. O'Regan, J. Nelson, J. T.
1577 Cabral, P. R. F. Barnes, *Nat. Commun.* **2015**, *6*, 7124.
- 1578 [30] D. A. Egger, A. Bera, D. Cahen, G. Hodes, T. Kirchartz, L. Kronik, R. Lovrincic, A.
1579 M. Rappe, D. R. Reichman, O. Yaffe, *Adv. Mater.* **2018**, *30*, 1800691.
- 1580 [31] J. M. Frost, K. T. Butler, F. Brivio, C. H. Hendon, M. van Schilfgaarde, A. Walsh,
1581 *Nano Lett.* **2014**, *14*, 2584.
- 1582 [32] A. Pecchia, D. Gentilini, D. Rossi, M. Auf der Maur, A. Di Carlo, *Nano Lett.* **2016**,
1583 *16*, 988.
- 1584 [33] H. Röhm, T. Leonhard, A. D. Schulz, S. Wagner, M. J. Hoffmann, A. Colmann, *Adv.*
1585 *Mater.* **2019**, *31*, 1806661.
- 1586 [34] S. G. P. Mahale, B. P. Kore, S. Mukherjee, M. S. Pavan, C. De, S. Ghara, A.
1587 Sundaresan, A. Pandey, T. N. Guru Row, D. D. Sarma, *J. Phys. Chem. Lett.* **2016**,
1588 *2412*.
- 1589 [35] (a) H. Röhm, T. Leonhard, M. J. Hoffmann, A. Colmann, *Energy Environ. Sci.* **2017**,
1590 *10*, 950; (b) P. Wang, J. Zhao, L. Wei, Q. Zhu, S. Xie, J. Liu, X. Meng, J. Li,
1591 *Nanoscale* **2017**, *9*, 3806; (c) Y. Kutes, L. Ye, Y. Zhou, S. Pang, B. D. Huey, N. P.

- 1592 Padture, *J. Phys. Chem. Lett.* **2014**, *5*, 3335; (d) B. Chen, X. Zheng, M. Yang, Y.
 1593 Zhou, S. Kundu, J. Shi, K. Zhu, S. Priya, *Nano Energy* **2015**, *13*, 582; (e) H.-S. Kim,
 1594 S. K. Kim, B. J. Kim, K.-S. Shin, M. K. Gupta, H. S. Jung, S.-W. Kim, N.-G. Park, *J.*
 1595 *Phys. Chem. Lett.* **2015**, *6*, 1729; (f) B. Chen, J. Shi, X. Zheng, Y. Zhou, K. Zhu, S.
 1596 Priya, *J. Mater. Chem. A* **2015**, *3*, 7699; (g) Y.-J. Kim, T.-V. Dang, H.-J. Choi, B.-J.
 1597 Park, J.-H. Eom, H.-A. Song, D. Seol, Y. Kim, S.-H. Shin, J. Nah, S.-G. Yoon, *J.*
 1598 *Mater. Chem. A* **2016**, *4*, 756; (h) I. M. Hermes, S. A. Bretschneider, V. W.
 1599 Bergmann, D. Li, A. Klasen, J. Mars, W. Tremel, F. Laquai, H.-J. Butt, M. Mezger, R.
 1600 Berger, B. J. Rodriguez, S. A. L. Weber, *J. Phys. Chem. C* **2016**, *120*, 5724.
 1601 [36] (a) E. Strelcov, Q. Dong, T. Li, J. Chae, Y. Shao, Y. Deng, A. Gruverman, J. Huang,
 1602 A. Centrone, *Sci. Adv.* **2017**, *3*, e1602165; (b) Z. Xiao, Y. Yuan, Y. Shao, Q. Wang, Q.
 1603 Dong, C. Bi, P. Sharma, A. Gruverman, J. Huang, *Nat Mater* **2015**, *14*, 193; (c) M.
 1604 Coll, A. Gomez, E. Mas-Marza, O. Almora, G. Garcia-Belmonte, M. Campoy-Quiles,
 1605 J. Bisquert, *J. Phys. Chem. Lett.* **2015**, *6*, 1408; (d) Z. Fan, J. Xiao, K. Sun, L. Chen,
 1606 Y. Hu, J. Ouyang, K. P. Ong, K. Zeng, J. Wang, *J. Phys. Chem. Lett.* **2015**, *6*, 1155.
 1607 [37] M. U. Rothmann, W. Li, Y. Zhu, U. Bach, L. Spiccia, J. Etheridge, Y.-B. Cheng, *Nat.*
 1608 *Commun.* **2017**, *8*, 14547.
 1609 [38] J. Hieulle, C. Stecker, R. Ohmann, L. K. Ono, Y. B. Qi, *Small Methods* **2018**, *2*,
 1610 1700295.
 1611 [39] T. W. Kim, S. Uchida, T. Matsushita, L. Cojocar, R. Jono, K. Kimura, D. Matsubara,
 1612 M. Shirai, K. Ito, H. Matsumoto, T. Kondo, H. Segawa, *Adv. Mater.* **2018**, *30*,
 1613 1705230.
 1614 [40] (a) E. T. Hoke, D. J. Slotcavage, E. R. Dohner, A. R. Bowring, H. I. Karunadasa, M.
 1615 D. McGehee, *Chem. Sci.* **2015**, *6*, 613; (b) D. J. Slotcavage, H. I. Karunadasa, M. D.
 1616 McGehee, *ACS Energy Lett.* **2016**, *1*, 1199; (c) E. L. Unger, L. Kegelmann, K.
 1617 Suchan, D. Sörell, L. Korte, S. Albrecht, *J. Mater. Chem. A* **2017**, *5*, 11401.
 1618 [41] C. G. Bischak, C. L. Hetherington, H. Wu, S. Aloni, D. F. Ogletree, D. T. Limmer, N.
 1619 S. Ginsberg, *Nano Lett.* **2017**, *17*, 1028.
 1620 [42] (a) R. Ohmann, L. K. Ono, H.-S. Kim, H. Lin, M. V. Lee, Y. Li, N.-G. Park, Y. B. Qi,
 1621 *J. Am. Chem. Soc.* **2015**, *137*, 16049; (b) L. She, M. Liu, D. Zhong, *ACS Nano* **2016**,
 1622 *10*, 1126; (c) L. She, M. Liu, X. Li, Z. Cai, D. Zhong, *Surf. Sci.* **2017**, *656*, 17; (d) L.
 1623 Cai, L. She, H. Qin, L. Xu, D. Zhong, *Surf. Sci.* **2018**, *675*, 78; (e) A. J. Yost, A.
 1624 Pimachev, C.-C. Ho, S. B. Darling, L. Wang, W.-F. Su, Y. Dahnovsky, T. Chien, *ACS*
 1625 *Appl. Mater. Interfaces* **2016**, *8*, 29110.
 1626 [43] (a) Q. Sun, P. Fassel, Y. Vaynzof, *ACS Appl. Energy Mater.* **2018**, *1*, 2410; (b) J.-P.
 1627 Correa-Baena, Y. Luo, T. M. Brenner, J. Snaider, S. Sun, X. Li, M. A. Jensen, N. T. P.
 1628 Hartono, L. Nienhaus, S. Wieghold, J. R. Poindexter, S. Wang, Y. S. Meng, T. Wang,
 1629 B. Lai, M. V. Holt, Z. Cai, M. G. Bawendi, L. Huang, T. Buonassisi, D. P. Fenning,
 1630 *Science* **2019**, *363*, 627; (c) S. Wieghold, J. Tresback, J.-P. Correa-Baena, N. T. P.
 1631 Hartono, S. Sun, Z. Liu, M. Layurova, Z. A. VanOrman, A. S. Bieber, J. Thapa, B.
 1632 Lai, Z. Cai, L. Nienhaus, T. Buonassisi, *Chem. Mater.* **2019**, *31*, 3712; (d) M.
 1633 Vrućinić, C. Matthiesen, A. Sadhanala, G. Divitini, S. Cacovich, S. E. Dutton, C.
 1634 Ducati, M. Atatüre, H. Snaith, R. H. Friend, H. Sirringhaus, F. Deschler, *Adv. Sci.*
 1635 **2015**, *2*, 1500136; (e) J. Chae, Q. Dong, J. Huang, A. Centrone, *Nano Lett.* **2015**, *15*,
 1636 8114; (f) H. R. Jung, B. P. Nguyen, H.-J. Jin, T. T. T. Nguyen, S. Yoon, W. S. Woo,
 1637 C. W. Ahn, S. Cho, I. W. Kim, W. Jo, *CrystEngComm* **2018**, *20*, 6551; (g) B. Philippe,
 1638 M. Saliba, J.-P. Correa-Baena, U. B. Cappel, S.-H. Turren-Cruz, M. Grätzel, A.
 1639 Hagfeldt, H. Rensmo, *Chem. Mater.* **2017**, *29*, 3589.
 1640 [44] L. K. Ono, E. J. Juárez-Pérez, Y. B. Qi, *ACS Appl. Mater. Interfaces* **2017**, *9*, 30197.
 1641 [45] (a) R. Brenes, D. Guo, A. Osherov, N. K. Noel, C. Eames, E. M. Hutter, S. K. Pathak,
 1642 F. Niroui, R. H. Friend, M. S. Islam, H. J. Snaith, V. Bulović, T. J. Savenije, S. D.

- 1643 Stranks, *Joule* **2017**, *1*, 155; (b) R. Brenes, C. Eames, V. Bulović, M. S. Islam, S. D.
 1644 Stranks, *Adv. Mater.* **2018**, *30*, 1706208.
- 1645 [46] G. Paul, S. Chatterjee, H. Bhunia, A. J. Pal, *J. Phys. Chem. C* **2018**, *122*, 20194.
- 1646 [47] (a) U. Dasgupta, A. Bera, A. J. Pal, *ACS Energy Lett.* **2017**, *2*, 582; (b) S. Chatterjee,
 1647 A. J. Pal, *J. Mater. Chem. A* **2018**, *6*, 3793.
- 1648 [48] (a) A. Kahn, *Mater. Horizons* **2016**, *3*, 7; (b) S. Wang, T. Sakurai, W. Wen, Y. B. Qi,
 1649 *Adv. Mater. Interfaces* **2018**, *5*, 1800260; (c) P. Schulz, D. Cahen, A. Kahn, *Chem.*
 1650 *Rev.* **2019**, *119*, 3349.
- 1651 [49] (a) P. Schulz, E. Edri, S. Kirmayer, G. Hodes, D. Cahen, A. Kahn, *Energy Environ.*
 1652 *Sci.* **2014**, *7*, 1377; (b) J. Endres, D. A. Egger, M. Kulbak, R. A. Kerner, L. Zhao, S.
 1653 H. Silver, G. Hodes, B. P. Rand, D. Cahen, L. Kronik, A. Kahn, *J. Phys. Chem. Lett.*
 1654 **2016**, *7*, 2722; (c) S. Tao, I. Schmidt, G. Brocks, J. Jiang, I. Tranca, K. Meerholz, S.
 1655 Olthof, *Nat. Commun.* **2019**, *10*, 2560; (d) D. Shin, D. Kang, J. Jeong, S. Park, M.
 1656 Kim, H. Lee, Y. Yi, *J. Phys. Chem. Lett.* **2017**, *8*, 5423; (e) P. Caprioglio, F. Zu, C. M.
 1657 Wolff, J. A. Márquez Prieto, M. Stolterfoht, P. Becker, N. Koch, T. Unold, B. Rech, S.
 1658 Albrecht, D. Neher, *Sustain. Energ. Fuels* **2019**, *3*, 550; (f) C. Wang, C. Wang, X. Liu,
 1659 J. Kauppi, Y. Shao, Z. Xiao, C. Bi, J. Huang, Y. Gao, *Appl. Phys. Lett.* **2015**, *106*,
 1660 111603; (g) C. Wang, X. Liu, C. Wang, Z. Xiao, C. Bi, Y. Shao, J. Huang, Y. Gao, *J.*
 1661 *Vac. Sci. Technol. B* **2015**, *33*, 032401; (h) J. Endres, M. Kulbak, L. Zhao, B. P. Rand,
 1662 D. Cahen, G. Hodes, A. Kahn, *J. Appl. Phys.* **2017**, *121*, 035304; (i) C. Wang, B. R.
 1663 Ecker, H. Wei, J. Huang, J.-Q. Meng, Y. Gao, *Phys. Chem. Chem. Phys.* **2017**, *19*,
 1664 5361; (j) M.-C. Jung, S. R. Raga, L. K. Ono, Y. B. Qi, *Sci. Rep.* **2015**, *5*, 9863; (k) Z.
 1665 Wu, Z. Liu, Z. Hu, Z. Hawash, L. Qiu, Y. Jiang, L. K. Ono, Y. B. Qi, *Adv. Mater.*
 1666 **2019**, *31*, 1804284; (l) Y. Jiang, M. R. Leyden, L. Qiu, S. Wang, L. K. Ono, Z. Wu, E.
 1667 J. Juarez-Perez, Y. B. Qi, *Adv. Funct. Mater.* **2018**, *28*, 1703835; (m) Z. Hawash, S. R.
 1668 Raga, D.-Y. Son, L. K. Ono, N.-G. Park, Y. B. Qi, *J. Phys. Chem. Lett.* **2017**, *8*, 3947;
 1669 (n) J. Liang, Z. Liu, L. Qiu, Z. Hawash, L. Meng, Z. Wu, Y. Jiang, L. K. Ono, Y. B.
 1670 Qi, *Adv. Energy Mater.* **2018**, *8*, 1800504; (o) D. Luo, W. Yang, Z. Wang, A.
 1671 Sadhanala, Q. Hu, R. Su, R. Shivanna, G. F. Trindade, J. F. Watts, Z. Xu, T. Liu, K.
 1672 Chen, F. Ye, P. Wu, L. Zhao, J. Wu, Y. Tu, Y. Zhang, X. Yang, W. Zhang, R. H.
 1673 Friend, Q. Gong, H. J. Snaith, R. Zhu, *Science* **2018**, *360*, 1442; (p) K. Yan, J. Chen,
 1674 H. Ju, F. Ding, H. Chen, C.-Z. Li, *J. Mater. Chem. A* **2018**, *6*, 15495; (q) C. Li, J. Wei,
 1675 M. Sato, H. Koike, Z.-Z. Xie, Y.-Q. Li, K. Kanai, S. Kera, N. Ueno, J.-X. Tang, *ACS*
 1676 *Appl. Mater. Interfaces* **2016**, *8*, 11526; (r) R. Comin, G. Walters, E. S. Thibau, O.
 1677 Voznyy, Z.-H. Lu, E. H. Sargent, *J. Mater. Chem. C* **2015**, *3*, 8839; (s) E. M. Miller,
 1678 Y. Zhao, C. C. Mercado, S. K. Saha, J. M. Luther, K. Zhu, V. Stevanović, C. L.
 1679 Perkins, J. van de Lagemaat, *Phys. Chem. Chem. Phys.* **2014**, *16*, 22122; (t) Q.-D. Ou,
 1680 C. Li, Q.-K. Wang, Y.-Q. Li, J.-X. Tang, *Adv. Mater. Interfaces* **2017**, *4*, 1600694.
- 1681 [50] (a) A. Miyata, A. Mitioglu, P. Plochocka, O. Portugall, J. T.-W. Wang, S. D. Stranks,
 1682 H. J. Snaith, R. J. Nicholas, *Nat. Phys.* **2015**, *11*, 582; (b) X. Chen, H. Lu, Y. Yang,
 1683 M. C. Beard, *J. Phys. Chem. Lett.* **2018**, *9*, 2595; (c) F. Ruf, M. F. Aygüler, N.
 1684 Giesbrecht, B. Rendenbach, A. Magin, P. Docampo, H. Kalt, M. Hetterich, *APL*
 1685 *Mater.* **2019**, *7*, 031113.
- 1686 [51] S. Prathapani, P. Bhargava, S. Mallick, *Appl. Phys. Lett.* **2018**, *112*, 092104.
- 1687 [52] F. Zu, P. Amsalem, D. A. Egger, R. Wang, C. M. Wolff, H. Fang, M. A. Loi, D.
 1688 Neher, L. Kronik, S. Duhm, N. Koch, *J. Phys. Chem. Lett.* **2019**, *10*, 601.
- 1689 [53] R. E. Brandt, V. Stevanović, D. S. Ginley, T. Buonassisi, *MRS Commun.* **2015**, *5*, 265.
- 1690 [54] M.-I. Lee, A. Barragán, M. N. Nair, V. L. R. Jacques, D. Le Bolloc'h, P. Fertey, K.
 1691 Jemli, F. Lédée, G. Trippé-Allard, E. Deleporte, A. Taleb-Ibrahimi, A. Tejada, *J.*
 1692 *Phys. D. Appl. Phys.* **2017**, *50*, 26LT02.

- 1693 [55] (a) F. Zu, P. Amsalem, M. Ralaïarisoa, T. Schultz, R. Schlesinger, N. Koch, *ACS*
1694 *Appl. Mater. Interfaces* **2017**, *9*, 41546; (b) F.-S. Zu, P. Amsalem, I. Salzmann, R.-B.
1695 Wang, M. Ralaïarisoa, S. Kowarik, S. Duhm, N. Koch, *Adv. Optical Mater.* **2017**, *5*,
1696 1700139.
- 1697 [56] D. Meggiolaro, E. Mosconi, F. De Angelis, *ACS Energy Lett.* **2019**, *4*, 779.
- 1698 [57] P. Schulz, L. L. Whittaker-Brooks, B. A. MacLeod, D. C. Olson, Y.-L. Loo, A. Kahn,
1699 *Adv. Mater. Interfaces* **2015**, *2*, 1400532.
- 1700 [58] (a) W.-J. Yin, T. Shi, Y. Yan, *Appl. Phys. Lett.* **2014**, *104*, 063903; (b) E. J. Juarez-
1701 Perez, Z. Hawash, S. R. Raga, L. K. Ono, Y. B. Qi, *Energy Environ. Sci.* **2016**, *9*,
1702 3406.
- 1703 [59] (a) Y. Zou, Q. Meng, H. Mao, D. Zhu, *Org. Electron.* **2017**, *41*, 307; (b) S. Olthof, K.
1704 Meerholz, *Sci. Rep.* **2017**, *7*, 40267; (c) K.-G. Lim, S. Ahn, Y.-H. Kim, Y. B. Qi, T.-
1705 W. Lee, *Energy Environ. Sci.* **2016**, *9*, 932; (d) X. Zhou, X. Li, Y. Liu, F. Huang, D.
1706 Zhong, *Appl. Phys. Lett.* **2016**, *108*, 121601.
- 1707 [60] S. Olthof, *APL Mater.* **2016**, *4*, 091502.
- 1708 [61] Q.-K. Wang, R.-B. Wang, P.-F. Shen, C. Li, Y.-Q. Li, L.-J. Liu, S. Duhm, J.-X. Tang,
1709 *Adv. Mater. Interfaces* **2015**, *2*, 1400528.
- 1710 [62] X. Liu, C. Wang, L. Lyu, C. Wang, Z. Xiao, C. Bi, J. Huang, Y. Gao, *Phys. Chem.*
1711 *Chem. Phys.* **2015**, *17*, 896.
- 1712 [63] (a) Y. Zhao, A. M. Nardes, K. Zhu, *Appl. Phys. Lett.* **2014**, *104*, 213906; (b) P. Liu, X.
1713 Liu, L. Lyu, H. Xie, H. Zhang, D. Niu, H. Huang, C. Bi, Z. Xiao, J. Huang, Y. Gao,
1714 *Appl. Phys. Lett.* **2015**, *106*, 193903.
- 1715 [64] S. Chen, T. W. Goh, D. Sabba, J. Chua, N. Mathews, C. H. A. Huan, T. C. Sum, *APL*
1716 *Mater.* **2014**, *2*, 081512.
- 1717 [65] G. Ji, B. Zhao, F. Song, G. Zheng, X. Zhang, K. Shen, Y. Yang, S. Chen, X. Gao,
1718 *Appl. Surf. Sci.* **2017**, *393*, 417.
- 1719 [66] M.-F. Lo, Z.-Q. Guan, T.-W. Ng, C.-Y. Chan, C.-S. Lee, *Adv. Funct. Mater.* **2015**, *25*,
1720 1213.
- 1721 [67] A. Zohar, M. Kulbak, I. Levine, G. Hodes, A. Kahn, D. Cahen, *ACS Energy Lett.*
1722 **2019**, *4*, 1.
- 1723 [68] H. Wang, A. Guerrero, A. Bou, A. M. Al-Mayouf, J. Bisquert, *Energy Environ. Sci.*
1724 **2019**, *12*, 2054.
- 1725 [69] M. Kulbak, I. Levine, E. Barak - Kulbak, S. Gupta, A. Zohar, I. Balberg, G. Hodes, D.
1726 Cahen, *Adv. Energy Mater.* **2018**, *8*, 1800398.
- 1727 [70] P. Fassel, V. Lami, A. Bausch, Z. Wang, M. T. Klug, H. J. Snaith, Y. Vaynzof, *Energy*
1728 *Environ. Sci.* **2018**, *11*, 3380.
- 1729 [71] (a) I. A. Howard, T. Abzieher, I. M. Hossain, H. Eggers, F. Schackmar, S. Ternes, B.
1730 S. Richards, U. Lemmer, U. W. Paetzold, *Adv. Mater.* **2019**, *31*, 1806702; (b) L. Qiu,
1731 L. K. Ono, Y. B. Qi, *Mater. Today Energy* **2018**, *7*, 169; (c) M. Remeika, Y. B. Qi, *J.*
1732 *Energy Chem.* **2018**, *27*, 1101; (d) L. K. Ono, M. R. Leyden, S. Wang, Y. B. Qi, *J.*
1733 *Mater. Chem. A* **2016**, *4*, 6693.
- 1734 [72] (a) R. Wang, M.-P. Zhuo, J. Li, T. Zhai, J. Yang, K. Fu, L.-S. Liao, L. Liu, S. Duhm,
1735 *Adv. Mater. Interfaces* **2019**, *6*, 1801827; (b) R. Wang, C. Wu, Y. Hu, J. Li, P. Shen,
1736 Q. Wang, L. Liao, L. Liu, S. Duhm, *ACS Appl. Mater. Interfaces* **2017**, *9*, 7859; (c) J.
1737 Emara, T. Schmier, N. Pourdavoud, T. Riedl, K. Meerholz, S. Olthof, *Adv. Mater.*
1738 **2016**, *28*, 553; (d) H. Xie, X. Liu, L. Lyu, D. Niu, Q. Wang, J. Huang, Y. Gao, *J.*
1739 *Phys. Chem. C* **2016**, *120*, 215; (e) T. G. Kim, S. W. Seo, H. Kwon, J. Hahn, J. W.
1740 Kim, *Phys. Chem. Chem. Phys.* **2015**, *17*, 24342.
- 1741 [73] S. Singh, D. Kabra, *J. Mater. Chem. C* **2018**, *6*, 12052.
- 1742 [74] Q. Wang, Y. Shao, H. Xie, L. Lyu, X. Liu, Y. Gao, J. Huang, *Appl. Phys. Lett.* **2014**,
1743 *105*, 163508.

- 1744 [75] (a) S. R. Raga, M.-C. Jung, M. V. Lee, M. R. Leyden, Y. Kato, Y. B. Qi, *Chem.*
 1745 *Mater.* **2015**, *27*, 1597; (b) B. Conings, J. Drijkoningen, N. Gauquelin, A. Babayigit, J.
 1746 D'Haen, L. D'Olieslaeger, A. Ethirajan, J. Verbeeck, J. Manca, E. Mosconi, F. D.
 1747 Angelis, H.-G. Boyen, *Adv. Energy Mater.* **2015**, *5*, 1500477; (c) B. Conings, L.
 1748 Baeten, C. De Dobbelaere, J. D'Haen, J. Manca, H.-G. Boyen, *Advanced Materials*
 1749 **2014**, *26*, 2041.
- 1750 [76] (a) W.-J. Yin, T. Shi, Y. Yan, *Adv. Mater.* **2014**, *26*, 4653; (b) W.-J. Yin, H. Chen, T.
 1751 Shi, S.-H. Wei, Y. Yan, *Adv. Electron. Mater.* **2015**, *1*, 1500044.
- 1752 [77] (a) L. Liu, J. A. McLeod, R. Wang, P. Shen, S. Duhm, *Appl. Phys. Lett.* **2015**, *107*,
 1753 061904; (b) W. Xu, L. Liu, L. Yang, P. Shen, B. Sun, J. A. McLeod, *Nano Lett.* **2016**,
 1754 *16*, 4720.
- 1755 [78] (a) M.-C. Jung, Y. M. Lee, H.-K. Lee, J. Park, S. R. Raga, L. K. Ono, S. Wang, M. R.
 1756 Leyden, B. D. Yu, S. Hong, Y. B. Qi, *Appl. Phys. Lett.* **2016**, *108*, 073901; (b) I.
 1757 Maeng, Y. M. Lee, J. Park, S. R. Raga, C. Kang, C.-S. Kee, B. D. Yu, S. Hong, L. K.
 1758 Ono, Y. B. Qi, M.-C. Jung, M. Nakamura, *Sci. Rep.* **2019**, *9*, 5811.
- 1759 [79] (a) E. J. Juarez-Perez, L. K. Ono, M. Maeda, Y. Jiang, Z. Hawash, Y. B. Qi, *J. Mater.*
 1760 *Chem. A* **2018**, *6*, 9604; (b) E. J. Juarez-Perez, L. K. Ono, I. Uriarte, E. J. Cocinero, Y.
 1761 B. Qi, *ACS Appl. Mater. Interfaces* **2019**, *11*, 12586.
- 1762 [80] P. Willmott, *John Wiley & Sons, Ltd* **2011**, DOI:10.1002/9781119970958.
- 1763 [81] M. Stolterfoht, P. Caprioglio, C. M. Wolff, J. A. Márquez, J. Nordmann, S. Zhang, D.
 1764 Rothhardt, U. Hörmann, Y. Amir, A. Redinger, L. Kegelmann, F. Zu, S. Albrecht, N.
 1765 Koch, T. Kirchartz, M. Saliba, T. Unold, D. Neher, *Energy Environ. Sci.* **2019**.
- 1766 [82] (a) Q. Jiang, X. Zhang, J. You, *Small* **2018**, *14*, 1801154; (b) J. Urieta-Mora, I. García-
 1767 Benito, A. Molina-Ontoria, N. Martín, *Chem. Soc. Rev.* **2018**, *47*, 8541; (c) P.-K.
 1768 Kung, M.-H. Li, P.-Y. Lin, Y.-H. Chiang, C.-R. Chan, T.-F. Guo, P. Chen, *Adv.*
 1769 *Mater. Interfaces* **2018**, *5*, 1800882.
- 1770 [83] E. H. Jung, N. J. Jeon, E. Y. Park, C. S. Moon, T. J. Shin, T.-Y. Yang, J. H. Noh, J.
 1771 Seo, *Nature* **2019**, *567*, 511.
- 1772 [84] (a) L. Qiu, Z. Liu, L. K. Ono, Y. Jiang, D.-Y. Son, Z. Hawash, S. He, Y. B. Qi, *Adv.*
 1773 *Funct. Mater.* **2018**, DOI: 10.1002/adfm.201806779; (b) L. Qiu, S. He, Y. Jiang, D.-
 1774 Y. Son, L. K. Ono, Z. Liu, T. Kim, T. Bouloumis, S. Kazaoui, Y. B. Qi, *J. Mater.*
 1775 *Chem. A* **2019**, *7*, 6920; (c) L. Qiu, L. K. Ono, Y. Jiang, M. R. Leyden, S. R. Raga, S.
 1776 Wang, Y. B. Qi, *J. Phys. Chem. B* **2018**, *122*, 511; (d) Q. Jiang, Y. Zhao, X. Zhang, X.
 1777 Yang, Y. Chen, Z. Chu, Q. Ye, X. Li, Z. Yin, J. You, *Nat. Photonics* **2019**, *13*, 460.
- 1778 [85] C. Chen, Z. Song, C. Xiao, D. Zhao, N. Shrestha, C. Li, G. Yang, F. Yao, X. Zheng,
 1779 R. J. Ellingson, C.-S. Jiang, M. Al-Jassim, K. Zhu, G. Fang, Y. Yan, *Nano Energy*
 1780 **2019**, *61*, 141.
- 1781 [86] J. J. Yoo, S. Wieghold, M. Sponseller, M. Chua, S. N. Bertram, N. T. P. Hartono, J.
 1782 Tresback, E. Hansen, J.-P. Correa-Baena, V. Bulovic, T. Buonassisi, S. S. Shin, M. G.
 1783 Bawendi, *Energy Environ. Sci.* **2019**.
- 1784 [87] (a) J. M. Azpiroz, E. Mosconi, J. Bisquert, F. De Angelis, *Energy Environ. Sci.* **2015**,
 1785 *8*, 2118; (b) A. J. Barker, A. Sadhanala, F. Deschler, M. Gandini, S. P. Senanayak, P.
 1786 M. Pearce, E. Mosconi, A. J. Pearson, Y. Wu, A. R. Srimath Kandada, T. Leijtens, F.
 1787 De Angelis, S. E. Dutton, A. Petrozza, R. H. Friend, *ACS Energy Lett.* **2017**, *2*, 1416;
 1788 (c) Y. Yuan, J. Huang, *Acc. Chem. Res.* **2016**, *49*, 286; (d) A. Alkauskas, M. D.
 1789 McCluskey, C. G. V. d. Walle, *J. Appl. Phys.* **2016**, *119*, 181101.
- 1790 [88] J.-S. Park, A. Walsh, *Nat. Energy* **2019**, *4*, 95.
- 1791 [89] S. G. Motti, D. Meggiolaro, A. J. Barker, E. Mosconi, C. A. R. Perini, J. M. Ball, M.
 1792 Gandini, M. Kim, F. De Angelis, A. Petrozza, *Nat. Photonics* **2019**, *13*, 532.
- 1793 [90] (a) S. Mahajan, *Acta Mater.* **2000**, *48*, 137; (b) J. S. Park, S. Kim, Z. Xie, A. Walsh,
 1794 *Nat. Rev. Mater.* **2018**, *3*, 194; (c) J. M. Ball, A. Petrozza, *Nat. Energy* **2016**, *1*, 16149;

- 1795 (d) T. M. Brenner, D. A. Egger, L. Kronik, G. Hodes, D. Cahen, *Nat. Rev. Mater.*
 1796 **2016**, *1*, 15007; (e) J. L. Garrett, E. M. Tennyson, M. Hu, J. Huang, J. N. Munday, M.
 1797 S. Leite, *Nano Lett.* **2017**, *17*, 2554; (f) S. Yun, X. Zhou, J. Even, A. Hagfeldt, *Angew.*
 1798 *Chem. Int. Ed.* **2017**, *56*, 15806; (g) C. Ran, J. Xu, W. Gao, C. Huang, S. Dou, *Chem.*
 1799 *Soc. Rev.* **2018**, *47*, 4581; (h) C.-J. Yu, *Journal of Physics: Energy* **2019**, *1*, 022001;
 1800 (i) D. Meggiolaro, F. De Angelis, *ACS Energy Lett.* **2018**, *3*, 2206; (j) L. K. Ono, S.
 1801 Liu, Y. B. Qi, *Angew. Chem. Int. Ed.* **2019**, DOI: 10.1002/ange.201905521.
- 1802 [91] J. Peng, Y. Chen, K. Zheng, T. Pullerits, Z. Liang, *Chem. Soc. Rev.* **2017**, *46*, 5714.
 1803 [92] J. Kim, S.-H. Lee, J. H. Lee, K.-H. Hong, *J. Phys. Chem. Lett.* **2014**, *5*, 1312.
 1804 [93] Q. A. Akkerman, G. Rainò, M. V. Kovalenko, L. Manna, *Nat. Mater.* **2018**, *17*, 394.
 1805 [94] M. H. Du, *J. Mater. Chem. A* **2014**, *2*, 9091.
 1806 [95] M. L. Agiorgousis, Y.-Y. Sun, H. Zeng, S. Zhang, *J. Am. Chem. Soc.* **2014**, *136*,
 1807 14570.
- 1808 [96] (a) W. S. Yang, B.-W. Park, E. H. Jung, N. J. Jeon, Y. C. Kim, D. U. Lee, S. S. Shin,
 1809 J. Seo, E. K. Kim, J. H. Noh, S. I. Seok, *Science* **2017**, *356*, 1376; (b) S. Wang, Y.
 1810 Jiang, Emilio J. Juarez-Perez, L. K. Ono, Y. B. Qi, *Nat. Energy* **2016**, *2*, 16195; (c) R.
 1811 G. Wilks, M. Bär, *Nat. Energy* **2017**, *2*, 16204.
- 1812 [97] M.-H. Du, *J. Phys. Chem. Lett.* **2015**, *6*, 1461.
 1813 [98] P. Xu, S. Chen, H.-J. Xiang, X.-G. Gong, S.-H. Wei, *Chem. Mater.* **2014**, *26*, 6068.
 1814 [99] W. Ming, H. Shi, M.-H. Du, *J. Mater. Chem. A* **2016**, *4*, 13852.
 1815 [100] J. Xu, J.-B. Liu, B.-X. Liu, B. Huang, *J. Phys. Chem. Lett.* **2017**, *8*, 4391.
 1816 [101] Z. Xiao, W. Meng, J. Wang, Y. Yan, *ChemSusChem* **2016**, *9*, 2628.
 1817 [102] (a) J. Haruyama, K. Sodeyama, L. Han, Y. Tateyama, *J. Phys. Chem. Lett.* **2014**, *5*,
 1818 2903; (b) J. Haruyama, K. Sodeyama, L. Han, Y. Tateyama, *Acc. Chem. Res.* **2016**,
 1819 *49*, 554; (c) H. Uratani, K. Yamashita, *J. Phys. Chem. Lett.* **2017**, *8*, 742; (d) E.
 1820 Mosconi, J. M. Azpiroz, F. De Angelis, *Chem. Mater.* **2015**, *27*, 4885; (e) C. Quarti, F.
 1821 De Angelis, D. Beljonne, *Chem. Mater.* **2017**, *29*, 958; (f) J. Yin, D. Cortecchia, A.
 1822 Krishna, S. Chen, N. Mathews, A. C. Grimsdale, C. Soci, *J. Phys. Chem. Lett.* **2015**, *6*,
 1823 1396; (g) W. Geng, C.-J. Tong, Z.-K. Tang, C. Yam, Y.-N. Zhang, W.-M. Lau, L.-M.
 1824 Liu, *Journal of Materiomics* **2015**, *1*, 213; (h) L. Zhang, X. Liu, J. Li, S. McKechnie,
 1825 *Sol. Energy Mater. Sol. Cells* **2018**, *175*, 1; (i) Y. Ouyang, Y. Li, P. Zhu, Q. Li, Y.
 1826 Gao, J. Tong, L. Shi, Q. Zhou, C. Ling, Q. Chen, Z. Deng, H. Tan, W. Deng, J. Wang,
 1827 *J. Mater. Chem. A* **2019**, *7*, 2275; (j) A. Torres, L. G. C. Rego, *J. Phys. Chem. C* **2014**,
 1828 *118*, 26947; (k) Y. Wang, B. G. Sumpter, J. Huang, H. Zhang, P. Liu, H. Yang, H.
 1829 Zhao, *J. Phys. Chem. C* **2015**, *119*, 1136.
- 1830 [103] (a) Y. Liu, K. Palotas, X. Yuan, T. Hou, H. Lin, Y. Li, S.-T. Lee, *ACS Nano* **2017**, *11*,
 1831 2060; (b) X. Huang, T. R. Paudel, P. A. Dowben, S. Dong, E. Y. Tsymbal, *Physical*
 1832 *Review B* **2016**, *94*, 195309.
- 1833 [104] B. Akbali, G. Topcu, T. Guner, M. Ozcan, M. M. Demir, H. Sahin, *Phys. Rev. Mater.*
 1834 **2018**, *2*, 034601.
- 1835 [105] (a) R. Lindblad, D. Bi, B.-w. Park, J. Oscarsson, M. Gorgoi, H. Siegbahn, M. Odelius,
 1836 E. M. J. Johansson, H. Rensmo, *J. Phys. Chem. Lett.* **2014**, *5*, 648; (b) S. D. Stranks,
 1837 *ACS Energy Lett.* **2017**, *2*, 1515.
- 1838 [106] D. Meggiolaro, S. G. Motti, E. Mosconi, A. J. Barker, J. Ball, C. Andrea Riccardo
 1839 Perini, F. Deschler, A. Petrozza, F. De Angelis, *Energy Environ. Sci.* **2018**, *11*, 702.
- 1840 [107] (a) J. Shi, X. Xu, D. Li, Q. Meng, *Small* **2015**, *11*, 2472; (b) A. Fakharuddin, L.
 1841 Schmidt-Mende, G. Garcia-Belmonte, R. Jose, I. Mora-Sero, *Adv. Energy Mater.*
 1842 **2017**, *7*, 1700623.
- 1843 [108] (a) E. Mosconi, E. Ronca, F. De Angelis, *J. Phys. Chem. Lett.* **2014**, *5*, 2619; (b) S.
 1844 Colella, E. Mosconi, G. Pellegrino, A. Alberti, V. L. P. Guerra, S. Masi, A. Listorti, A.
 1845 Rizzo, G. G. Condorelli, F. De Angelis, G. Gigli, *J. Phys. Chem. Lett.* **2014**, *5*, 3532;

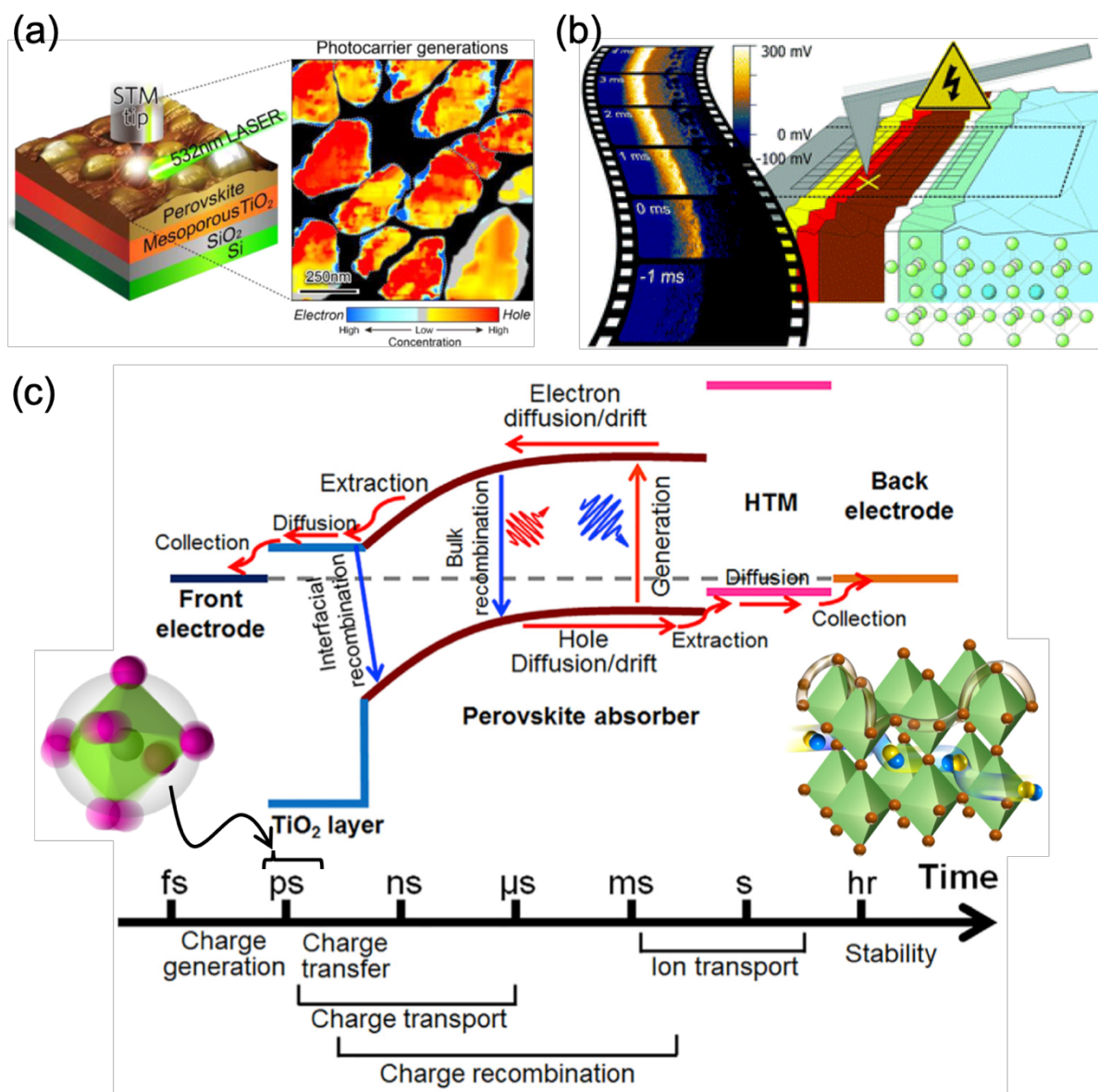
- 1846 (c) E. Mosconi, G. Grancini, C. Roldán-Carmona, P. Gratia, I. Zimmermann, M. K.
 1847 Nazeeruddin, F. De Angelis, *Chem. Mater.* **2016**, *28*, 3612; (d) V. Roiati, E. Mosconi,
 1848 A. Listorti, S. Colella, G. Gigli, F. De Angelis, *Nano Lett.* **2014**, *14*, 2168; (e) F. De
 1849 Angelis, *Acc. Chem. Res.* **2014**, *47*, 3349; (f) A. Akbari, J. Hashemi, E. Mosconi, F.
 1850 De Angelis, M. Hakala, *J. Mater. Chem. A* **2017**, *5*, 2339; (g) R. Long, W.-H. Fang, O.
 1851 V. Prezhdo, *J. Phys. Chem. C* **2017**, *121*, 3797; (h) J. Haruyama, K. Sodeyama, L.
 1852 Han, Y. Tateyama, *J. Am. Chem. Soc.* **2015**, *137*, 10048; (i) W. Geng, C.-J. Tong, J.
 1853 Liu, W. Zhu, W.-M. Lau, L.-M. Liu, *Sci. Rep.* **2016**, *6*, 20131; (j) L.-y. Wei, W. Ma,
 1854 C. Lian, S. Meng, *J. Phys. Chem. C* **2017**, *121*, 5905; (k) R. Long, O. V. Prezhdo, *ACS*
 1855 *Nano* **2015**, *9*, 11143; (l) H. Tan, A. Jain, O. Voznyy, X. Lan, F. P. García de Arquer,
 1856 J. Z. Fan, R. Quintero-Bermudez, M. Yuan, B. Zhang, Y. Zhao, F. Fan, P. Li, L. N.
 1857 Quan, Y. Zhao, Z.-H. Lu, Z. Yang, S. Hoogland, E. H. Sargent, *Science* **2017**, *355*,
 1858 722.
- 1859 [109] H.-J. Feng, T. R. Paudel, E. Y. Tsymbal, X. C. Zeng, *J. Am. Chem. Soc.* **2015**, *137*,
 1860 8227.
- 1861 [110] J. Yang, B. D. Siempelkamp, E. Mosconi, F. De Angelis, T. L. Kelly, *Chem. Mater.*
 1862 **2015**, *27*, 4229.
- 1863 [111] H.-J. Feng, J. Huang, X. C. Zeng, *Adv. Mater. Interfaces* **2016**, *3*, 1600267.
- 1864 [112] C.-X. Qian, Z.-Y. Deng, K. Yang, J. Feng, M.-Z. Wang, Z. Yang, S. Liu, H.-J. Feng,
 1865 *Appl. Phys. Lett.* **2018**, *112*, 093901.
- 1866 [113] E. Edri, S. Kirmayer, A. Henning, S. Mukhopadhyay, K. Gartsman, Y. Rosenwaks, G.
 1867 Hodes, D. Cahen, *Nano Lett.* **2014**, *14*, 1000.
- 1868 [114] L. Liu, S. Huang, Y. Lu, P. Liu, Y. Zhao, C. Shi, S. Zhang, J. Wu, H. Zhong, M. Sui,
 1869 H. Zhou, H. Jin, Y. Li, Q. Chen, *Adv. Mater.* **2018**, *30*, 1800544.
- 1870 [115] Y. Zhao, Q. Li, W. Zhou, Y. Hou, Y. Zhao, R. Fu, D. Yu, X. Liu, Q. Zhao, *Solar RRL*
 1871 **2019**, *3*, 1800296.
- 1872 [116] Y. Yan, W.-J. Yin, Y. Wu, T. Shi, N. R. Paudel, C. Li, J. Poplawsky, Z. Wang, J.
 1873 Moseley, H. Guthrey, H. Moutinho, S. J. Pennycook, M. M. Al-Jassim, *J. Appl. Phys.*
 1874 **2015**, *117*, 112807.
- 1875 [117] (a) A. P. Sutton, R. W. Balluff, *Interfaces in crystalline materials*. Clarendon Oxford,
 1876 Oxford: 1995; (b) P. Lejcek, *Grain Boundary Segregation in Metals*. Springer-Verlag
 1877 Berlin Heidelberg, Berlin: 2010; (c) H. Ogawa, *Mater. Trans.* **2006**, *47*, 2706; (d) M.
 1878 D. Sangid, H. Sehitoglu, H. J. Maier, T. Niendorf, *Materials Science and Engineering:*
 1879 *A* **2010**, *527*, 7115.
- 1880 [118] F. Zhu, L. Men, Y. Guo, Q. Zhu, U. Bhattacharjee, P. M. Goodwin, J. W. Petrich, E.
 1881 A. Smith, J. Vela, *ACS Nano* **2015**, *9*, 2948.
- 1882 [119] (a) W.-J. Yin, T. Shi, Y. Yan, *J. Phys. Chem. C* **2015**, *119*, 5253; (b) M. Imaeda, T.
 1883 Mizoguchi, Y. Sato, H. S. Lee, S. D. Findlay, N. Shibata, T. Yamamoto, Y. Ikuhara,
 1884 *Physical Review B* **2008**, *78*, 245320.
- 1885 [120] (a) Y. Yu, D. Zhang, C. Kisielowski, L. Dou, N. Kornienko, Y. Bekenstein, A. B.
 1886 Wong, A. P. Alivisatos, P. Yang, *Nano Lett.* **2016**, *16*, 7530; (b) Y. Yu, D. Zhang, P.
 1887 Yang, *Nano Lett.* **2017**, *17*, 5489.
- 1888 [121] Y. Guo, Q. Wang, W. A. Saidi, *J. Phys. Chem. C* **2017**, *121*, 1715.
- 1889 [122] J. Xu, J.-B. Liu, B.-X. Liu, J. Wang, B. Huang, *Adv. Funct. Mater.* **2019**, *29*, 1805870.
- 1890 [123] W.-J. Yin, Y. Wu, S.-H. Wei, R. Noufi, M. M. Al-Jassim, Y. Yan, *Adv. Energy Mater.*
 1891 **2014**, *4*, 1300712.
- 1892 [124] (a) B. S. Tosun, H. W. Hillhouse, *J. Phys. Chem. Lett.* **2015**, *6*, 2503; (b) B. R.
 1893 Sutherland, *Joule* **2018**, *2*, 820; (c) S. Sidhik, A. C. Pasarán, C. Rosiles Pérez, T.
 1894 López-Luke, E. De la Rosa, *J. Mater. Chem. C* **2018**, *6*, 7880.
- 1895 [125] R. Long, J. Liu, O. V. Prezhdo, *J. Am. Chem. Soc.* **2016**, *138*, 3884.

- 1896 [126] (a) D.-Y. Son, S.-G. Kim, J.-Y. Seo, S.-H. Lee, H. Shin, D. Lee, N.-G. Park, *J. Am.*
 1897 *Chem. Soc.* **2018**, *140*, 1358; (b) X. Gong, L. Guan, H. Pan, Q. Sun, X. Zhao, H. Li,
 1898 H. Pan, Y. Shen, Y. Shao, L. Sun, Z. Cui, L. Ding, M. Wang, *Adv. Funct. Mater.*
 1899 **2018**, *28*, 1804286; (c) J. T.-W. Wang, Z. Wang, S. Pathak, W. Zhang, D. W.
 1900 deQuillettes, F. Wisnivesky-Rocca-Rivarola, J. Huang, P. K. Nayak, J. B. Patel, H. A.
 1901 Mohd Yusof, Y. Vaynzof, R. Zhu, I. Ramirez, J. Zhang, C. Ducati, C. Grovenor, M.
 1902 B. Johnston, D. S. Ginger, R. J. Nicholas, H. J. Snaith, *Energy & Environmental*
 1903 *Science* **2016**, *9*, 2892; (d) T. Wu, Y. Wang, X. Li, Y. Wu, X. Meng, D. Cui, X. Yang,
 1904 L. Han, *Adv. Energy Mater.* **2019**, *9*, 1803766.
- 1905 [127] H. Tan, F. Che, M. Wei, Y. Zhao, M. I. Saidaminov, P. Todorović, D. Broberg, G.
 1906 Walters, F. Tan, T. Zhuang, B. Sun, Z. Liang, H. Yuan, E. Fron, J. Kim, Z. Yang, O.
 1907 Voznyy, M. Asta, E. H. Sargent, *Nat. Commun.* **2018**, *9*, 3100.
- 1908 [128] C. Liu, Z. Huang, X. Hu, X. Meng, L. Huang, J. Xiong, L. Tan, Y. Chen, *ACS Appl.*
 1909 *Mater. Interfaces* **2018**, *10*, 1909.
- 1910 [129] E. Mosconi, D. Meggiolaro, H. J. Snaith, S. D. Stranks, F. De Angelis, *Energy*
 1911 *Environ. Sci.* **2016**, *9*, 3180.
- 1912 [130] H. Tsai, R. Asadpour, J.-C. Blancon, C. C. Stoumpos, O. Durand, J. W. Strzalka, B.
 1913 Chen, R. Verduzco, P. M. Ajayan, S. Tretiak, J. Even, M. A. Alam, M. G. Kanatzidis,
 1914 W. Nie, A. D. Mohite, *Science* **2018**, *360*, 67.
- 1915 [131] W. Nie, J.-C. Blancon, A. J. Neukirch, K. Appavoo, H. Tsai, M. Chhowalla, M. A.
 1916 Alam, M. Y. Sfeir, C. Katan, J. Even, S. Tretiak, J. J. Crochet, G. Gupta, A. D.
 1917 Mohite, *Nat. Commun.* **2016**, *7*, 11574.
- 1918 [132] Q. Wang, B. Chen, Y. Liu, Y. Deng, Y. Bai, Q. Dong, J. Huang, *Energy Environ. Sci.*
 1919 **2017**, *10*, 516.
- 1920 [133] Y. Shao, Z. Xiao, C. Bi, Y. Yuan, J. Huang, *Nat. Commun.* **2014**, *5*, 5784.
- 1921 [134] F. Cai, L. Yang, Y. Yan, J. Zhang, F. Qin, D. Liu, Y.-B. Cheng, Y. Zhou, T. Wang, *J.*
 1922 *Mater. Chem. A* **2017**, *5*, 9402.
- 1923 [135] Y. Lin, L. Shen, J. Dai, Y. Deng, Y. Wu, Y. Bai, X. Zheng, J. Wang, Y. Fang, H. Wei,
 1924 W. Ma, X. C. Zeng, X. Zhan, J. Huang, *Adv. Mater.* **2017**, *29*, 1604545.
- 1925 [136] X. Zheng, B. Chen, J. Dai, Y. Fang, Y. Bai, Y. Lin, H. Wei, X. C. Zeng, J. Huang,
 1926 *Nature Energy* **2017**, *2*, 17102.
- 1927 [137] W. Li, W. Zhang, S. Van Reenen, R. J. Sutton, J. Fan, A. A. Haghighirad, M. B.
 1928 Johnston, L. Wang, H. J. Snaith, *Energy Environ. Sci.* **2016**, *9*, 490.
- 1929 [138] W. Ke, G. Fang, Q. Liu, L. Xiong, P. Qin, H. Tao, J. Wang, H. Lei, B. Li, J. Wan, G.
 1930 Yang, Y. Yan, *J. Am. Chem. Soc.* **2015**, *137*, 6730.
- 1931 [139] J. P. Correa Baena, L. Steier, W. Tress, M. Saliba, S. Neutzner, T. Matsui, F.
 1932 Giordano, T. J. Jacobsson, A. R. Srimath Kandada, S. M. Zakeeruddin, A. Petrozza,
 1933 A. Abate, M. K. Nazeeruddin, M. Grätzel, A. Hagfeldt, *Energy Environ. Sci.* **2015**, *8*,
 1934 2928.
- 1935 [140] E. H. Anaraki, A. Kermanpur, L. Steier, K. Domanski, T. Matsui, W. Tress, M. Saliba,
 1936 A. Abate, M. Grätzel, A. Hagfeldt, J.-P. Correa-Baena, *Energy Environ. Sci.* **2016**, *9*,
 1937 3128.
- 1938 [141] D. Yang, R. Yang, K. Wang, C. Wu, X. Zhu, J. Feng, X. Ren, G. Fang, S. Priya, S.
 1939 Liu, *Nat. Commun.* **2018**, *9*, 3239.
- 1940 [142] W. Ke, D. Zhao, C. Xiao, C. Wang, A. J. Cimaroli, C. R. Grice, M. Yang, Z. Li, C.-S.
 1941 Jiang, M. Al-Jassim, K. Zhu, M. G. Kanatzidis, G. Fang, Y. Yan, *J. Mater. Chem. A*
 1942 **2016**, *4*, 14276.
- 1943 [143] K. Liu, S. Chen, J. Wu, H. Zhang, M. Qin, X. Lu, Y. Tu, Q. Meng, X. Zhan, *Energy*
 1944 *Environ. Sci.* **2018**, *11*, 3463.
- 1945 [144] Z. Liu, K. Deng, J. Hu, L. Li, *Angew. Chem. Int. Ed.* **2019**, *58*, 11497.

- 1946 [145] Y. Zhao, W. Zhou, W. Ma, S. Meng, H. Li, J. Wei, R. Fu, K. Liu, D. Yu, Q. Zhao,
1947 *ACS Energy Lett.* **2016**, *1*, 266.
- 1948 [146] F. Wang, A. Shimazaki, F. Yang, K. Kanahashi, K. Matsuki, Y. Miyauchi, T.
1949 Takenobu, A. Wakamiya, Y. Murata, K. Matsuda, *J. Phys. Chem. C* **2017**, *121*, 1562.
- 1950 [147] G. Han, T. M. Koh, S. S. Lim, T. W. Goh, X. Guo, S. W. Leow, R. Begum, T. C.
1951 Sum, N. Mathews, S. Mhaisalkar, *ACS Appl. Mater. Interfaces* **2017**, *9*, 21292.
- 1952 [148] D. Koushik, W. J. H. Verhees, Y. Kuang, S. Veenstra, D. Zhang, M. A. Verheijen, M.
1953 Creatore, R. E. I. Schropp, *Energy Environ. Sci.* **2017**, *10*, 91.
- 1954 [149] (a) P. Chen, Y. Bai, S. Wang, M. Lyu, J.-H. Yun, L. Wang, *Adv. Funct. Mater.* **2018**,
1955 *28*, 1706923; (b) K. T. Cho, G. Grancini, Y. Lee, E. Oveisi, J. Ryu, O. Almora, M.
1956 Tschumi, P. A. Schouwink, G. Seo, S. Heo, J. Park, J. Jang, S. Paek, G. Garcia-
1957 Belmonte, M. K. Nazeeruddin, *Energy Environ. Sci.* **2018**, *11*, 952.
- 1958 [150] Y. Lin, Y. Bai, Y. Fang, Z. Chen, S. Yang, X. Zheng, S. Tang, Y. Liu, J. Zhao, J.
1959 Huang, *J. Phys. Chem. Lett.* **2018**, *9*, 654.
- 1960 [151] S. Gharibzadeh, B. Abdollahi Nejand, M. Jakoby, T. Abzieher, D. Hauschild, S.
1961 Moghadamzadeh, J. A. Schwenzen, P. Brenner, R. Schmager, A. A. Haghighirad, L.
1962 Weinhardt, U. Lemmer, B. S. Richards, I. A. Howard, U. W. Paetzold, *Adv. Energy*
1963 *Mater.* **2019**, *9*, 1803699.
- 1964 [152] J. Peng, J. I. Khan, W. Liu, E. Ugur, T. Duong, Y. Wu, H. Shen, K. Wang, H. Dang,
1965 E. Aydin, X. Yang, Y. Wan, K. J. Weber, K. R. Catchpole, F. Laquai, S. De Wolf, T.
1966 P. White, *Adv. Energy Mater.* **2018**, *8*, 1801208.
- 1967 [153] A. Dualeh, N. Tétreault, T. Moehl, P. Gao, M. K. Nazeeruddin, M. Grätzel, *Adv.*
1968 *Funct. Mater.* **2014**, *24*, 3250.
- 1969 [154] Z. Xiao, Q. Dong, C. Bi, Y. Shao, Y. Yuan, J. Huang, *Adv. Mater.* **2014**, *26*, 6503.
- 1970 [155] J. Liu, C. Gao, X. He, Q. Ye, L. Ouyang, D. Zhuang, C. Liao, J. Mei, W. Lau, *ACS*
1971 *Appl. Mater. Interfaces* **2015**, *7*, 24008.
- 1972 [156] W. Nie, H. Tsai, R. Asadpour, J.-C. Blancon, A. J. Neukirch, G. Gupta, J. J. Crochet,
1973 M. Chhowalla, S. Tretiak, M. A. Alam, H.-L. Wang, A. D. Mohite, *Science* **2015**, *347*,
1974 522.
- 1975 [157] S. M. Jain, Z. Qiu, L. Häggman, M. Mirmohades, M. B. Johansson, T. Edvinsson, G.
1976 Boschloo, *Energy Environ. Sci.* **2016**, *9*, 3770.
- 1977 [158] Q. Wang, Y. Shao, Q. Dong, Z. Xiao, Y. Yuan, J. Huang, *Energy Environ. Sci.* **2014**,
1978 *7*, 2359.
- 1979 [159] (a) W. Zhang, S. Pathak, N. Sakai, T. Stergiopoulos, P. K. Nayak, N. K. Noel, A. A.
1980 Haghighirad, V. M. Burlakov, D. W. deQuilettes, A. Sadhanala, W. Li, L. Wang, D. S.
1981 Ginger, R. H. Friend, H. J. Snaith, *Nat. Commun.* **2015**, *6*, 10030; (b) H. Jiang, Z.
1982 Yan, H. Zhao, S. Yuan, Z. Yang, J. Li, B. Liu, T. Niu, J. Feng, Q. Wang, D. Wang, H.
1983 Yang, Z. Liu, S. F. Liu, *ACS Appl. Energy Mater.* **2018**, *1*, 900.
- 1984 [160] N. De Marco, H. Zhou, Q. Chen, P. Sun, Z. Liu, L. Meng, E.-P. Yao, Y. Liu, A.
1985 Schiffer, Y. Yang, *Nano Lett.* **2016**, *16*, 1009.
- 1986 [161] X. Li, W. Zhang, W. Zhang, H.-Q. Wang, J. Fang, *Nano Energy* **2019**, *58*, 825.
- 1987 [162] P. Guo, Q. Ye, X. Yang, J. Zhang, F. Xu, D. Shchukin, B. Wei, H. Wang, *J. Mater.*
1988 *Chem. A* **2019**, *7*, 2497.
- 1989 [163] T. Niu, J. Lu, R. Munir, J. Li, D. Barrit, X. Zhang, H. Hu, Z. Yang, A. Amassian, K.
1990 Zhao, S. Liu, *Adv. Mater.* **2018**, *30*, 1706576.
- 1991 [164] J. Xu, A. Buin, A. H. Ip, W. Li, O. Voznyy, R. Comin, M. Yuan, S. Jeon, Z. Ning, J. J.
1992 McDowell, P. Kanjanaboos, J.-P. Sun, X. Lan, L. N. Quan, D. H. Kim, I. G. Hill, P.
1993 Maksymovych, E. H. Sargent, *Nat. Commun.* **2015**, *6*, 7081.
- 1994 [165] W. Li, S. K. Yadavalli, D. Lizarazo-Ferro, M. Chen, Y. Zhou, N. P. Padture, R. Zia,
1995 *ACS Energy Lett.* **2018**, *3*, 2669.

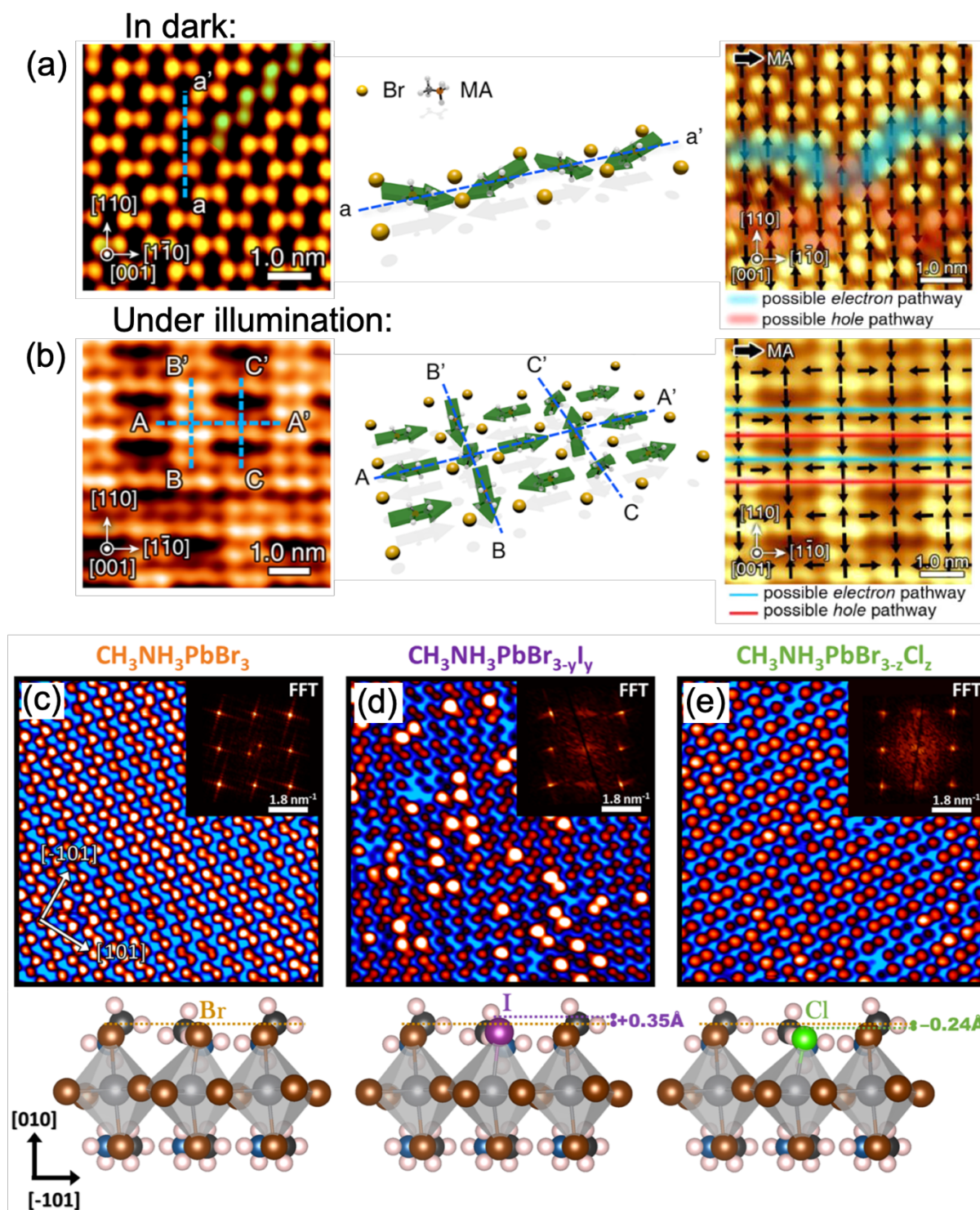
- 1996 [166] (a) Y. B. Qi, *Surf. Sci. Rep.* **2011**, *66*, 379; (b) E. M. Tennyson, J. M. Howard, M. S.
 1997 Leite, *ACS Energy Lett.* **2017**, *2*, 1825; (c) R. Giridharagopal, P. A. Cox, D. S. Ginger,
 1998 *Acc. Chem. Res.* **2016**, *49*, 1769.
- 1999 [167] D. H. Kim, J. Park, Z. Li, M. Yang, J.-S. Park, I. J. Park, J. Y. Kim, J. J. Berry, G.
 2000 Rumbles, K. Zhu, *Adv. Mater.* **2017**, *29*, 1606831.
- 2001 [168] L. K. Ono, Y. B. Qi, S. F. Liu, *Joule* **2018**, *2*, 1961.
- 2002 [169] H. J. Snaith, A. Abate, J. M. Ball, G. E. Eperon, T. Leijtens, N. K. Noel, S. D. Stranks,
 2003 J. T.-W. Wang, K. Wojciechowski, W. Zhang, *J. Phys. Chem. Lett.* **2014**, *5*, 1511.
- 2004 [170] (a) L. Collins, M. Ahmadi, T. Wu, B. Hu, S. V. Kalinin, S. Jesse, *ACS Nano* **2017**, *11*,
 2005 8717; (b) Y. Almadori, D. Moerman, J. L. Martinez, P. Leclère, B. Grévin, *Beilstein J.*
 2006 *Nanotechnol.* **2018**, *9*, 1695.
- 2007 [171] H. Tian, L. Zhao, X. Wang, Y.-W. Yeh, N. Yao, B. P. Rand, T.-L. Ren, *ACS Nano*
 2008 **2017**, *11*, 12247.
- 2009 [172] (a) S. Silver, Q. Dai, H. Li, J.-L. Brédas, A. Kahn, *Adv. Energy Mater.* *0*, 1901005; (b)
 2010 R. Giridharagopal, J. T. Pecht, S. Jariwala, L. Collins, S. Jesse, S. V. Kalinin, D. S.
 2011 Ginger, *ACS Nano* **2019**, *13*, 2812.
- 2012 [173] Y. Zhou, C. Fuentes-Hernandez, J. Shim, J. Meyer, A. J. Giordano, H. Li, P. Winget,
 2013 T. Papadopoulos, H. Cheun, J. Kim, M. Fenoll, A. Dindar, W. Haske, E. Najafabadi,
 2014 T. M. Khan, H. Sojoudi, S. Barlow, S. Graham, J.-L. Brédas, S. R. Marder, A. Kahn,
 2015 B. Kippelen, *Science* **2012**, *336*, 327.
- 2016 [174] (a) D. I. Patel, S. Bahr, P. Dietrich, M. Meyer, A. Thißen, M. R. Linford, *Surface*
 2017 *Science Spectra* **2019**, *26*, 024002; (b) J. Chun-Ren Ke, A. S. Walton, D. J. Lewis, A.
 2018 Tedstone, P. O'Brien, A. G. Thomas, W. R. Flavell, *Chemical Communications* **2017**,
 2019 *53*, 5231; (c) J. Lin, M. Lai, L. Dou, C. S. Kley, H. Chen, F. Peng, J. Sun, D. Lu, S. A.
 2020 Hawks, C. Xie, F. Cui, A. P. Alivisatos, D. T. Limmer, P. Yang, *Nat. Mater.* **2018**, *17*,
 2021 261; (d) J. C.-R. Ke, D. J. Lewis, A. S. Walton, B. F. Spencer, P. O'Brien, A. G.
 2022 Thomas, W. R. Flavell, *J. Mater. Chem. A* **2018**, *6*, 11205.
- 2023 [175] (a) K. Motoki, Y. Miyazawa, D. Kobayashi, M. Ikegami, T. Miyasaka, T. Yamamoto,
 2024 K. Hirose, *J. Appl. Phys.* **2017**, *121*, 085501; (b) B.-A. Chen, J.-T. Lin, N.-T. Suen,
 2025 C.-W. Tsao, T.-C. Chu, Y.-Y. Hsu, T.-S. Chan, Y.-T. Chan, J.-S. Yang, C.-W. Chiu,
 2026 H. M. Chen, *ACS Energy Lett.* **2017**, *2*, 342.
- 2027 [176] (a) L. T. Schelhas, J. A. Christians, J. J. Berry, M. F. Toney, C. J. Tassone, J. M.
 2028 Luther, K. H. Stone, *ACS Energy Lett.* **2016**, *1*, 1007; (b) M. Alsari, O. Bikondoa, J.
 2029 Bishop, M. Abdi-Jalebi, L. Y. Ozer, M. Hampton, P. Thompson, M. T. Hörantner, S.
 2030 Mahesh, C. Greenland, J. E. Macdonald, G. Palmisano, H. J. Snaith, D. G. Lidzey, S.
 2031 D. Stranks, R. H. Friend, S. Lilliu, *Energy Environ. Sci.* **2018**, *11*, 383.
- 2032 [177] (a) L. K. Ono, T. Kim, Y. Jiang, Y. B. Qi, S. F. Liu, *ACS Energy Lett.* **2018**, *3*, 1898;
 2033 (b) L. K. Ono, N.-G. Park, K. Zhu, W. Huang, Y. B. Qi, *ACS Energy Lett.* **2017**, *2*,
 2034 1749; (c) L. Qiu, S. He, L. K. Ono, S. Liu, Y. B. Qi, *ACS Energy Lett.* **2019**, DOI:
 2035 10.1021/acsenerylett.9b01396.
- 2036 [178] M. A. Green, E. D. Dunlop, D. H. Levi, J. Hohl-Ebinger, M. Yoshita, A. W. Y. Ho-
 2037 Baillie, *Prog. Photovolt. Res. Appl.* **2019**, *27*, 565.
- 2038 [179] (a) H. S. Kim, C. R. Lee, J. H. Im, K. B. Lee, T. Moehl, A. Marchioro, S. J. Moon, R.
 2039 Humphry-Baker, J. H. Yum, J. E. Moser, M. Grätzel, N. G. Park, *Sci. Rep.* **2012**, *2*,
 2040 591; (b) Z. Hawash, L. K. Ono, Y. B. Qi, *Adv. Mater. Interfaces* **2018**, *5*, 1700623; (c)
 2041 L. K. Ono, Z. Hawash, E. J. Juarez-Perez, L. B. Qiu, Y. Jiang, Y. B. Qi, *J Phys D Appl*
 2042 *Phys* **2018**, *51*.
- 2043 [180] L. Han, *Nature* **2019**, *567*, 465.
- 2044 [181] A. Kojima, K. Teshima, Y. Shirai, T. Miyasaka, *J. Am. Chem. Soc.* **2009**, *131*, 6050.
- 2045 [182] J.-H. Im, C.-R. Lee, J.-W. Lee, S.-W. Park, N.-G. Park, *Nanoscale* **2011**, *3*, 4088.

- 2046 [183] J. Burschka, N. Pellet, S. J. Moon, R. Humphry-Baker, P. Gao, M. K. Nazeeruddin,
2047 M. Grätzel, *Nature* **2013**, *499*, 316.
- 2048 [184] N. J. Jeon, J. H. Noh, Y. C. Kim, W. S. Yang, S. Ryu, S. I. Seok, *Nat Mater* **2014**, *13*,
2049 897.
- 2050 [185] N. J. Jeon, J. H. Noh, W. S. Yang, Y. C. Kim, S. Ryu, J. Seo, S. I. Seok, *Nature* **2015**,
2051 *517*, 476.
- 2052 [186] W. S. Yang, J. H. Noh, N. J. Jeon, Y. C. Kim, S. Ryu, J. Seo, S. I. Seok, *Science* **2015**,
2053 *348*, 1234.
- 2054 [187] D. Bi, C. Yi, J. Luo, J.-D. Décoppet, F. Zhang, Shaik M. Zakeeruddin, X. Li, A.
2055 Hagfeldt, M. Grätzel, *Nat. Energy* **2016**, *1*, 16142.
- 2056 [188] M. Saliba, T. Matsui, J.-Y. Seo, K. Domanski, J.-P. Correa-Baena, M. K.
2057 Nazeeruddin, S. M. Zakeeruddin, W. Tress, A. Abate, A. Hagfeldt, M. Grätzel, *Energy*
2058 *Environ. Sci.* **2016**, *9*, 1989.
- 2059 [189] Q. Jiang, Y. Zhao, X. Zhang, X. Yang, Y. Chen, Z. Chu, Q. Ye, X. Li, Z. Yin, J. You,
2060 *Nat. Photon.* **2019**, DOI: 10.1038/s41566.
- 2061 [190] (a) Y. Y. Zhou, M. J. Yang, W. W. Wu, A. L. Vasiliev, K. Zhu, N. P. Padture, *J.*
2062 *Mater. Chem. A* **2015**, *3*, 8178; (b) M. A. Green, Y. Hishikawa, E. D. Dunlop, D. H.
2063 Levi, J. Hohl-Ebinger, M. Yoshita, A. W. Y. Ho-Baillie, *Prog. Photovolt. Res. Appl.*
2064 **2019**, *27*, 3.
- 2065 [191] T. W. Kim, N. Shibayama, L. Cojocaru, S. Uchida, T. Kondo, H. Segawa, *Adv. Funct.*
2066 *Mater.* **2018**, *28*, 1804039.
- 2067 [192] Y. Luo, P. Khoram, S. Brittman, Z. Zhu, B. Lai, S. P. Ong, E. C. Garnett, D. P.
2068 Fenning, *Adv. Mater.* **2017**, *29*, 1703451.
- 2069 [193] Y. Zhong, R. Munir, J. Li, M.-C. Tang, M. R. Niazi, D.-M. Smilgies, K. Zhao, A.
2070 Amassian, *ACS Energy Lett.* **2018**, *3*, 1078.
- 2071



2072

2073 **Figure 1.** a) Spatially resolved imaging on photoinduced charge transfer behaviors in
 2074 perovskite grains under light illumination mapped by light-modulated scanning tunneling
 2075 microscopy. Reprinted with permission from ref. ^[15]. Copyright 2017, American Chemical
 2076 Society. b) A method based on Kelvin probe force microscopy that enables mapping of charge
 2077 redistribution in an operating device upon a voltage- or light pulse with sub-millisecond
 2078 resolution was developed. Reprinted with permission from ref. ^[12c]. Copyright 2018, The Royal
 2079 Society of Chemistry. c) Possible charge excitation, recombination, transport, and extraction at
 2080 electrodes processes and the corresponding time-scale taking place in PSCs. Reprinted with
 2081 permission from ref. ^[9a]. Copyright 2018, Elsevier Ltd. The picture in the left side as inset
 2082 (octahedron dynamics in ps time scale) in panel c) was reprinted with permission from ref. ^[29a].
 2083 The picture in the right side as inset (ion migration in ms to s time scale) was reprinted with
 2084 permission from ref. ^[10g]. Copyright 2016, The Royal Society of Chemistry.



2085

2086

2087

2088

2089

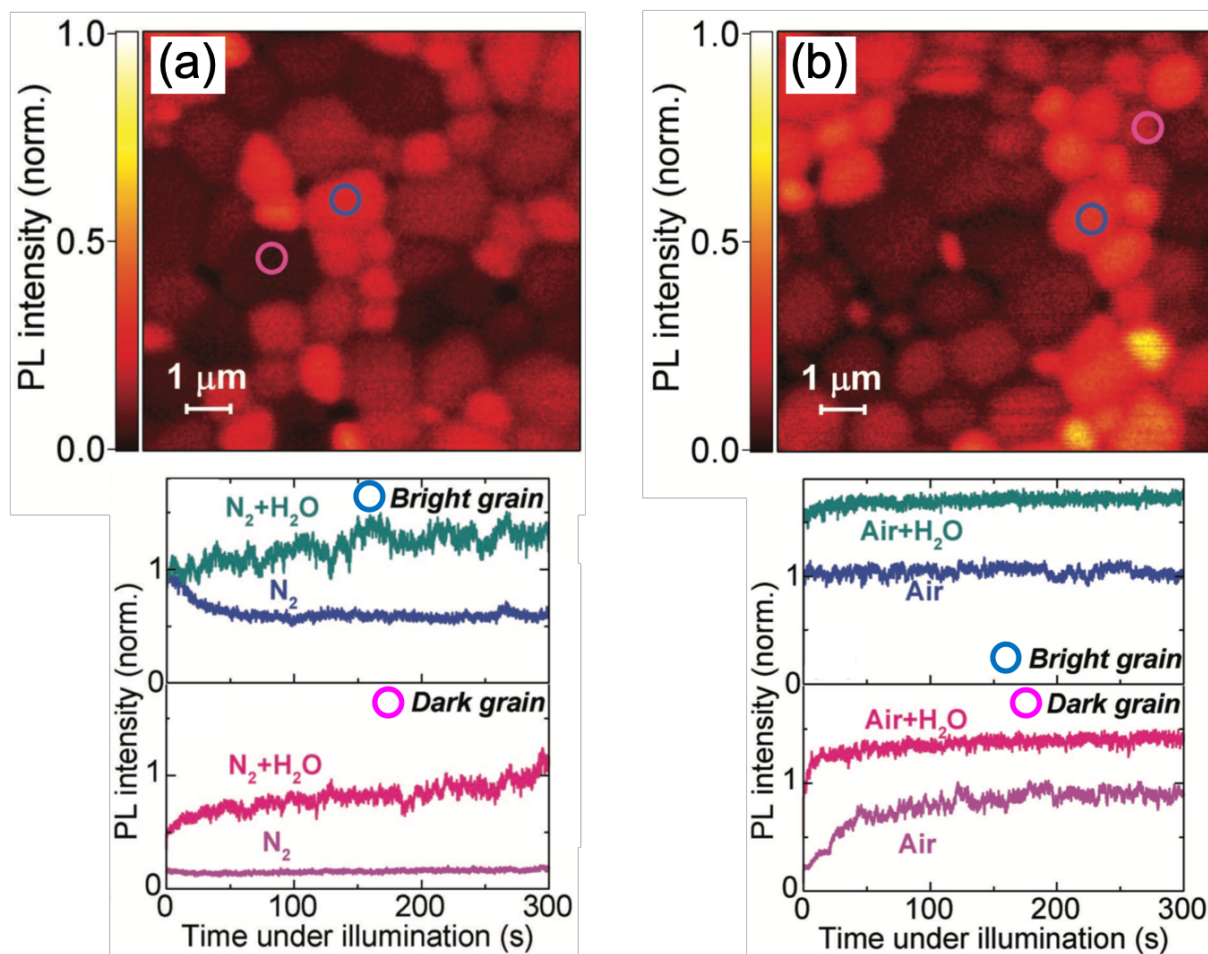
2090

2091

2092

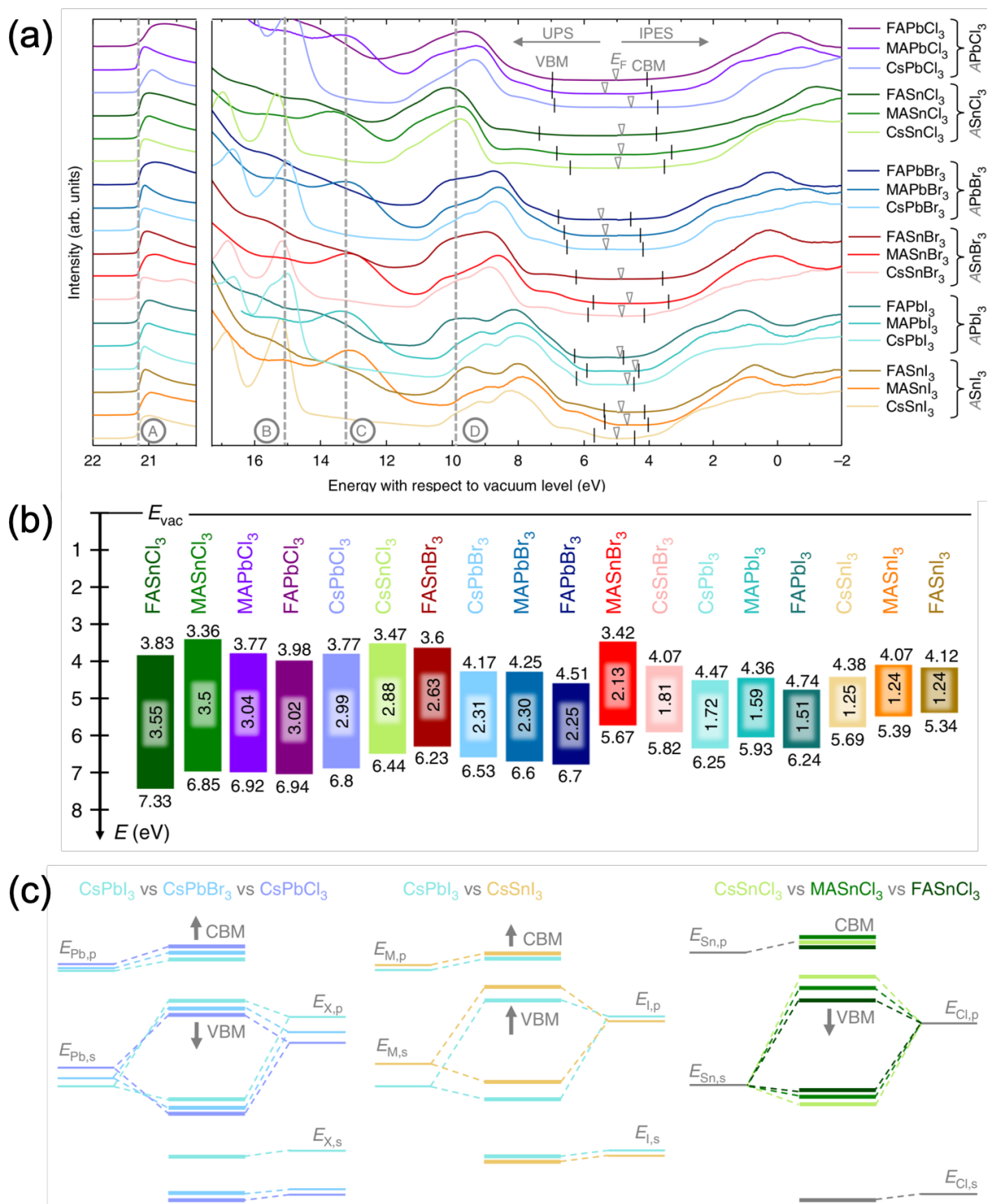
Figure 2. a) Comparison of the surface structure and molecule orientation pattern in the dark and b) under illumination. STM images reveal a transition from a) the dominant dimer structure in dark to b) a 4×2 structure under laser illumination. DFT calculations reveal CH_3NH_3^+ molecule dipole alignments lead to the transition from a) to b) surface pattern under illumination. The orientation of CH_3NH_3^+ molecule dipoles are indicated by arrows. The blue lines indicate a low electron potential energy pathway and the red ones indicate a low hole potential energy pathway. The fading out illustrates the lack of potential modulation in the 2×2 phase in dark.

2093 A movie showing the proposed model of MA rotation and its influence on Br surface
2094 arrangement is available as supplementary work in this work. Reprinted with permission from
2095 ref. ^[26]. Copyright 2019, American Chemical Society. c-e) Large area STM images (10 nm ×
2096 10 nm) of the c) pristine CH₃NH₃PbBr₃, d) CH₃NH₃PbBr_{3-y}I_y, and e) CH₃NH₃PbBr_{3-z}Cl_z
2097 mixed-halide perovskites. Inset: FFT results obtained from the topographic STM images
2098 showing no additional peak at low k-values for the mixed-halide perovskite, suggesting that
2099 there is no long-range ordering of the additional iodine and chlorine ions at the surface. Relative
2100 positions of the I (+0.35 Å) and Cl (-0.24 Å) ions with respect to the top CH₃NH₃Br₃ structure.
2101 Color code: Pb (gray), Br (brown), I (purple), Cl (green), C (black), N (blue), H (light pink).
2102 Reprinted with permission from ref. ^[27]. Copyright 2019, American Chemical Society.
2103



2104

2105 **Figure 3.** Microscale confocal PL map of a MAPbI₃ perovskite film in a) dry nitrogen, and
 2106 humidified nitrogen (~45% RH), b) dry air, and humidified air (~45% RH) normalized to the
 2107 maximum intensity. PL intensity as a function of time under illumination from a bright grain
 2108 (blue circle) and a dark grain (pink circle) under the different gas environment. The PL intensity
 2109 for each trace over time is given relative to the starting value for the bright grain in nitrogen,
 2110 which is normalized to 1. Reprinted with permission from ref. [45b]. Copyright 2018, WILEY-
 2111 VCH Verlag GmbH & Co. KGaA, Weinheim.



2112

2113 **Figure 4.** a) UPS and IPES spectra of 18 Sn- and Pb-based halide perovskites. For easy

2114 comparison, the secondary electron cutoff (SECO) onsets were aligned at the He-I α excitation

2115 energy (21.22 eV), marked by line A. Lines, B, C, and D indicate the common features

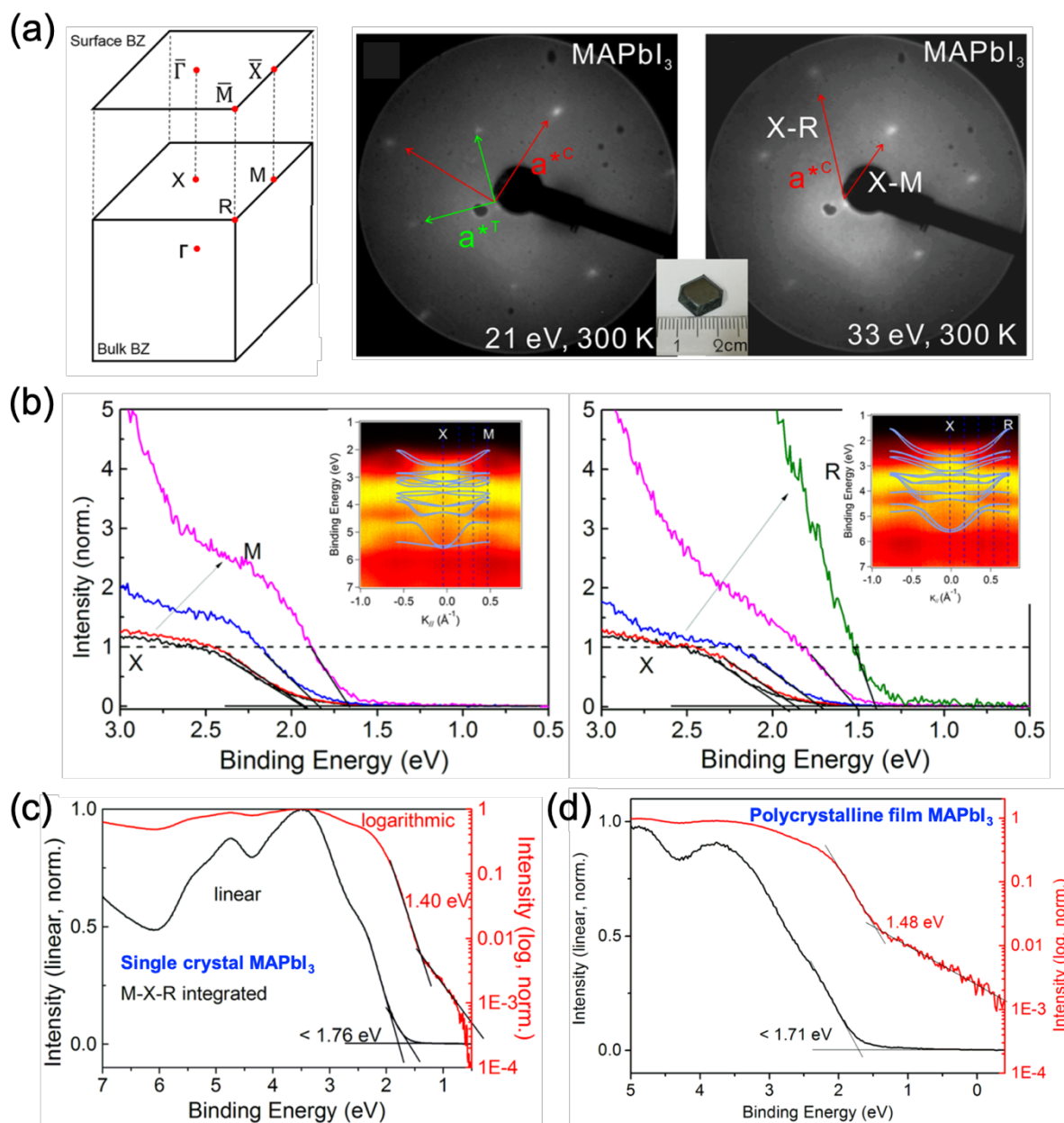
2116 corresponding to the Cs, MA, and FA related states, respectively. The extracted absolute

2117 positions of IE and EA are indicated by vertical markers, while E_F is indicated by triangles.

2118 b) Diagram of energy levels of the 18 metal halide perovskites with IE, EA, and E_{Opt} values

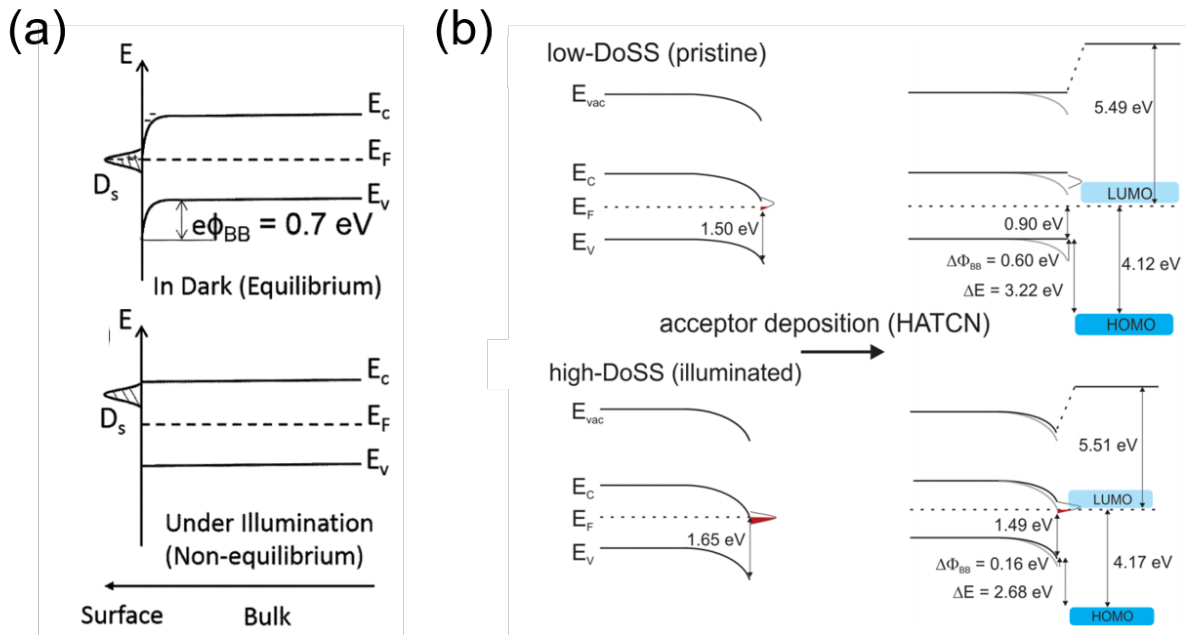
2119 indicated in eV. Minor deviations between E_{Opt} and difference between IE and EA (i.e., E_G) can

2120 be inferred and assigned to contribution of exciton bind energy and/or error measurements. c)
2121 Trends of changes in energy levels in ABX_3 perovskites when varying the X halide anions (left
2122 panel), M metal cations (middle panel), and A cations (right panel). Arrows indicate the
2123 direction of shifts in energy levels upon the anion or cation substitutions. Reprinted with
2124 permission from ref. ^[49c]. Copyright 2019, Springer Nature.
2125



2126

2127 **Figure 5.** a) Schematic of the surface and first bulk Brillouin zone (BZ) of a cubic lattice. LEED
 2128 patterns of (001) plane of MAPbI₃ single crystal acquired at electron energies of 21 eV and 33
 2129 eV at 295 K. The reciprocal lattice parameters a^{*C} and a^{*T} refer to the cubic and tetragonal
 2130 phases, respectively. b) Photoemission spectra for defined emission angles with selected wave
 2131 vector (k) values along the X—M and X—R directions. Inset shows the band structure of of
 2132 MAPbI₃ single crystal measured ARPES. c) Integrated photoemission spectra of all k values
 2133 along the X—M and X—R directions acquired on MAPbI₃ single crystal, which translates to a
 2134 simulated polycrystalline MAPbI₃ film. d) Actual UPS measurements on the polycrystalline
 2135 film of MAPbI₃. The photoemission intensities are displayed in linear and logarithmic scales to
 2136 highlight the variations in the onset of VBM determination. Reprinted with permission from ref.
 2137 [52]. Copyright 2019, American Chemical Society.



2138

2139

2140

2141

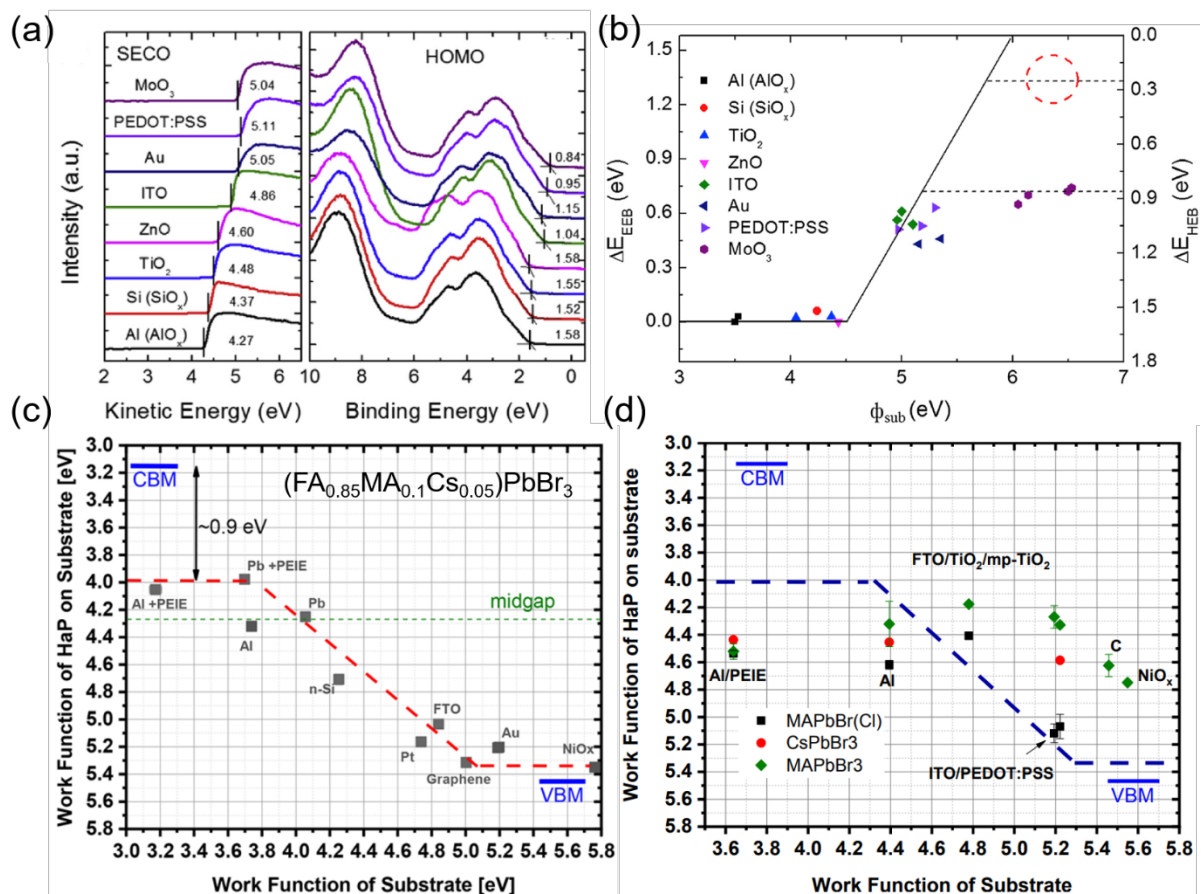
2142

2143

2144

2145

Figure 6. Effect of surface states on the band structure of MAPbI₃. a) the surface band bending is caused by the surface trap states with E_F pinned to CBM. Under illumination the traps are filled with photo-excited charges and the flat band structure is formed. Reprinted from ref. ^[55b] Copyright 2017, WILEY-VCH Verlag GmbH & Co. KGaA, Weinheim. b) the density of surface state influence the energy level alignment with the coating of ETL. Reprinted from ref. ^[55a]. Copyright 2017, American Chemical Society.



2146

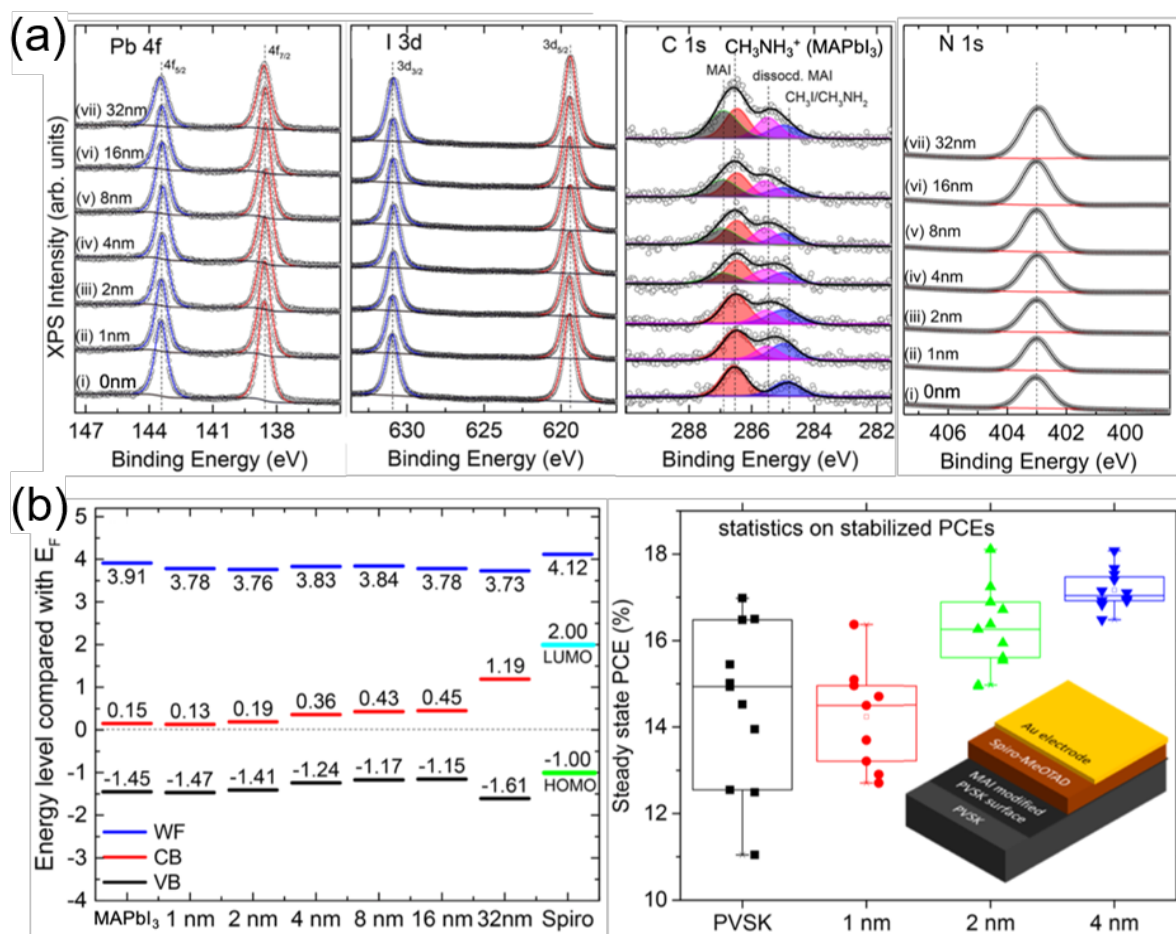
2147 **Figure 7.** Influence of the underlying substrate on the perovskite electronic properties. a) and2148 b) evaporated MAPbI₃ on substrate with increasing WF. The deposited MAPbI₃ also shows

2149 increased WF and shift of VBM to lower binding energy. Reprinted from ref. [59a]. Copyright

2150 2017, Elsevier Ltd. c) the WF evolution of (FA_{0.85}MA_{0.1}Cs_{0.05})PbBr₃ on the substrates with2151 increasing WF. d) the WF evolution of MAPbBr(Cl), MAPbBr₃ and CsPbBr₃ on the substrates

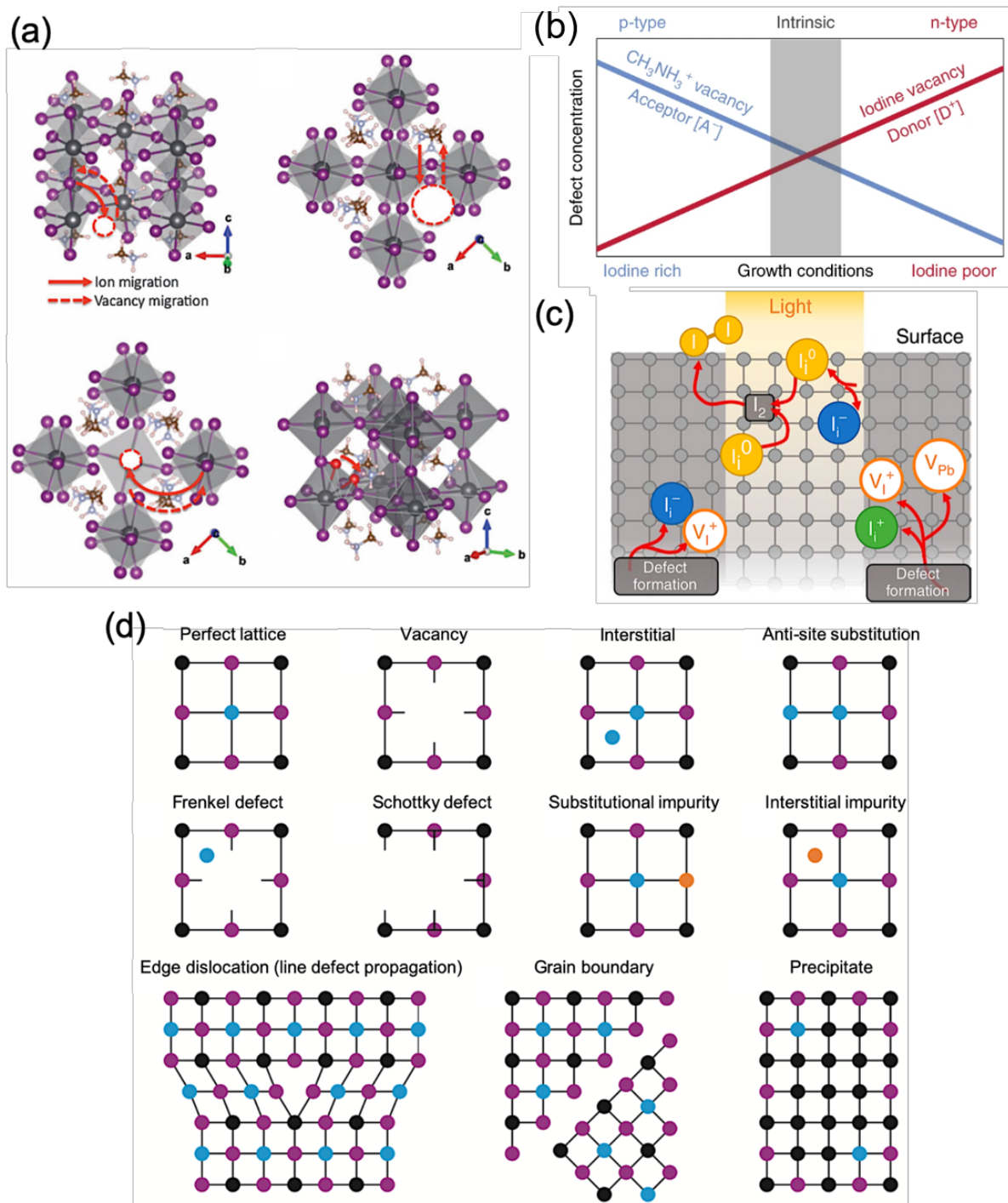
2152 with increasing WF. Reprinted from ref. [67]. Copyright 2019, American Chemical Society.

2153



2154

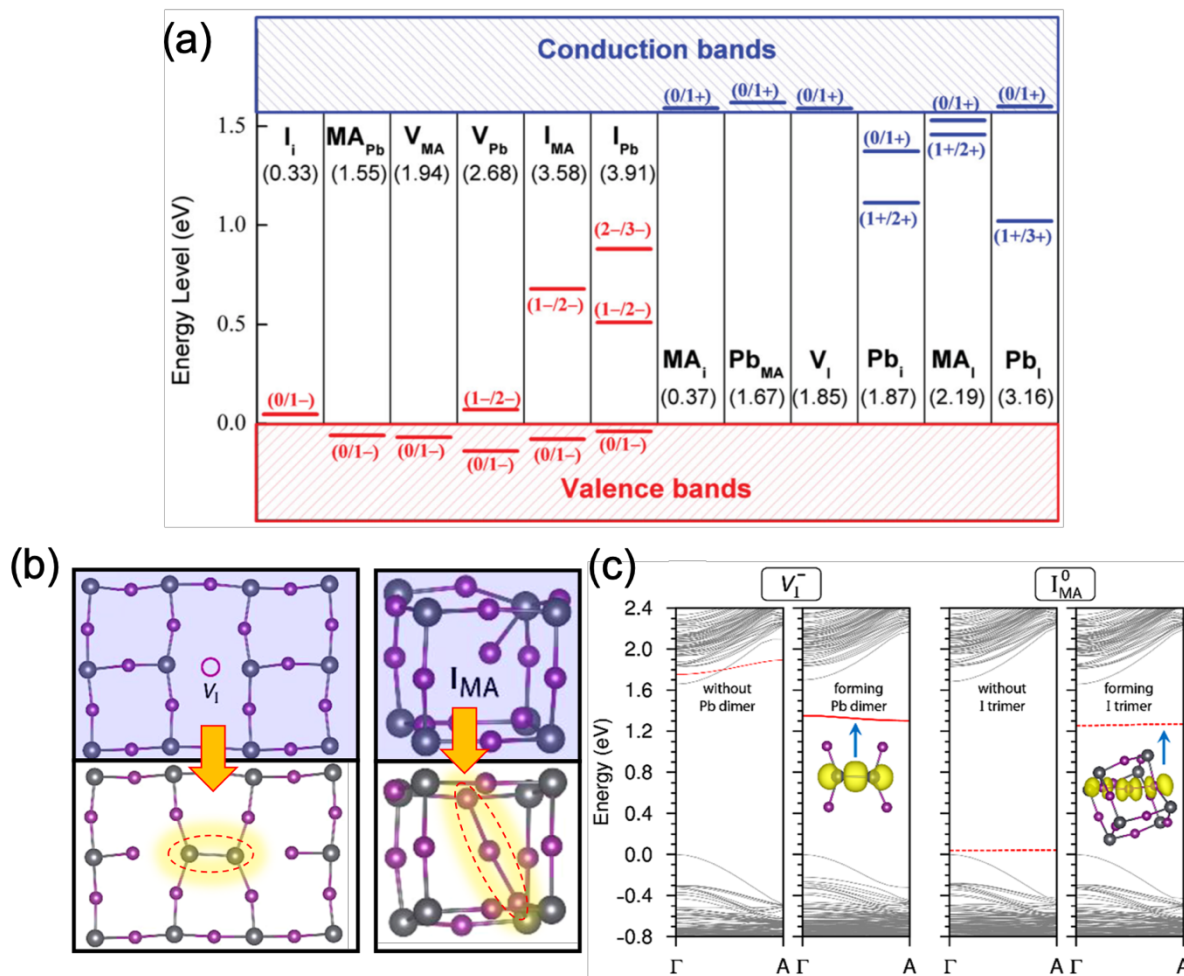
2155 **Figure 8.** a) XPS spectra ($Al\text{-}K\alpha = 1486.6$ eV) corresponding to Pb 4f, I 3d, C 1s, and N 1s core
 2156 levels of the pristine MAPbI₃ perovskite and after depositing additional excess of MAI layer
 2157 (from 1 nm up to 32 nm). b) (Left panel) Schematic energy diagram of valence band (VB),
 2158 conduction band (CB), and work function (WF) with respect to the Fermi level (E_F). (Right
 2159 panel) Statistics of steady-state PCEs with MAPbI₃-based PSCs as a function of excess MAI
 2160 layer thickness. A schematic of device architecture with interface modification is shown in the
 2161 inset. Reprinted with permission from ref. [49m]. Copyright 2017, American Chemical Society.



2162
 2163
 2164
 2165
 2166
 2167
 2168
 2169
 2170

Figure 9. a) Migration pathways for the vacancies of iodine (V_I), methylammonium (V_{MA}), lead (V_{Pb}), and interstitial iodine (I_i) defects. Solid lines represent migration of the ions, while the dashed lines indicate trajectories of the vacancies. Reprinted with permission from ref. [87a]. Copyright 2015, The Royal Society of Chemistry. b) Control of defect concentration in MAPbI₃ that can be achieved during crystal growth and annealing. Three regimes in MAPbI₃ semiconductor behavior leading to n-type (electron rich), p-type (hole rich), and intrinsic ([A⁺] ~ [D⁻]) characteristics. Reprinted with permission from ref. [88]. Copyright 2019, Springer Nature. c) Dynamics of light-induced degradation in MAPbI₃. On the basis of hybrid-DFT,

2171 MAPbI₃ shows the defect chemistry dominated by Pb vacancy (V_{Pb}) and interstitial iodide (I_i).
2172 Proposal of I_i^+/I_i^- pair defect formation: (i) $\text{MAPbI}_3 \rightarrow V_{\text{Pb}}^{2-} + V_{\text{I}}^+ + I_i^+$ and (ii) $\text{MAPbI}_3 \rightarrow V_{\text{I}}^+$
2173 $+ I_i^-$. Sequential electron and hole trapping take place on the I_i^+/I_i^- pair defect leading to I_2 : I_i^+/I_i^-
2174 $+ 1e \rightarrow I_i^0/I_i^- + 1h \rightarrow 2I_i^0 \rightarrow I_2$. A surface-coordinated I_2 molecule can remain bound to the
2175 surface or grain boundary. Reprinted with permission from ref. [89]. Copyright 2019, Springer
2176 Nature. d) Illustration of the type of defects in perovskite crystal lattice: blue, black, and purple
2177 dots represent A, M, and X site ions, respectively. Orange dots represent impurity atoms.
2178 Defects are often divided into two categories of point defects (i.e., vacancy, interstitial, anti-
2179 site substitution, Frenkel and Schottky defects, substitutional and interstitial impurities) and
2180 dimensional defects (i.e., edge dislocation (line defect propagation), grain boundary, and
2181 precipitates). Theoretical studies provide useful but limited guidance as the results are
2182 dependent on the choice of modules and calculation methods, especially the dimensional
2183 defects, which has a relatively larger model system size and complex environment. Reprinted
2184 with permission from ref. [90c]. Copyright 2016, Springer Nature.
2185

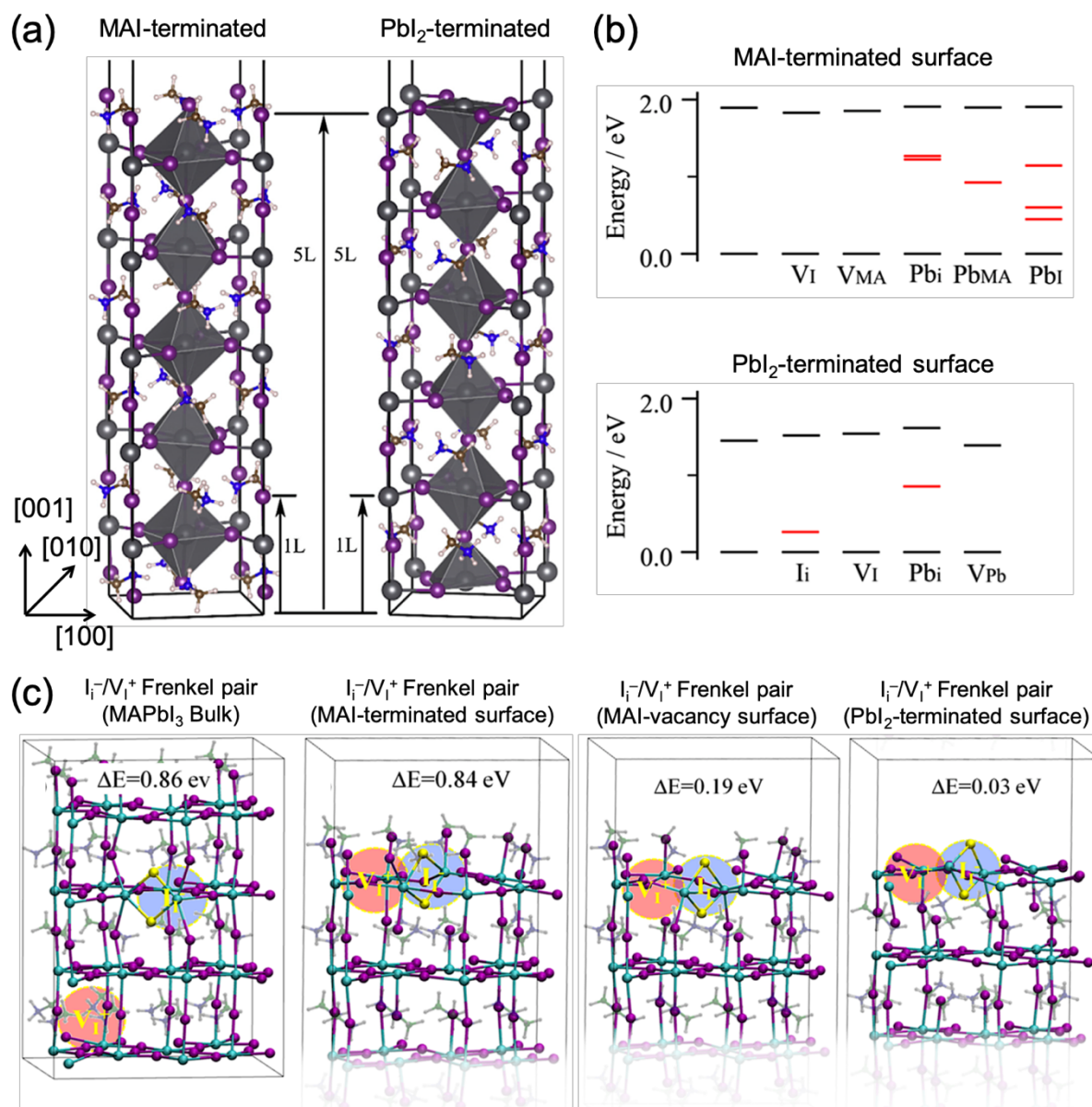


2186

2187 **Figure 10.** a) Calculated defect energy levels of point defects. The formation energies of defects2188 are indicated by the values within parenthesis. The acceptor (red) type and donor (blue) type of
2189 defects are ordered by the formation energies. Reprinted with permission from ref. [76a].2190 Copyright 2014, WILEY-VCH Verlag GmbH & Co. KGaA, Weinheim. b) Atomic structure
2191 changes before (shaded) and after (non-shaded) illustrating the steps for the formation of Pb2192 dimer from V_I and I trimer from I_{MA} . c) Reprinted with permission from ref. [95]. Copyright

2193 2014, American Chemical Society.

2194

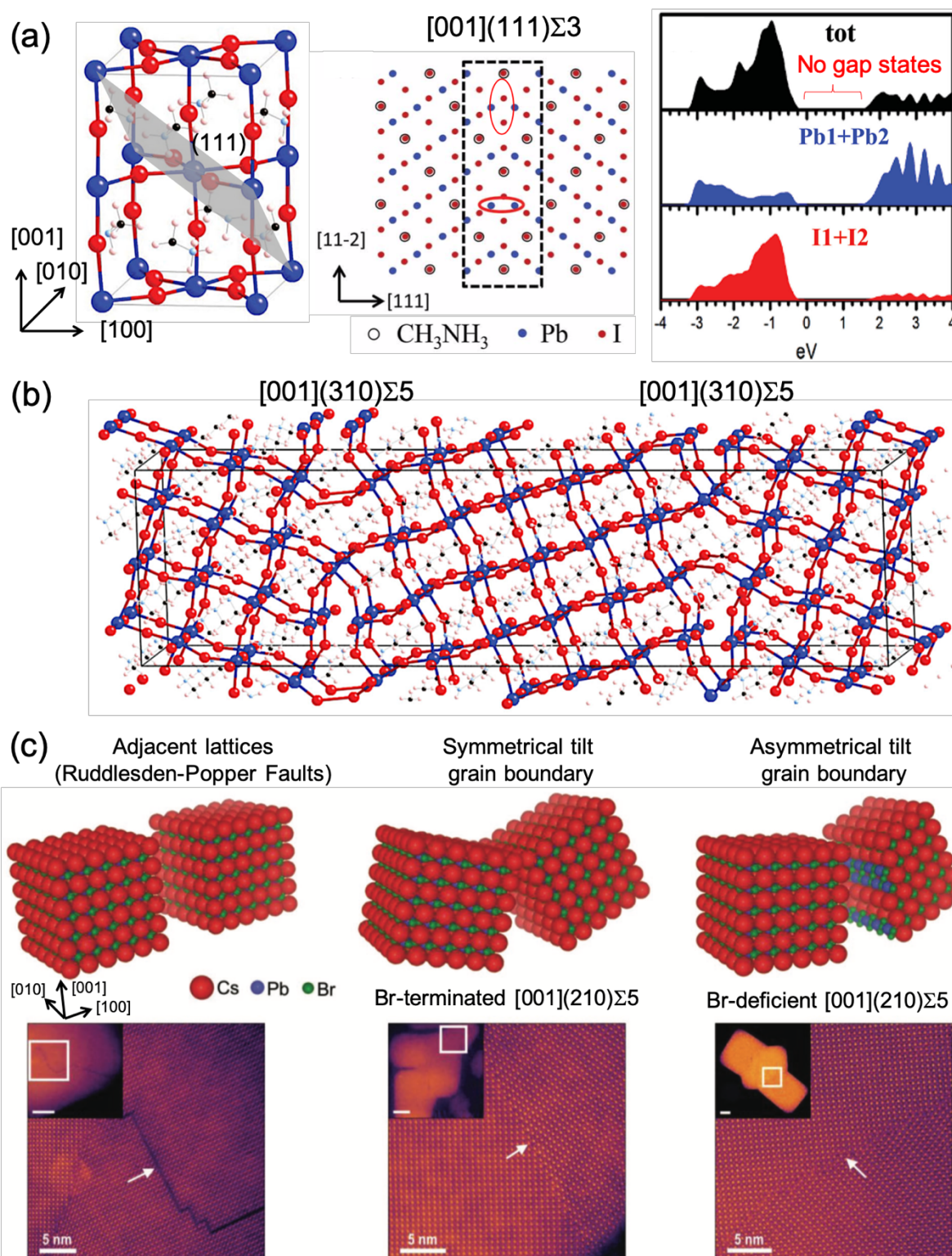


2195
 2196 **Figure 11.** a) DFT optimized geometrical structures of 5-layer slabs with (001) surface of
 2197 MAPbI₃ perovskite including a vacuum layer of 20 Å. Two surface terminations are widely
 2198 studied: MAI- and PbI₂-terminated surfaces. Reprinted with permission from ref. [102g].
 2199 Copyright 2015, Elsevier Ltd. b) VBM, CBM, and point defects energy levels with respect to
 2200 the VBM ($E = 0$). Defect levels are represented by red horizontal lines, while the VBM and
 2201 CBM are represented by the lower and upper black lines, respectively. Reprinted with
 2202 permission from ref. [102c]. Copyright 2017, American Chemical Society. c) Optimized
 2203 structures and formation energies for I_i⁻/V_I⁺ Frenkel pair in the MAPbI₃ bulk, at MAI-
 2204 terminated surface, at a MAI-vacant site, and at PbI₂-terminated surface. Reprinted with
 2205 permission from ref. [56]. Copyright 2019, American Chemical Society.

2206

2207

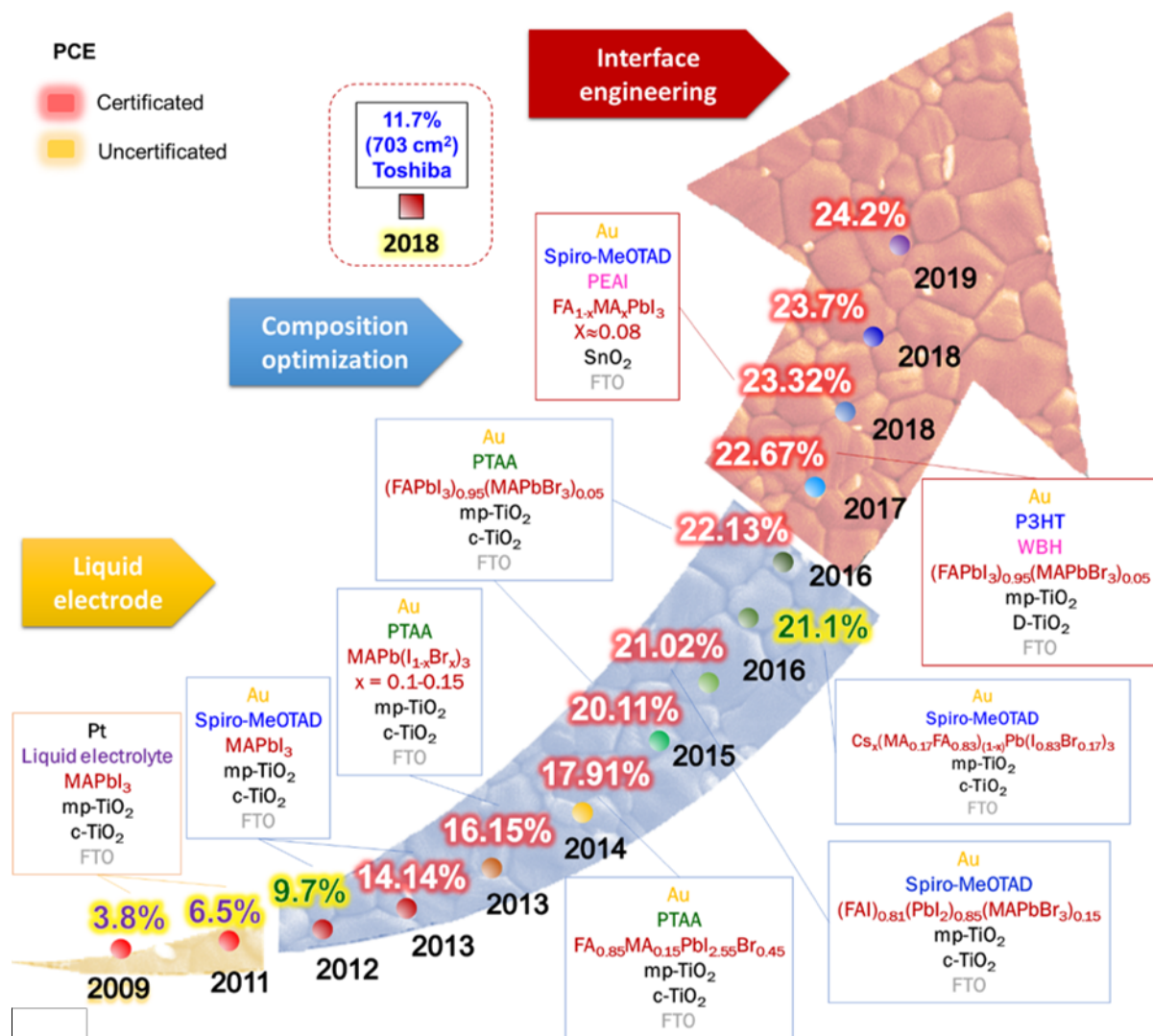
2208



2209

2210 **Figure 12.** a) Tetragonal MAPbI₃ crystal structure phase. Structural model for a [001](111)Σ₃
 2211 grain boundary in MAPbI₃. The red circles indicate the new bonds formed at the grain boundary,
 2212 which DFT calculations reveal the non-generation of deep level defects. b) Schematic of a super
 2213 cell structure of [001](310)Σ₅ grain boundary. Reprinted with permission from ref. [76b].
 2214 Copyright 2015, WILEY-VCH Verlag GmbH & Co. KGaA, Weinheim. c) Schematic

2215 formation of different planar faults of Ruddlesden-Popper (RP), Br-terminated and Br-deficient
2216 [001](210) Σ 5 during the fusion of CsPbBr₃ nanocrystals and their respective HAADF images.
2217 Reprinted with permission from ref. ^[8a]. Copyright 2019, WILEY-VCH Verlag GmbH & Co.
2218 KGaA, Weinheim.
2219



2220
 2221 **Figure 13.** Selected lab-scale perovskite-based solar cell efficiencies and their corresponding
 2222 device architecture evolved over the years.^[25, 44, 179b] The corresponding references to each of
 2223 the efficiency numbers are as following: 3.8%,^[181] 6.5%,^[182] 9.7%,^[179a] 14.1%,^[183] 16.15%,^[184]
 2224 17.91%,^[185] 20.11%,^[186] 21.02%,^[187] 21.1%,^[188] 22.13%,^[96a] 22.67%,^[83] 23.32%.^[189] The
 2225 certified efficiencies divulged by NREL are represented by red-colored numbers.^[190] Toshiba
 2226 Corporation holds the certified efficiency with the largest perovskite solar module (dash square
 2227 symbol).^[28a]

2228 **Table 1.** Selected microscopic studies that emphasize multi-modal measurements as well as focused on the dynamical processes taking place within
 2229 a PSC. This table is complementary to the one published in ref. [11].

2230

Technique; measurement conditions	Subject	Spatial resolution; detection depth; quantitative/qualitative	Static/Dynamic (movie availability)	Perovskite; processing	Main findings	Ref
STM/STS; UHV, 4.5 K.	Atomic surface structure and electronic structure.	Atomic resolution (~ 0.2 Å); top surface; quantitative	Static	MAPbBr ₃ single crystal.	<ul style="list-style-type: none"> • Surface reconstruction with dimmer and zigzag structures. • MABr-terminated surface. 	[42a]
STM; 78 K.	Atomic surface structure and electronic structure.	Atomic resolution (~ 0.2 Å); top surface; quantitative	Static	MAPbI ₃ polycrystalline film; vacuum deposition.	<ul style="list-style-type: none"> • Surface reconstruction with dimmer and zigzag structures. • MAI-terminated surface. 	[42b-d]
Cross-sectional STM/STS	Topography and electronic structure.	Atomic resolution (~ 0.2 Å); top surface; quantitative	Static	MAPbI _{3-x} Cl _x polycrystalline film; solution processed; 50 K.	<ul style="list-style-type: none"> • MAPbI_{3-x}Cl_x / Si(100) cleaved in-situ. • Two domains with different DOS are observed in the length scale of 10-20 nm. • DFT corroborates the scenario of local I/Cl stoichiometric ratios. • The domain with low dI/dV corresponds to lower I/Cl, while high dI/dV was attributed to high Cl-contents. 	[42e]
STM	Atomic surface structure.	Atomic resolution (~ 0.2 Å); top surface;	Static	MAPbBr ₃ , MAPbBr _{3-y} I _y and MAPbBr _{3-z} Cl _z polycrystalline films;	<ul style="list-style-type: none"> • Br ions substituted by I or Cl ions. • Substituted halides show randomly distributed. 	[27]

		quantitative		vacuum deposition; 5 K, UHV.	<ul style="list-style-type: none"> • disordered surface structure with no phase segregation. 	
Photoexcited cross-sectional STM/STS	Atomic surface structure under laser diode (532 nm, 140 mW/cm ²).	Atomic resolution (~0.2 Å); top surface; quantitative	Dynamic (yes)	MAPbBr ₃ single crystal; 4.3 K.	<ul style="list-style-type: none"> • Photo-induced atomic-scale reordering of MA cations. • Rotation of MA induced by excitation of electron-hole pairs in spatially displaced orbital states. 	[26]
Light-modulated STM; UHV; Laser diode (532 nm, 3 mW/cm ²); 100 K.	Topography and electronic structure mapping.	Atomic resolution (~0.2 Å); top surface; quantitative	Static; Comparison dark versus light.	MAPbI ₃ polycrystalline film on mp-TiO ₂ /c-TiO ₂ /SiO ₂ /Si; solution processed.	<ul style="list-style-type: none"> • Interfacial electronic structure at the heterointerfaces between MAPbI₃ and PbI₂. • Spatially resolved mapping images of photoinduced band bending of VB and CB. • Real-space observations of photocarrier generation. • Enhanced charge separation and reduced back recombination deduced for PbI₂ passivation layer 	[15]
Real-time in-situ HRTEM	Thermal degradation.	Atomic-scale; atomic-scale HRTEM observation of the outermost surface of the crystalline; qualitative	Dynamics (yes)	MAPbI ₃ on FTO	<ul style="list-style-type: none"> • Precipitation of trigonal PbI₂ grains and its detailed process during thermal degradation. • Precipitation of the PbI₂ grains did not originate directly from the crystalline MAPbI₃ layer, but from the amorphized MAPbI₃ layer. 	[191]

Frequency-modulation KPFM	CPD maps on cross-sectional complete devices.	A lateral resolution <50 nm; quantitative	Dynamic (no)	ITO/c-TiO ₂ /MAPbI ₃ /spiro-MeOTAD/Ag	<ul style="list-style-type: none"> • Upon illumination, space charge layers are formed at the interfaces of the selective contacts with MAPbI₃ layer within seconds. • Distinct differences in the charging dynamics at the interfaces of MAPbI₃ with adjacent layers are observed. • Such differences in charging rates at different interfaces were associated to a combination of ion migration and interfacial trap states. 	[24c]
KPFM	CPD maps on cross-sectional complete devices.	Nanometer resolution; quantitative	Static; poling the device with +1 V and -1 V.	FTO/c-TiO ₂ /(FA-MA)Pb(I-Br)/spiro-MeOTAD/Au	<ul style="list-style-type: none"> • Influence of extrinsic ions (Li⁺ ion migration). • Li⁺ ions in the HTL layer diffuse across the perovskite layer and accumulate in the ETL layer. • Accumulation of Li⁺ at the c-TiO₂ interface improves carrier injection from perovskite to c-TiO₂. 	[24d]
High-speed illuminated heterodyne-KPFM (16 s/scan); air (<15% RH); 500 nm	Topography and Voc mapping.	A lateral resolution <50 nm; quantitative	Dynamic (yes)	MAPbI ₃ polycrystalline film on PEDOT/ITO; solution processed.	<ul style="list-style-type: none"> • Local Voc mapping shows voltage variations >300 mV under 1-sun within a perovskite grain. • The time-dependent changes of local Voc were observed under dark conditions 	[90e]

laser light at 54 μ W.					and proposed due to reversible intragrain ion migration.	
Fast free force recovery (F^3R)-KPFM	CPD mapping with high temporal resolution ($>10 \mu$ s)	Quantitative	Dynamic (yes)	MAPbBr ₃ single crystal.	<ul style="list-style-type: none"> • Ion migration induced laterally across Au (drain)/MAPbBr₃/Au (source = ground) lateral device structure. • After drain voltage is switched on, a complex potential transient is observed, including both fast and slow processes, indicating that the imaging mechanism is not simply electronic in nature. • The establishment of the interface region does not appear instantaneous; instead, it is established $\sim 30 \mu$s after the removal of the field and disappears $\sim 92 \mu$s after the application of the field across the device. • These were correlated with the finite transport rates of ions in the material. 	[170a]
KPFM	Time-dependent mapping of surface photovoltage.	Quantitative	Dynamic (no)	MAPbBr ₃ single crystal.	<ul style="list-style-type: none"> • Interplay of convoluted processes of charge carrier dynamics and ion migration. • Time-dependent changes of the surface potential under illumination taking place on the scale of a few seconds. This time scale assigned to ion migration. 	[170b]

					<ul style="list-style-type: none"> • Photopotential decay at the sub-millisecond time scale was related to the photocarrier lifetime. 	
Time-resolved G-mode KPFM and fast free time-resolved (FF-tr)EFM.	CPD mapping with time resolution in the order of μs time scales.	Spatial resolution: 100 nm; Quantitative	Dynamic (yes)	Layered 2D perovskite of $(\text{C}_4\text{H}_9\text{NH}_3)_2\text{PbI}_4$.	<ul style="list-style-type: none"> • Under illumination, the photovoltage equilibrates over hundreds of μs, a time scale associated with ion migration and trapped electronic carriers. • On the contrary to 3D perovskites, the surface photovoltage of the 2D grain interiors evolves more rapidly in time than at the grain boundaries. • The slower evolution at grain boundaries was associated to a combination of ion migration occurring between PbI_4 planes in the 2D layered perovskite as well as electronic carriers traversing the traps present in grain boundaries. 	[172b]
Time resolved (tr-)KPFM	CPD maps on cross-sectional complete devices.	The lateral KPFM resolution of 50 nm; quantitative	Dynamic (yes)	Cross-section on FTO/SnO ₂ /(MA-FA)Pb(I-Br) perovskite/spiro-MeOTAD/Au	<ul style="list-style-type: none"> • A localized interfacial charge forms at the photoanode interface within 10 ms after applying a forward bias to the device. • After switching off the forward bias, these interfacial charges were stable for over 500 ms and created a reverse electric field in the cell. 	[12c]

					<ul style="list-style-type: none"> • This reverse electric field was associated with the higher photocurrents during reverse bias scans in I-V measurements (hysteresis). 	
KPFM and pc-AFM	CPD maps on MAPbI ₃ films deposited on ETL and HTL.	In nanometer resolution; quantitative	Dynamic, Light on/off with KPFM (no)	Three samples: S1. MAPbI ₃ /c-TiO ₂ /FTO. S2. MAPbI ₃ /PEDOT:PSS/FTO. S3. MAPbI ₃ /FTO.	<ul style="list-style-type: none"> • The average difference value (ΔV) of CPD values obtained between in dark and under illumination is associated with the efficacy for charge extraction at perovskite/contact layer interfaces. • The magnitude of ΔV is related to the density of charge carrier at the surface, while ΔV polarity is associated to the type of charge carrier (electrons or holes). 	[13b]
KPFM; N ₂ filled glovebox; >50 mW/cm ² from 350 to 750 nm.	CPD maps on cross-sectional complete devices.	Lateral resolution 20~50 nm; quantitative	Static; Comparison dark versus light.	Cell 1. ITO/TiO ₂ /MAPbI ₃ /spiro-MeOTAD/Au; Cell 2. ITO/C ₆₀ -C ₆ -PA SAM/MAPbI ₃ /spiro-MeOTAD/Au	<ul style="list-style-type: none"> • Under J_{sc} or V_{oc} conditions, SAM cell showed higher positive potential (LCPD profiles). This high potential (i.e., charge-up) for SAM cell was higher than for TiO₂ cell. • The positive charge-up means an unbalanced e-h extractions with a more efficient electron extraction in SAM cells. 	[24c]
KPFM	CPD maps on cross-sectional complete devices.	Quantitative	Static	Cell 1 (planar). FTO/c-TiO ₂ /MAPbI ₃ (excess PbI ₂ or MAI)/spiro-MeOTAD/Ag;	<ul style="list-style-type: none"> • The diode junction behaves differently between planar and mesoporous PSCs. • Regardless of MAPbI₃ stoichiometry (PbI₂- or MAI-rich conditions), a major 	[22]

				Cell 2 (mesoporous). FTO/c-TiO ₂ /mp-TiO ₂ +MAPbI ₃ (excess PbI ₂ or MAI)/spiro-MeOTAD/Ag	potential drop takes place at the perovskite+mp-TiO ₂ exhibiting one diode junction. • In contrast, the major potential drop was found on both sides of the perovskite layer in planar PSCs, indicating two diode junctions, which the generated ca	
KPFM	CPD maps on cross-sectional complete devices.	A nominal tip radius of ~25 nm; quantitative	Static	FTO/c-TiO ₂ /n-type perovskite/p-type perovskite/spiro-MeOTAD/Au	• A potential drop is observed at the interface of the n-type/p-type perovskite layers caused by the carrier separation at the interface. • It demonstrates the existence of a built-in electric field and hence the existence of a p-n junction.	[24f]
CL/SE	Halide segregation	All CL images were acquired with 512 × 512 pixels of a 10 μm × 10 μm field of view.	Dynamic (yes)	MAPb(I _x Br _{1-x}) ₃ polycrystalline films; solution-processed.	• Photoinduced halide segregation arises when charged excitations generate sufficient lattice strain to destabilize the solid solution.	[41]
Nanoprobe (nano)-XRF	Halide segregation	250 nm resolution; qualitative.	Dynamic (no)	MAPbBr ₃ single crystal.	• Nano-XRF mapping employed to identify the spatial distribution of elements within MAPbBr ₃ single crystal under applied bias. • A direct relationship between migration and local optoelectronic response by PL mapping is provided.	[192]

					<ul style="list-style-type: none"> • As Br⁻ migrates from the negatively biased electrode and the perovskite becomes locally sub-stoichiometric, the PL intensity decreases. 	
PL mapping	Influence of atmospheric gases (O ₂ , H ₂ O, N ₂)	Qualitative.	Dynamic (no)	MAPbI ₃ (~250 nm) on cover slip glass.	<ul style="list-style-type: none"> • The response of each grain to continuous illumination and atmospheric environment was studied. • PL mapping in N₂ shows the grain-to-grain heterogeneity with bright and dark grains. • PL mapping under N₂ + H₂O (~45% RH) reveals both the bright and dark grains to show a gradual rise in intensity. • PL mapping under dry air reveals that bright grain exhibits stable PL over time, while the dark grain, which likely has a higher defect density than the bright grain, shows significant PL enhancement under illumination and eventually reached the same intensity as the bright grain. • PL mapping under air + H₂O (~45% RH) shows an initial baseline increase (i.e., before any light illumination) in the emission intensity for both bright and dark grains. Then the emission from both bright 	[45b]

					and dark grains slowly rises over time under illumination with again a greater relative increase for the dark grain than the bright grain.	
--	--	--	--	--	--	--

2231 Abbreviations: UHV = ultrahigh vacuum; STM = scanning tunneling microscopy; STS = scanning tunneling spectroscopy; HRTEM = high resolution
2232 transmission electron microscopy; KPFM = Kelvin probe force microscopy; LCPD = local contact potential difference; XRF = X-ray fluorescence;
2233 PL = photoluminescence; SAM = self-assembled monolayer; CL = cathode luminescence; SE = secondary electrons; FTO = fluorine-doped tin oxide,
2234 C₆₀-C₆-PA = C60-functionalized 6-octyl phosphonic acid; PEDOT:PSS = poly(3,4-ethylenedioxythiophene) polystyrene sulfonate.

2235 **Table 2.** The type of defects, related characterizing method and its effect related to photovoltaic parameters.

Type of defects	Healing process	Perovskite	Method	Sample	Activation energy/ Or V_{TEF} (only to SCLC)	Defect density/cm ⁻³	Voc/V	Jsc/ma/cm ²	FF/%	PCE	Ref
Grain boundary											
	DMF vapor	MAPbI ₃	TAS	Control	0.30-0.40 eV	5.3×10^{18}	0.96	16.8	69.5	10.5	[154]
			Passivation			1.8×10^{18}	0.96	21.0	76.0	15.1	
	Hydroxylamine hydrochloride	MAPbI ₃	SCLC	Control	V_{TEF} 0.60 V	2.1×10^{16}	1.05	22.01	74.80	16.85	[159b]
			Passivation		V_{TEF} 0.34 V	1.2×10^{16}	1.10	22.42	76.07	18.69	
	ITIC	MAPbI ₃	SCLC	Control	V_{TEF} 0.90 V	3.2×10^{16}	1.06	21.07	74.7	16.66	[163]
			Passivation		V_{TEF} 0.17 V	5.9×10^{15}	1.07	22.02	75.5	18.03	
	E2CA	MAPbI ₃	SCLC	Control	V_{TEF} 0.68 V	1.06×10^{16}	1.07	21.92	77.9	18.23	[161]
			Passivation		V_{TEF} 0.49 V	0.77×10^{16}	1.09	22.06	80.5	19.51	
	PFA	MAPbI ₃	SCLC	Control	V_{TEF} 2.02 V	2.9×10^{16}	0.98	20.14	63.39	12.71	[162]
			Passivation		V_{TEF} 0.12 V	9.3×10^{15}	1.05	21.71	70.97	16.18	
Surface/Interface											
	PFA	MAPbI ₃	SCLC	Control	V_{TEF} 2.02 V	2.9×10^{16}	0.98	20.14	63.39	12.71	[162]
			Passivation		V_{TEF} 0.87 V	1.4×10^{15}	1.04	20.45	68.10	14.48	
	choline chloride	MAPbI ₃	TAS	Control	Deeper 0.35-0.40 eV	Higher	1.04	22.5	73	17.1	[18]
			Passivation		shallow 0.40-0.52 eV	Lower	1.15	22.9	76	20.0	
	PCBM	MAPbI ₃	TAS	Control	Deeper >0.40 eV	1×10^{19}	1.10	22.81	73.8	18.5	[133]

				Passivation	Shallow 0.35-0.40 eV	1×10^{17}	1.21	22.60	76.1	20.9	
	C ₆₀ -ETA	MAPbI ₃	SCLC	Control	-	4.14×10^{16}	1.09	22.35	75.56	18.03	[134]
				Passivation	-	1.99×10^{16}	1.09	22.75	78.56	19.12	
	π -conjugated Lewis base	MAPbI ₃	TAS	Control	0.33–0.45	1×10^{19}	1.03	19.37	-	13.5	[135]
				Passivation		1×10^{18}	1.11	22.96	-	19.5	
	CsBr	MAPbI _{3-x} Cl _x	TAS	Control	0.16-0.40 eV	5.0×10^{16}	0.99	18.7	69	13.1	[137]
				Passivation		2.0×10^{16}	1.06	20.7	75	16.3	
	PbI ₂	Cs _{0.02} MA _{0.03} FA _{0.95} Pb(I _{0.9} ₅ Br 0.05) ₃	TAS	Control	0.06-0.20 eV	Higher	1.04	23.8	75.2	18.8	[115]
				Passivation		Lower	1.15	24.8	78.4	22.3	
Bulk point defect											
I_Frenkel defect	K ⁺ (KI)	(FAPbI ₃) _{0.87} ₅ (CsPbBr ₃) _{0.125}	SCLC	Control	V _{TEF} 0.79 V	1.37×10^{16}	1.03	21.8	67	15	[126a]
				Passivation	V _{TEF} 0.62 V	0.85×10^{16}	1.14	21.7	72	18	
Deep-defect	MA	Cs _{0.2} FA _{0.8} Pb (I _{0.75} Br _{0.25}) ₃	TAS	Control	Deep	2.1×10^{16}	1.16	19.9	76	17.5	[193]
				Passivation	0.18 eV	Disappeared					
				Control	Shallow	0.6×10^{16}	1.21	21.0	79	20.0	
				Passivation	0.11 eV	1.1×10^{16}					
PbI ₃ ⁻ antisite defect	Ni ²⁺	MAPbI ₃	TAS	Control	Shallow	Higher	1.08	21.55	74	17.2	[126b]
				Passivation	0.05 eV	Lower	1.13	22.64	81	20.6	

Pb _i and antisite defects	I ₃ ⁻	MAFAPbI _{3-x} Br _x	DLTS	Control	Deep/Deep/Semi shallow 0.78/0.82/0.46 eV	Same/5.28 × 10 ¹⁴ /- Same/5.28 × 10 ¹⁴ /-	1.07	23.5	80.8	20.3	[96a]
				Passivation			Same/8.81×10 ¹³ / Disappeared	1.10	24.1	81.9	
	Rb5Cs5	FA _{0.83} MA _{0.17} Pb(I- _{0.83} Br _{0.17}) ₃	TSC	Control	-	7.3×10 ¹⁶	1.12	19.21	70	15.08	[126d]
				Passivation	-	1.6×10 ¹⁶	1.14	20.65	72	17.02	

2236 Abbreviations: DMF = Dimethylformamide; TFL = Trap-filled limit; SCLC = space charge limited current; TAS = thermal (thermal admittance
2237 spectroscopy; TSC = thermal stimulated current; DLTS = deep-level transient spectroscopy.



Yabing Qi is Professor and Unit Director of Energy Materials and Surface Sciences Unit at Okinawa Institute of Science and Technology Graduate University in Japan. He received his B.S., M.Phil., and Ph.D. from Nanjing Univ., Hong Kong Univ. of Sci. and Tech., and UC Berkeley, respectively. His research interests include perovskite solar cells, surface/interface sciences, lithium ion batteries, organic electronics, energy materials and devices (<https://groups.oist.jp/emssu>).

Table of Contents

Progress of Surface Science Studies on ABX_3 Based Metal Halide Perovskite Solar Cells

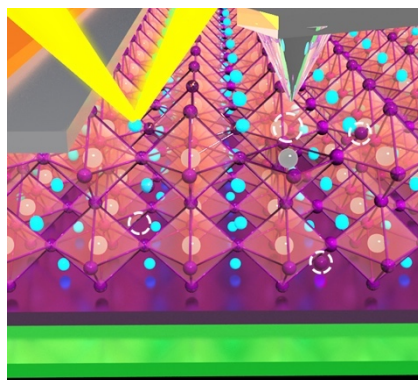
*Longbin Qiu†, Sisi He†, Luis K. Ono†, Yabing Qi**

Dr. L. Qiu, Dr. S. He, Dr. L. K. Ono, Prof. Y. B. Qi

Energy Materials and Surface Sciences Unit (EMSSU), Okinawa Institute of Science and Technology Graduate University (OIST), 1919-1 Tancha, Onna-son, Kunigami-gun, Okinawa 904-0495, Japan.

*Corresponding author: Yabing Qi, E-Mail: Yabing.Qi@OIST.jp

†These authors contributed equally to this work.



Recent case studies demonstrate how probing of local heterogeneities and ensembled average properties in larger scale of perovskites by surface science techniques can help build connections between material properties and perovskite solar cell performance. In this review article, we also focus on how generation and healing of electronic defects within the semiconductor band gap influence perovskite solar cell efficiency, lifetime, as well as reproducibility.